Template-Free Assembly of Three-Dimensional Mesostructures via Polarization Control

Thesis by

Natasha D. Reich

In Partial Fulfillment of the Requirements for the degree of

Doctor of Philosophy

CALIFORNIA INSTITUTE OF TECHNOLOGY

Pasadena, California

2026

(Defended May 1st, 2026)

Natasha Daphne Reich
ORCID: 0000-0002-8215-792X

ACKNOWLEDGEMENTS

I first want to thank my advisor, Nate Lewis. I knew when I first joined that the Lewis group was a special place, where group members considered themselves part of a larger team, never a sole individual, always supporting, advising and helping one another. A large part of that culture can be attributed to Nate's approach to running a group, particularly his emphasis on his graduate students as real people, not just machines that produce science. It was the kind of culture that made me fall in love with science again, after a challenging first year of graduate school. If not for my late admittance to Nate's group, I do not believe that I would be writing a PhD thesis at all. I am so grateful for the opportunities Nate provided me, in allowing me to explore a wide range of scientific interests and grow as an independent researcher. I also would know a lot less about ice cream, the Dodgers, wind-surfing, cold fusion, Southern California water parks, and minions, if not for him.

I also want to thank my committee, Harry Gray, Geoff Blake, and Mitchio Okumura, for their scientific feedback and advice throughout my PhD. I am especially grateful to Harry, for being my Chair and for his personal support over the years. It was also a pleasure to traverse up a flight of stairs to his office on occasion when I wanted to procrastinate work and hear a few of his fantastic stories. It was a particular pleasure to learn about his time teaching the first joint Barnard College and Columbia University chemistry course, which happened to be Advanced Inorganic Chemistry, one of my favorite courses during my time at Barnard.

Words really can't express my gratitude to Azhar Carim, who has been many things to me during my PhD: a scientific advisor, a career advisor, a mentor, a copyeditor, a committee member, a bad influence, and a friend. He made a tremendous effort to teach me

everything I know about electrochemistry, optics, and making squiggly shapes, and he always had faith that I could learn something, even when I didn't. His belief in me kept me going through many scientific and personal obstacles. His companionship in the lab and at the SEM ruined a few depositions and many images, respectively, but it also made long workdays and late hours feel a lot more fun. It's really been a pleasure; thank you for everything.

Whatever Azhar Carim did not teach me about making squiggly shapes, Madeline Meier filled in the gaps (and the reverse of that sentence would also be true). She is the reason I joined the Lewis group, and her friendship, mentorship, and support got me through a very tough first two years of graduate school. I'll see you for a HGW and handmade pasta in Chicago soon.

I want to thank all members of the Lewis group I have had the pleasure of being mentored by and working with over my five years: Jackie Dowling, Jake Evans, Sean Byrne, Zach Ifkovits, Mo Morla, Alex Ye, Sarah Kabboul, Dominic Covelli, Paul Bean, Elaine Shen, Imra Tajuddin, and in particular, the current squiggles subgroup, Giulia Luciani, Jackie Katsirubas, and Ariel Struzyk, who have made the last couple years very fun. There is really no one else I'd rather make fun of Azhar with. I also want to say that especially in my first couple years of graduate school, the support of senior students was particularly crucial to any success I could claim, and I'm so grateful for the time and effort that was given to me by very busy and talented graduate students.

I am extremely grateful to the Barnard Chemistry Department, which made a tremendous and successful effort to make chemistry a subject that people fell in love with and didn't fear. In particular, Rachel Austin's General Chemistry course was where this all

stated. I religiously attended every single office hour she hosted each week (there were eight) and I often brought questions completely unrelated to the material she was teaching to four hundred students. She gallantly put up with my irrelevant questioning and eventually she pulled me aside one day to suggest gently that I might consider majoring in chemistry, which should not have, but did, come as a completely surprising idea. Despite my clear interest in the subject, I didn't understand what someone would do with that degree, and Rachel took the time to explain what that major would mean, even welcoming me into her lab for a semester. Dina Merrer's Organic Chemistry sequence further solidified my passion for the subject, and my acceptance into Michael Campbell's lab was the final nail in the coffin. Mike's mentorship and teaching as I first took ownership over an independent research project was incredibly crucial to building my love for research and confidence in myself as a potential scientist. I am so grateful for his teaching and support, and to the other lab members during my time in his group: Tasneem Elkoush, Emily Miura-Stempel, and Dr. Fei Bu, as well Ana Beatriz Bonfim especially, who also became a close friend.

At risk of being grandiose, I want to thank every single teacher I have had, at Caltech and at Barnard, and especially the teachers of my elementary, middle, and high schools. Being a teacher is a tremendous and challenging responsibility, and I am so grateful to have had so many wonderful ones over the years.

As a long-time leader of PRISM, Caltech's LGBTQ+ organization, I want to thank every person who attended one of our events, as well as to all the other club leaders and advisors that I've worked with, particularly Devon Dobbs and Alex Winnett. Creating visible queer community at Caltech has often felt like a Sisyphean task, but it's also been very fun and I'm grateful to everyone I've been in those trenches with. I also want to thank all the

Crescent Valley High School students who I've mentored as part of the Sustainable Energy Activity Lab outreach program. Their enthusiasm and passion reignited my own excitement about science at many points throughout graduate school, and I'm also so grateful to Kitty Cahalan for her work in keeping that program up and running.

I especially want to thank our union, UAW 2478, and every single person I worked with as we dropped cards, whipped votes, and ratified our first contract. Being part of this campaign was extremely special to me, and it was made even more special by getting to learn from and work with such a smart, passionate, and talented group of people. I also want to thank all the graduate students and postdocs at Caltech who welcomed us into their office and lab spaces and shared their time and concerns as we all navigated this complicated process together. Having a union is better than not having one at all but having a really good union requires a lot of work, and I'm so thankful for everyone who puts in the work to make ours possible.

Now that the professional business is out of the way, I want to thank many amazing people who I am so honored to call a friend: Frieda Mueller, Thomas Boers, Claire Walker, Divara Cendana, Marina Lecoeuche, Jakob Faber, Dee Dunne, Rahma Elsiesy, Richard Horak, Kiran Grewal, and Shehab Fadda. I'm incredibly grateful to have you all in my life. I also want to thank Liz Irvin who provided me with so much support and love over the years and during my PhD. I am very grateful to her. I want to thank Rosie Lichtenbaum whose visits to LA during my PhD provided a critical anchor and who truly makes me laugh like no one else. I want to thank Aditi Rao for loving me when I was eighteen, at my most annoying and ridiculous, and now and into the future. I feel so lucky to have you, and your lovely wife and family, in my life. I especially want to thank Nadia Suryawinata, who has

been a major bastion and fierce cheerleader during my PhD and has brought so much fun, love, and cool clothes into my life. I want to thank Sam Ponnada for his friendship and love—his scientific prowess and innate ability to make friends and bring people together consistently amaze me. I want to thank Jasmine Emtage, who, especially in the last two years, really kept me afloat. Her kindness, generosity, and intelligence are truly unparalleled, and her love and friendship mean so much to me. Thank you for taking care of me and letting me take care of you.

I want to thank Kelcey Wallens-Logan. If you will have us, me and this thesis are yours. You became my family, when I was so far away from my own. Our time together at 1108 E Palm St was one of the happiest in my life—knitting and cooking and spinning and weaving and dyeing and dancing and sewing and watching TV and lying on our couch and lying in our beds and pretending we were going to garden and barbecuing and walking to the base of the mountains and sitting on our front porch. The fire took so much from us, but I'm so glad it couldn't take you. I'm so proud of you—in your last four years, as a truly talented and beloved educator, and in your future, as a truly talented and beloved social worker. I'm also so grateful to the members of your family who welcomed me in and made LA feel more like home: Blake, Nicole, Donald and Sharon.

I want to thank my own family, and in particular, Ange, Stephen, Nat, Jessica, Stephanie, Juliette, Jo, Jacqui, Leon, Gordon, Morris, Alex, and Beth, who have been so supportive and excited for me throughout my PhD. I also want to mention my grandparents, Judith, Daphne, Michaelis, and Bill, and my great aunt, Natalie, who are no longer with us, but whom I think about often and wish I could have shared this accomplishment with.

I am so grateful to my little brother, Julian, whose intelligence, determination, and bravery constantly inspire me. He has made such an effort to keep us in touch while living on opposite coasts, and I'm so happy to be moving closer to you in this next phase. I feel so lucky to have you as my sibling.

I of course want to thank my parents, Nick and Elizabeth. Without a doubt, I could not have done this without you. You have been there for me every step of the way, supporting and helping and counseling, not just in my PhD, but at every stage of my life. I cannot express how grateful I am to you for everything you've given me and how lucky I feel to share this accomplishment with you.

Finally—since I began this PhD, every physical university campus in Gaza has been heavily damaged or destroyed. As someone who once stood in the rubble of my own home and belongings, I can't even begin to imagine the pain and grief of the Palestinian people, not only since 2023, but since 1948. As an American Jew, it shames me deeply for this genocide and destruction to be perpetuated in my name. It is not only a fundamental human right to live on your land, to not be jailed or killed, to have food and water, but it is also a fundamental human right and drive to study and create knowledge. I feel unbelievably lucky to have had the opportunity to do that in my PhD, and I feel unbelievable anger that the same opportunity has been taken from so many. From the river to the sea.

ABSTRACT

Plants are inherently sessile and thus exhibit adaptive morphologies to forage for essential resources such as light. For example, palm trees grow with a pronounced tilt towards the time-averaged solar position to optimize light collection. In analogy, electrochemical growth of semiconductor material under illumination can result in spontaneous self-organization. Such inorganic phototropic growth can produce mesostructured deposits consisting of ordered nanoscale features over cm^2 areas, despite a lack of lithographic processing, structured light fields, or templating agents (ligands, surfactants, etc.). Precise deposit morphologies are determined by the characteristics of the input illumination. Growth using linearly polarized illumination produces highly anisotropic lamellar arrays with a feature pitch proportional to the wavelength. Abrupt, orthogonal shifts in the polarization direction during growth reorient the direction of the in-plane anisotropy producing woodpile architectures with independently tunable layer heights. Moreover, spatial registration between alternating layers is produced via optical coupling across the intermediary layer. The investigations described herein demonstrate that inorganic phototropic growth enables programmable, high-throughput fabrication of complex three-dimensional lattices that cannot be achieved easily, if at all, via conventional means.

PUBLISHED CONTENT AND CONTRIBUTIONS

Portions of this thesis have been drawn from the following publications:

Mechanism of Mesoscale Woodpile Development via Photoelectrochemical Deposition of Se–Te
Reich, N. D.; Lewis, N. S.; Carim, A. I. *ACS Nano*, **2025**, *19*, 34869-34879. DOI: 10.1021/acsnano.5c10748
N.D.R. performed the experiments and modeling, analyzed the data, and helped prepare the manuscript.

Photonic Templating of Inorganic Phototropic Growth Produces Extended Vertical Registration in Multilayered Mesostructures
Reich, N. D.; Lewis, N. S.; Carim, A. I. *In Preparation.*
N.D.R. performed the experiments and modeling, analyzed the data, and helped prepare the manuscript.

Cost-Effective Approaches to Maintaining Resource Adequacy in Wind and Solar Electricity Systems Over Decades of Weather Variability
Reich, N. D.; Ruggles, T. H.; Virgüez, E.; Dowling, J. A.; Caldeira, K.; Lewis, N. S. *Submitted.*
N.D.R. performed the modeling, analyzed the data, and wrote the manuscript.

TABLE OF CONTENTS

LIST OF FIGURES

Chapter 1

INTRODUCTION AND BACKGROUND

1.1. Background

Materials structured at the nanoscale often demonstrate altered or enhanced properties compared to the same material in an unstructured form, which has led to widespread application in a variety of fields, including medicine, electronics, optics, photonics, and sensors. Many of the applications of nanostructured surfaces currently being explored take inspiration from advantageous properties found in the nanostructured surfaces of plants and animals. For example, the feet of geckos have remarkable adhesion properties, enabling rapid climbing of smooth vertical walls and even ceilings, due in part to thousands of nano-meter scale spatulas on the bottom of their paws.[1-3] Reusable dry adhesives that mimic the gecko foot structure and leave no residue are currently being sold for use in robotics, construction, and semiconductor and automated manufacturing.[4] Sharks also have nanostructured pillars on their skin, called denticles, which afford them excellent drag reduction in water by reducing vortex ejection and outer-layer turbulence.[5,6] Shark skin, like the wings of certain species of cicada and dragonfly, also demonstrate excellent anti-biofouling properties as the nanostructured surface hinders bacterial colonization and biofilm formation, and has inspired the fabrication of similar structures for use in indwelling medical and dental devices.[7-10] Other nanostructured surfaces found in nature, particularly those on the blue wings of the *Morpho* butterfly, cause

interference of light that leads to highly stable, brilliant structural coloration, and both *Morpho* butterfly scales themselves and biomimetic analogs have been used for photonic gas and thermal sensing applications.[11,12]

To take advantage of the many desirable properties accessible through nanostructured surfaces, the discovery and optimization of nanofabrication techniques have been extensively studied. Electron beam lithography (EBL) is one of the primary nanofabrication methods in use, utilizing a focused beam of electrons to "draw" a desired pattern in an electron-sensitive film, or resist, on top of a substrate.[13] The electron beam changes the solubility of the resist, enabling selective removal of either the exposed or un-exposed regions through solvent immersion, and the pattern can then be transferred into or onto the substrate through material etching or deposition, respectively. Focused ion beam (FIB) lithography is a similar technique for fabrication of nanostructures, utilizing a focused beam of ions instead of an electron beam. FIB lithography can create a pattern in a resist layer like EBL, but it can also be used directly to mill away atoms or locally deposit material with < 10 nm resolution.[14] EBL and FIB lithography represent significant advances in the field of nanofabrication, but are also both fundamentally serial writing techniques, limiting throughput and scalability for large-area fabrication. In contrast, nanoimprint lithography is a widely used parallel patterning technique in which a nanostructured mold is pressed into a deformable resist layer to replicate features over large areas in a single step, followed by curing and mold release.[15,16] This approach enables high-throughput and relatively low-cost nanofabrication compared to techniques like EBL, but accessible structures are limited to those defined by replication from a master

mold, making the fabrication of complex, multilayered architectures a particular challenge. One recently discovered nanofabrication technique, termed inorganic phototropic growth, takes advantage of the light-matter interactions fundamental to the photo-electrodeposition of semiconducting materials to generate complex, multi-layered three-dimensional nanostructures in parallel.

1.2 Inorganic Phototropic Growth

The photo-responsive behavior of plants is a direct inspiration for inorganic phototropic growth. To enhance for light collection, biological systems capable of photosynthesis often display phototropism in which directed organ growth is dictated by the illumination available in the environment.[17] For example, palm trees in the northern hemisphere grow directionally towards the southern sky, the location of the time-averaged solar azimuth (Figure 1.1a). Light placement can be used to artificially manipulate the growth of plants that exhibit phototropism (Figure 1.1b). Direct overhead illumination causes cells in the plant stem to lengthen equally, resulting in upward growth. However, inclined illumination leads to uneven lengthening on either side of the stem and consequently results in tilting of the stem toward the light source. [17-20]

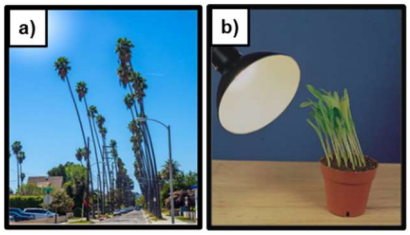

Figure 1.1. (a) Palm tree growth in Pasadena, California directed toward the time-averaged solar azimuth. (b) Direction of grass shoot growth can be artificially manipulated via placement of light source.

Analogous to biological systems, phototropic behavior has been demonstrated in chalcogen-based semiconductors, where the deposition of the material proceeds towards an uncorrelated light beam via a process termed inorganic phototropic growth.[21] Benchtop growth in the dark results in deposits with no long-range morphological order (Figure 1.2b). However, template-free growth on

isotropic substrates using low intensity illumination from an incoherent light-emitting diode (LED) source can generate highly anisotropic morphologies with nanoscale features over macroscale areas.[22] For example, growth using low intensity illumination from an incoherent light-emitting diode source generates an ordered array of nanopores (Figure 1.2c).[23]

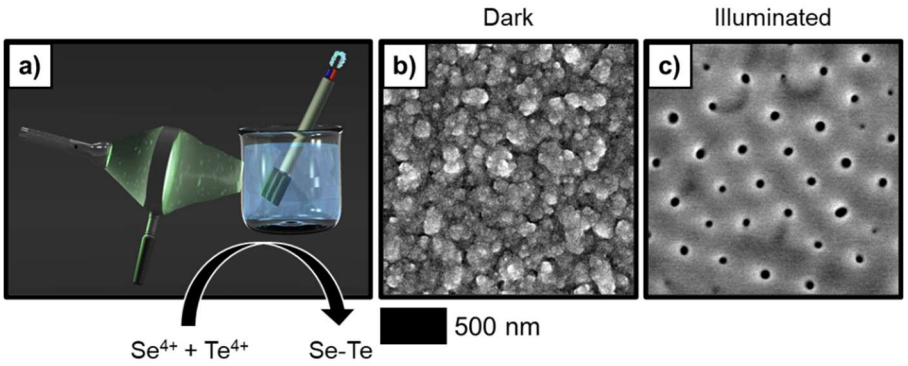

Figure 1.2. (a) Schematic of inorganic phototropic growth via cathodic electrochemical deposition of Se-Te. Representative SEM of films deposited (b) in the dark and (c) using unpolarized λ_{avg} = 630 nm.

Unlike lithographic processes that utilize structured light fields to generate defined morphologies, inorganic phototropic growth capitalizes on inherent anisotropies in the light-material interactions during material deposition under uniform illumination to generate order and anisotropy. The morphology of deposits generated via inorganic phototropic growth is determined by the characteristics of the input illumination, including the spectral distribution, polarization, phase, coherence, and incident direction.[21-24] Growth using linearly polarized illumination produces highly anisotropic, ordered lamellar structures. The long axes of the lamellar structures orient parallel to the electric field (E-field) vector of the input illumination (Figure 1.3a-c). Additionally, the pitch, or spacing, of the lamellar

features is defined by the wavelength of light used during the deposition process. Shorter wavelengths of light generate features that are more closely spaced (Figure 1.3d). Performing the same deposition but using light of longer wavelengths produces lamellae with a larger pitch (Figure 1.3e-f).

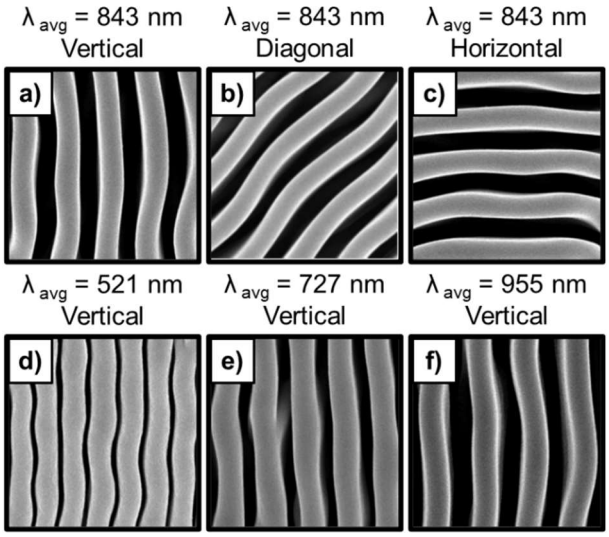

Figure 1.3. Top-down SEMs of deposits generated via inorganic phototropic growth using λ_{avg} = 843 nm with the polarization (a) vertical, (b) diagonal, and (c) horizontal and using vertically polarized light with λ_{avg} = (d) 521 nm, (e) 727 nm, and (f) 955 nm.

The development of the structural anisotropy observed in the top-down SEMs can be further examined in cross-sectional SEMs by systematically varying the charge density of the deposition (Figure 1.4). At low charge densities, the top-down and cross-sectional SEMs reveal that the structure generated is mostly isotropic across the surface (Figure 1.4a-c). Increasing the charge density generates a structure with more defined lamellar features (Figure 1.4d-f) and increased structural anisotropy. After the initial definition of the features, a steady-state regime is observed, where additional charge density results in linear feature extension (Figure 1.4g-o).

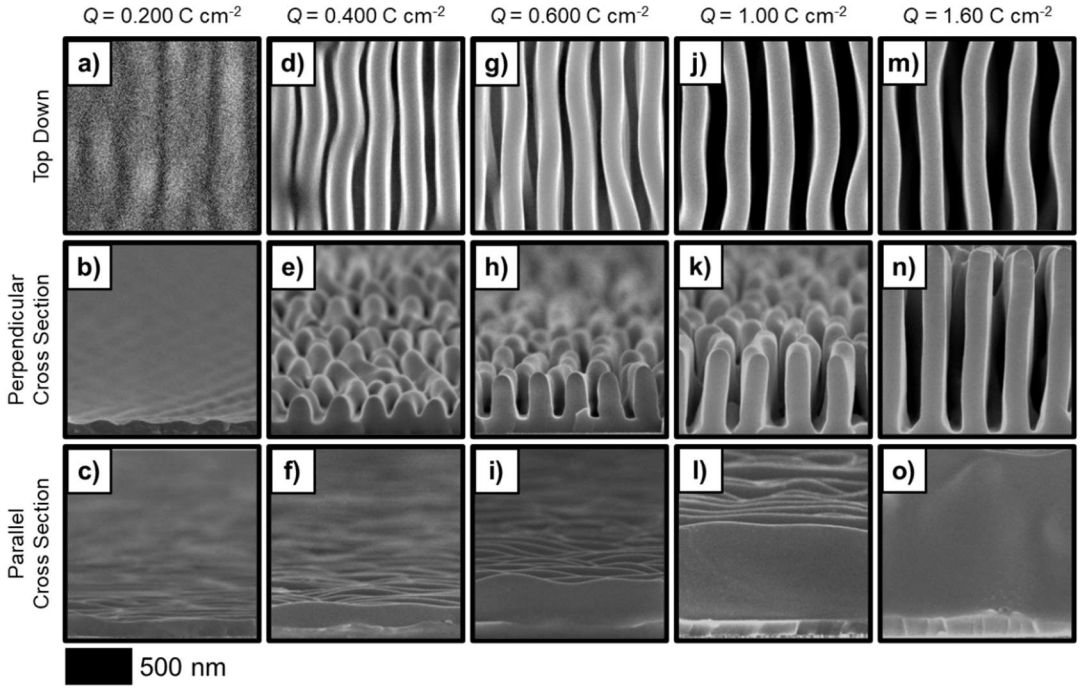

Figure 1.4. Top-down, perpendicular cross-sectional, and parallel cross-sectional SEMs of deposits generated via inorganic phototropic growth using the indicated charge densities.

Structure generation via inorganic phototropic growth is understood to be a result of emergent nanophotonic phenomena at the electrochemical interface. Initial electrochemical growth results in the generation of surface roughness which scatters the incident illumination. Figure 1.5a presents an optical simulation in which two dipole emission sources are utilized to represent scattering by initially deposited material. Periodic bands of electric field intensity are observed between the two emitters indicating that a spatially oscillating light intensity profile is generated at the interface. The rate of photoelectrochemical growth is accelerated in such regions, and a positive feedback loop results in which the additional mass at the high intensity regions results in higher absorption, thus maintaining the elevated rate of photoelectrochemical growth. To further understand the mechanism of inorganic

phototropic growth, an optically based model has been used to simulate the deposition process. The spatial profile of light absorption is first calculated via electromagnetic simulations and then utilized to weigh the local probability of mass addition in a subsequent Monte Carlo step. The new light absorption profile is then calculated and the process is iterated. Empirical inputs to the model are limited to estimates of the refractive index of the growth solution and complex index of the deposited material. Figure 1.5b-e presents successive model iterations of growth using linearly polarized λ_{avg} = 630 nm illumination with the overlaid spatial absorption profiles. Early, the absorption profile is somewhat conformal. Later, periodic absorbance bands are observed in the tips of nascent lamellar features, and such absorption directs continued anisotropic growth. The final structure is in good agreement with that observed experimentally (Figure 1.5f), indicating that morphology determination during inorganic phototropic growth is principally governed by optical interactions rather than chemical, crystallographic and/or transport biases.

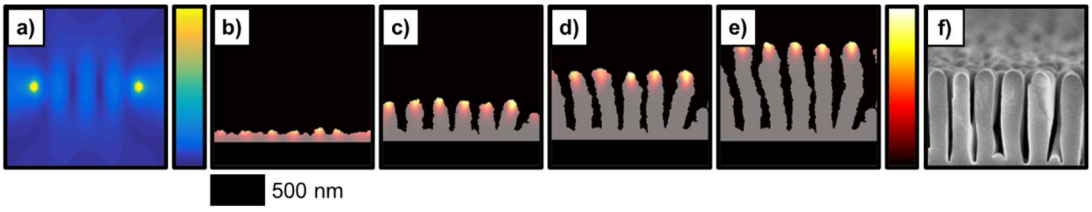

Figure 1.5. (a) Normalized time-average of electric field magnitude resulting from two dipoles emitting radiation with a free space wavelength of λ_{avg} = 630 nm separated by a distance of two wavelengths in the direction perpendicular to the oscillation axis. (b)-(e) Simulated profiles of absorption of illumination in deposit morphologies generated by growth modeling. Panels from left to right present profiles for successive iterations of the simulated morphologies. (f) Cross-sectional SEM of deposit generated under illumination of λ_{avg} = 630 nm.

Use of time-varying optical inputs to the inorganic phototropic growth process has recently been demonstrated as a method to direct generation of structures with increased three-dimensional complexity. For example, an abrupt shift in the input wavelength can effect evolution of the interfacial feature pitch and direct the growth of a structure resembling a tuning fork.[25] Figure 1.6 presents representative top-down and cross-sectional SEMs of deposits initially generated using a single wavelength input, λ_0 = 955 nm, and extended in a subsequent deposition step of variable length with a single input of a different wavelength, λ_1 = 528 nm. Continued growth with λ_1 resulted in an interfacial morphology matching that observed for deposits generated using λ_1 alone. This structural evolution is produced by the change in the interfacial absorption profile induced by the switch in the illumination input in order to optimize for light collection.

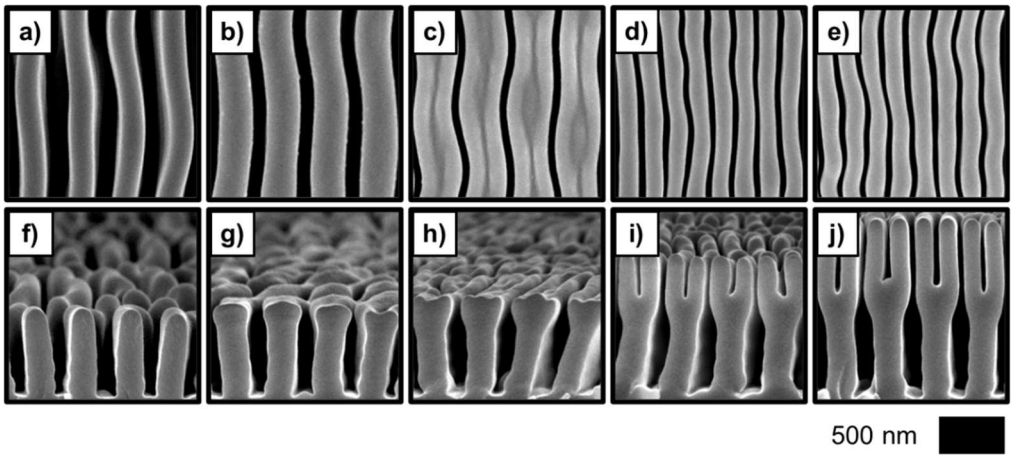

Figure 1.6. (a)-(e) Representative top-view and (f)-(j) cross-sectional SEMs of deposits generated initially using λ_0 = 955 nm for t_0 = 2.00 min and then extended in a subsequent deposition step using λ_1 = 528 nm for the indicated t_1.

1.3 Scope of Thesis

The focus of this thesis is the use of dynamic changes in the polarization of light during film deposition via inorganic phototropic growth. Chapter 2 presents an investigation of the impact of abrupt, orthogonal shifts in the polarization of light during photoelectrodeposition of Se-Te and the underlying nanophotonic interactions by which complex, three-dimensional layered structures can be generated. Chapter 3 explores a photonic templating phenomenon wherein inorganic phototropic growth proceeds at an isotropic interface to produce spatial registry in a multi-layer structure despite stimulation with spatially uniform illumination. Chapter 4 details the experimental methods for the work presented in Chapters 2 and 3.

Chapter 2

MECHANISM OF MESOSCALE WOODPILE DEVELOPMENT VIA PHOTOELECTROCHEMICAL DEPOSITION OF SE-TE

Reich, N. D.; Lewis, N. S.; Carim, A. I. *ACS Nano*, 2025, *19*, 34869-34879. DOI: 10.1021/acsnano.5c10748

2.1. Introduction

Mesoscale woodpile morphologies have been studied extensively as a prototypical photonic crystal structure that has a photonic band gap at near-infrared and visible frequencies, with applications including integrated photonic circuits, light manipulation, and responsive optical materials.[26-32] Woodpile nanostructures also are potentially useful as three-dimensional electrode supports for lithium-ion battery anodes, as supports for electrocatalysis of the oxygen-evolution and oxygen-reduction reactions (OER and ORR), and as electrochemical biosensors.[33-36] Additionally, such structures exhibit a uniform spatial distribution of high optical enhancement sites for surface-enhanced Raman spectroscopy (SERS) analysis.[37,38]

This work focused on the synthesis and development of woodpile structures in response to an orthogonal change in the polarization direction during photoelectrochemical deposition.[39] During the formation of a woodpile structure, deposition of mass could occur primarily at the tips of the lamellae and/or across the sidewalls of the underlying material. The analysis presented herein elucidates the light-matter interactions that lead to directional deposition of material from

preexisting lamellae, as well as self-organization of suspended bridging deposits, and fusion of individual suspended features into overlying lamellae to form a woodpile. Electron microscopy revealed the morphologies of the deposits as a function of the deposition charge density both before and after the polarization change. Deposition was performed using two distinct continuous illumination wavelengths as well as using a change in wavelength concomitant with a shift in the direction of optical polarization. Computational modeling of the deposition, in conjunction with electromagnetic simulations of simplified structures that were representative of the experimentally observed morphologies, elucidated the stepwise physical phenomena that underpin the formation of these mesoscale woodpile structures.

2.2. Results and Discussion

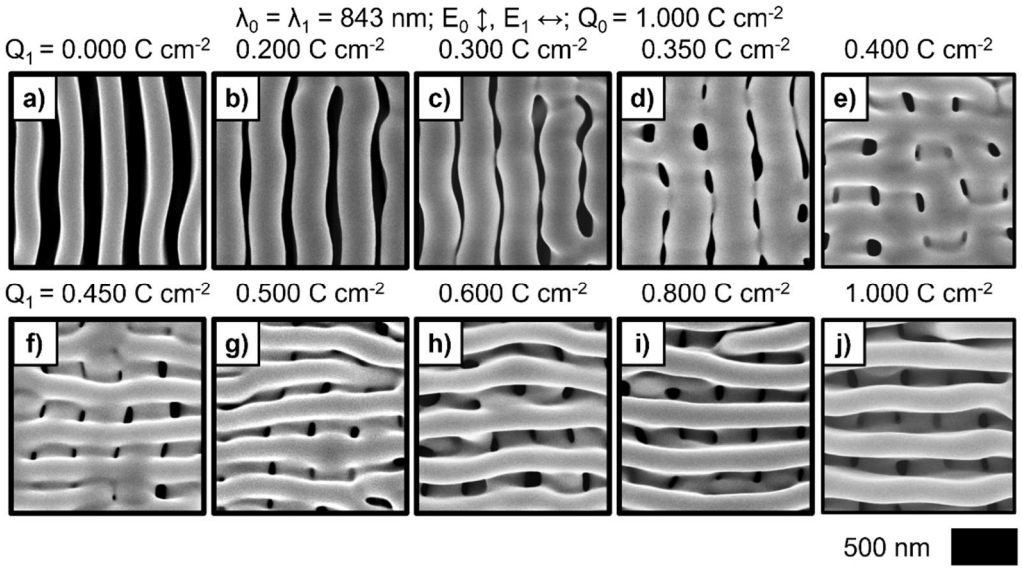

Figure 2.1. Representative top-down SEMs of deposits generated with λ = 843 nm initially using vertical polarization (E_0 ↕) for Q_0 = 1.000 C cm^{-2} followed by horizontal polarization (E_1 ↔) for the indicated Q_1.

Light-directed electrochemistry produced deposits of Se-Te from an aqueous solution of fully oxidized precursors. Herein, a narrowband light-emitting diode (LED) provided spatially uniform, linearly polarized illumination for deposition. Figure 2.1a presents a representative top-down scanning-electron micrograph (SEM) of a deposit generated with an initial intensity-weighted average illumination wavelength, λ_0, of 843 nm and an initial deposition charge, Q_0, of 1.000 C cm^{-2}. The light was polarized such that the oscillation of the E-field was along the vertical, resulting in ordered lamellae with a long axis aligned along the vertical. The pitch and width of the lamellae were 318 ± 10 nm and 215 ± 6 nm, respectively. Figure 2.1b-j presents representative SEMs of deposits initially generated in the same manner as the deposit depicted in Figure 2.1a. However, the deposition was then continued with a charge density, Q_1, utilizing horizontally

polarized illumination with the same wavelength used initially ($\lambda_0 = \lambda_1 = 843$ nm). At $Q_1 = 0.200$ C cm^{-2} (Figure 2.1b), the width of the lamellae was larger than for the structure that was generated using only vertically polarized light (Figure 2.1a). At $Q_1 = 0.300$ C cm^{-2} (Figure 2.1c), the width of the lamellae increased further, but in a nonuniform and periodic fashion along the vertical. At $Q_1 = 0.350$ C cm^{-2} (Figure 2.1d), spatially non-uniform bridging features formed across the void space between the vertically aligned features. At $Q_1 = 0.400$ C cm^{-2} (Figure 2.1e), more well-defined, uniform bridging was observed relative to $Q_1 = 0.350$ C cm^{-2} (Figure 2.1d), with the bridging features exhibiting spatial periodicity in the vertical direction. A charge density of $Q_1 = 0.450$ C cm^{-2} led to a woodpile structure that consisted of a horizontally aligned array of lamellae on top of a vertically aligned array of lamellae (Figure 2.1f). Deposition with $Q_1 = 0.500$, 0.600, 0.800 and 1.000 C cm^{-2} (Figure 2.1g-j) also produced woodpile structures, with increasing definition and topographic prominence of the horizontal structure as Q_1 increased. The morphology of the topmost layer for $Q_1 = 1.000$ C cm^{-2} (Figure 2.1j) was similar to the structure that was generated using only vertically polarized light (Figure 2.1a), albeit with horizontally rather than vertically aligned lamellae. The pitch and width of these horizontal features were 324 ± 6 nm and 223 ± 8 nm, respectively. Energy-dispersive X-ray spectroscopic analysis (EDX) indicated a relatively consistent stoichiometry of the deposited Se-Te material as Q_1 increased.

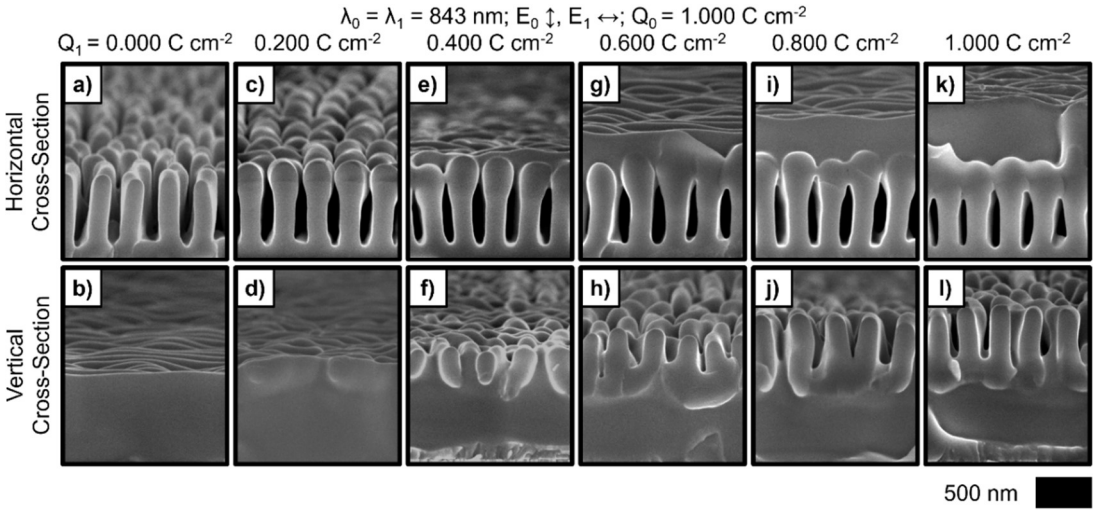

Figure 2.2. Representative horizontal and vertical cross-sectional SEMs of deposits generated with λ = 843 nm initially using vertical polarization (E_0 ↕) for Q_0 = 1.000 C cm^{-2} followed by horizontal polarization (E_1 ↔) for the indicated Q_1.

Figure 2.2 presents representative cross-sectional SEM data analogous to the top-down data presented in Figure 2.1. Horizontal cross-section data were obtained by physically cleaving the substrates and top-facing deposits along the horizontal. To determine the out-of-plane morphology, these cleaved deposits were then analyzed at a near-grazing viewing angle. Analogous vertical cross-section data were obtained with the substrate and top-facing deposits cleaved along the vertical. The horizontal cross-section of the structure that was generated using only vertically polarized light (Q_1 = 0.000 C cm^{-2}, Figure 2,2a) showed lamellae with substantial out-of-plane anisotropy that moreover projected vertically along the substrate normal. The corresponding vertical cross-section (Figure 2.2b) revealed a uniform sidewall consistent with the directional deposition observed in the top-down SEMs (Figure 2.1a). Subsequent deposition using horizontally polarized light (Q_1 = 0.200 C cm^{-2}) produced lateral broadening of the feature tips in the horizontal cross-section (Figure 2.2c) and three-dimensional texture at the top of the sidewall

in the vertical cross-section (Figure 2.2d). At Q_1 = 0.400 C cm^{-2}, a ridge in the horizontal cross-section (Figure 2.2e) extended across the frame at a height close to the height of the broadened lamellar tips. The void space between the sidewalls was similar in size to the void space observed for Q_1 = 0.200 C cm^{-2} (Figure 2.2c). The vertical cross-section at Q_1 = 0.400 C cm^{-2} (Figure 2.2f) revealed formation of nascent, periodic features along the top of the observed sidewall. At Q_1 = 0.600 C cm^{-2}, the top of the ridge feature in the horizontal cross-section extended above the tips of the lamellae (Figure 2.2g). Moreover, the features observed in the vertical cross-section at Q_1 = 0.400 C cm^{-2} (Figure 2.2f) increased in height and became more well-defined at Q_1 = 0.600 C cm^{-2} (Figure 2.2h). At Q_1 = 0.800 or 1.000 C cm^{-2}, the ridge features continued to increase in height in the horizontal cross-section (Figures 2i and k, respectively), whereas in the vertical-section (Figures 2j and l, respectively) the ordered lamellae further increased in height, consistent with the formation of the woodpile structure observed in the analogous top-down SEMs (Figures 1i and j).

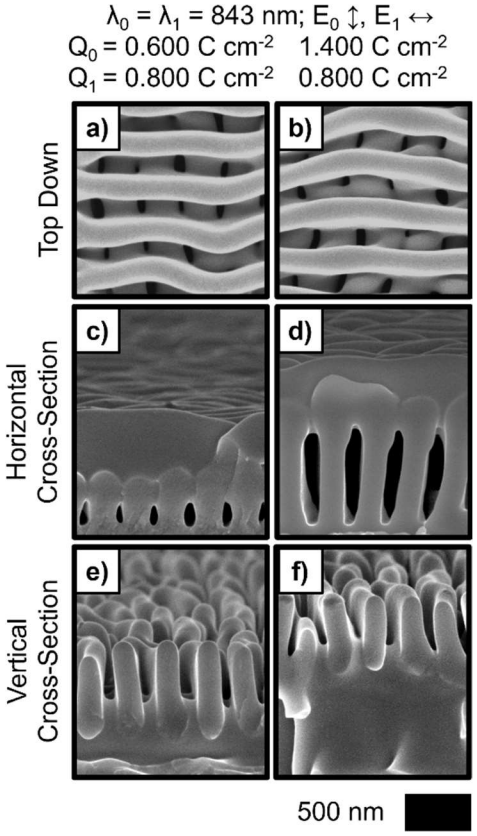

Figure 2.3. (a) and (b) Representative top-down and corresponding (c) and (d) horizontal and (e) and (f) vertical cross-sectional SEMs of deposits generated with λ = 843 nm initially using vertical polarization (E_0 ↕) for the indicated Q_0 followed by horizontal polarization (E_1 ↔) for the indicated Q_1.

To evaluate the formation of woodpiles derived from lamellae that had a series of different aspect ratios, additional depositions using constant wavelength illumination ($\lambda_0 = \lambda_1 = 843$ nm) were performed with Q_0 values of 0.600 or 1.400 C cm^{-2}. The initial deposition was performed using vertically polarized light. Q_1 was fixed at 0.800 C cm^{-2} for the subsequent deposition with horizontally polarized light. Top-down SEMs of deposits generated using Q_0 = 0.600 and 1.400 C cm^{-2} (Figure 2.3a and b, respectively) revealed mutually similar woodpile structures, characterized by horizontal lamellae atop vertical lamellae. For Q_0 = 0.600 C cm^{-2}, horizontal cross-sections revealed a uniform ridge feature above relatively shorter

transverse array of lamellae (Figure 2.3c). For Q_0 = 1.400 C cm^{-2}, the horizontal cross-section also displayed a uniform ridge above the transverse lamellae (Figure 2.3d). The lamellae were similar in height to the total structure height produced using Q_0 = 0.600 C cm^{-2} (Figure 2.3c) and taller than the ridge. Vertical cross-sections of deposits generated using Q_0 = 0.600 or 1.400 C cm^{-2} (Figure 2.3e and 3f, respectively) showed transverse lamellae projecting from the top of a uniform ridge. The heights of the ridges in the vertical cross-sections (Figure 2.3e and f) were in accord with the heights of the lamellae in the horizontal cross-sections (Figure 2.3c and d).

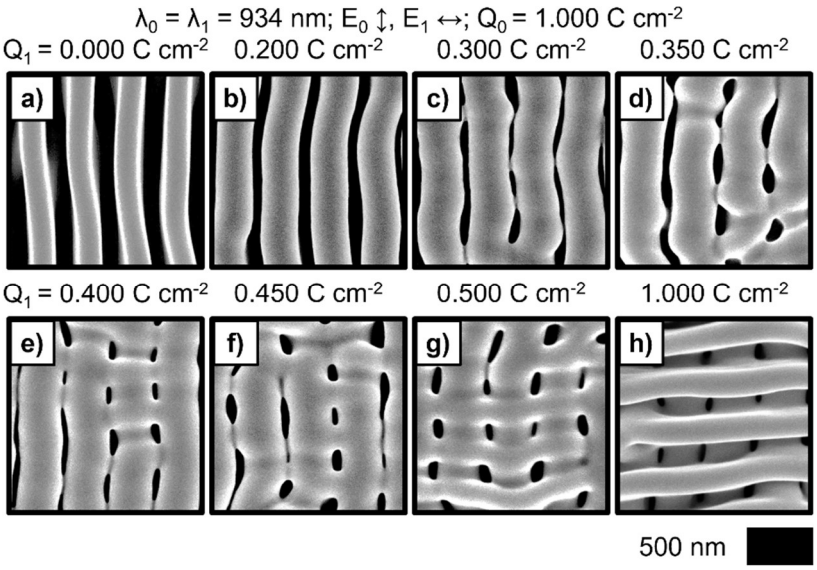

Figure 2.4. Representative top-down SEMs of deposits generated with λ = 934 nm initially using vertical polarization (E_0 ↕) for Q_0 = 1.000 C cm^{-2} followed by horizontal polarization (E_1 ↔) for the indicated Q_1.

Figure 2.4 presents representative top-down SEM data of deposits that were produced using $\lambda_0 = \lambda_1$ = 934 nm. Deposition with vertically polarized λ_0 = 934 nm light (Q_0 = 1.000 C cm^{-2}) resulted in vertically aligned lamellae (Figure 2.4a) similar to, but with a larger feature pitch and width (348 ± 7 nm and 250 ± 7 nm,

respectively) than, the lamellae that were produced using $\lambda_0 = 843$ nm (Figure 2.1a). Subsequent deposition with horizontal polarization for various Q_1 values (Figure 2.4b-k) resulted in development of a structure that closely resembled the structure obtained using $\lambda_0 = \lambda_1 = 843$ nm (Figure 2.1b-j). The lamellae increased in width, first uniformly ($Q_1 = 0.200$ C cm^{-2}, Figure 2.4b) and then in nonuniform periodic fashion ($Q_1 = 0.300$ C cm^{-2}, Figure 2.4c), leading to the formation of bridges across the void space between adjacent lamellae ($Q_1 = 0.350$ C cm^{-2}, Figure 2.4d). With further deposition, features continued to bridge underlying lamellae ($Q_1 = 0.400$ C cm^{-2}, Figure 2.4e) and exhibit more order ($Q_1 = 0.450$ C cm^{-2}, Figure 2.4f). Eventually a nascent woodpile structure formed ($Q_1 = 0.500$ C cm^{-2}, Figure 2.4g). For the fully developed woodpile structure ($Q_1 = 1.000$ C cm^{-2}, Figure 2.4h), the horizontally oriented lamellae had a pitch and width (350 ± 7 nm and 260 ± 8 nm, respectively) that were similar to the pitch and width of the vertically oriented lamellae that had formed before the polarization shift (Figure 2.4a).

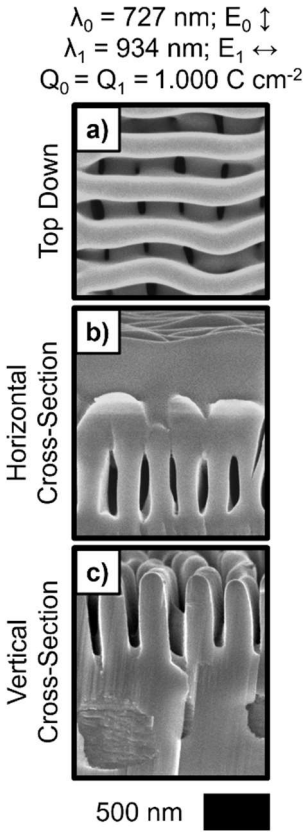

Figure 2.5. Representative (a) top-down and corresponding (b) horizontal and (c) vertical cross-sectional SEMs of a deposit generated initially with λ_0 = 727 nm and vertical polarization (E_0 ↕) for Q_0 = 1.000 C cm^{-2} followed by λ_1 = 934 nm and horizontal polarization (E_1 ↔) for Q_1 = 1.000 C cm^{-2}.

Deposition was also performed using a change in illumination wavelength ($\lambda_0 \neq \lambda_1$) concomitant with a shift in the polarization. The formation of woodpile structures having substantially different feature pitches in each layer was evaluated using λ_0 = 727 nm and λ_1 = 934 nm illumination. Figure 2.5 presents representative top-down and cross-sectional SEMs of a deposit generated using vertically polarized illumination with λ_0 = 727 nm for Q_0 = 1.000 C cm^{-2}, followed by horizontally polarized illumination with λ_1 = 934 nm for Q_1 = 1.000 C cm^{-2}. The top-down SEM (Figure 2.5a) revealed a woodpile structure similar to those generated using illumination with $\lambda_0 = \lambda_1$ = 843 nm (Figure 2.1j, Figure 2.4f). The

horizontal cross-section revealed a transverse lamellar array with a uniform ridge feature in the top layer (Figure 2.5b). The 263 ± 6 nm pitch of the underlying lamellar array was smaller than the pitch of the deposit that was generated using λ_0 = 843 nm (Figure 2k, 318 ± 10 nm). The vertical cross-section revealed transverse lamellae projecting from the top of a uniform ridge (Figure 2.5c). Moreover, the 343 ± 6 nm pitch of the top-layer lamellae formed using λ_1 = 934 nm illumination was larger than the pitch of lamellae formed using illumination with λ_1 = 843 nm (Figure 2l, 324 ± 6 nm).

An optically based, two-step computer model provided insight into the mechanism of mesoscale woodpile formation by the light-stimulated electrochemical deposition process. First, the spatial profile of light absorption at the electrochemical interface was calculated using an electromagnetic simulation. A Monte Carlo method was then used to simulate addition of material with a spatial probability that was proportional to the magnitude of the local light absorption. These steps were then successively iterated. Empirical inputs to the modeling were limited to estimates of the refractive index of the deposition solution and the complex index of the deposited material.

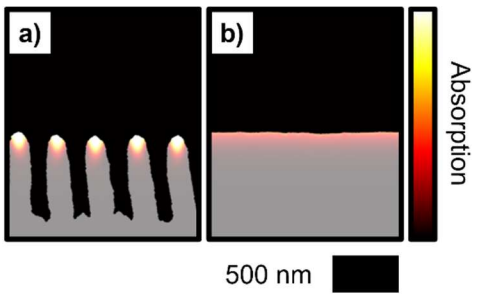

Figure 2.6. Simulated absorption profiles of deposit morphologies generated by two-dimensional modeling using λ = 843 nm with (a) TE polarization (E_0 ⊗) and (b) TM polarization (E_0 ↔).

Figure 2.6 presents the light absorption profiles of morphologies generated by two-dimensional deposition simulations using illumination with λ_0 = 843 nm. Light with transverse electric (TE) or transverse magnetic (TM) polarization was used to simulate illumination with vertically or horizontally polarized light, respectively, as viewed from the horizontal cross-section. The resulting simulations of the deposition using input illumination with TE polarization (Figure 2.6a) produced lamellar morphologies that were nominally identical to those observed experimentally (Figure 2a), with a pitch of 315 ± 11 nm and a width of 206 ± 11 nm. Well-defined, discrete absorption maxima were present in the tips of the lamellae. Modeling of the deposition using TM polarization (Figure 2.6b) produced a ridge morphology that also was nominally identical to the experimentally observed structure (Figure 2b), with uniform light absorption along the top of the ridge.

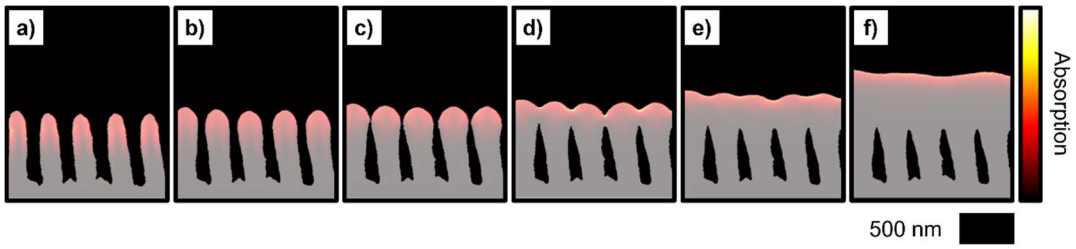

Figure 2.7. Simulated absorption profiles of deposit morphologies generated by two-dimensional modeling. Morphologies were initially generated using λ_0 = 843 nm with TE polarization ($E_0 \otimes$). Each panel presents profiles for successive growth modeling iterations using λ_1 = 843 nm with TM polarization ($E_1 \leftrightarrow$).

Figure 2.7 presents light absorption profiles that were obtained from successive modeling iterations of the morphology presented in Figure 2.6a for additional deposition that used λ_1 = 843 nm illumination with TM polarization. These simulated morphologies were nominally identical to the analogous

horizontal cross-sections observed experimentally (Figure 2). Initially, the magnitude and concentration of light absorption within individual features in Figure 2.7a was lower than that observed for illumination with TE polarization (Figure 2.6a). The absorption was substantial along the surface of the upper half of each lamella, with minimal absorption in the internal area of the deposit. As the feature width increased, the magnitude of optical absorption remained nearly constant, but became increasingly localized at the tips of the features (Figure 2.7b and c). The absorption then became concentrated at the interface of newly formed suspended, bridging sites between adjacent lamellae (Figure 2.7d). Upon further deposition, the light absorption became narrowly concentrated along the top surface, and the relief of this surface diminished (Figure 2.7e and f).

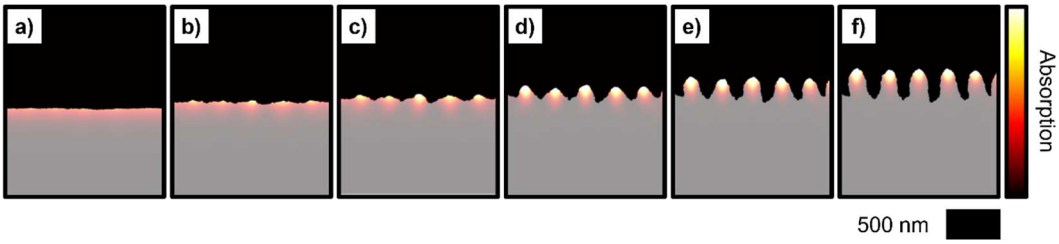

Figure 2.8. Simulated absorption profiles of deposit morphologies generated by two-dimensional modeling. Morphologies were initially generated using λ_0 = 843 nm with TM polarization (E_0 ↔). Each panel presents profiles for successive modeling iterations using λ_1 = 843 nm with TE polarization (E_1 ⊗).

Figure 2.8 presents light absorption profiles that were obtained from successive modeling iterations of the morphology depicted in Figure 2.6b for additional deposition using λ_1 = 843 nm illumination with TE polarization. These simulated morphologies were nominally identical to the analogous vertical cross-sections observed experimentally (Figure 2). The initial absorption profile (Figure 2.8a) was nominally identical to that observed in Figure 2.6b for TM-polarized

illumination. However, subsequent deposition of material disrupted the uniformity of the absorption along the top of the deposit (Figure 2.8b). Further addition of material resulted in spatially periodic absorption maxima along the top of the deposit (Figure 2.8c). The absorption maxima then exhibited regions of high magnitude that were isolated in spatially periodic, raised reliefs along the top of the deposit (Figure 2.8d). Further deposition did not substantially change either the concentration or magnitude of the absorption (Figure 2.8e and f). Rather, the reliefs elongated to form discrete lamellae in which light absorption was concentrated in the tips. The pitch and width of these lamellae was 316 ± 13 nm and 208 ± 12 nm, respectively.

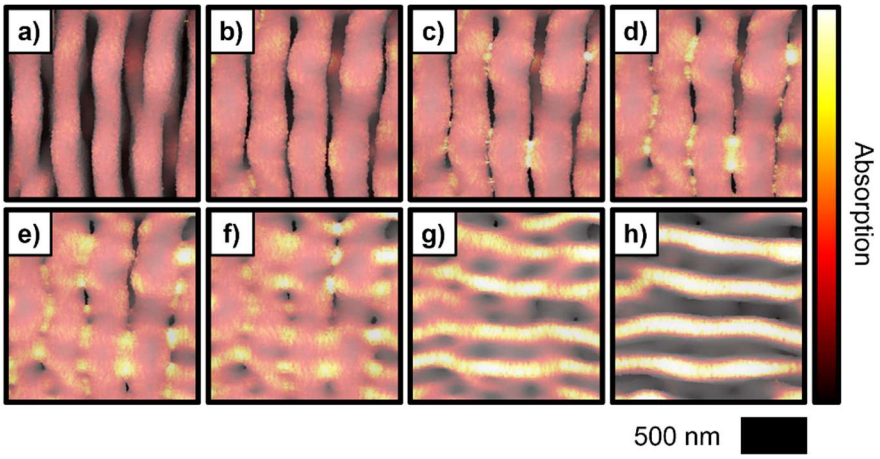

Figure 2.9. Simulated absorption profiles of deposit morphologies generated by three-dimensional modeling. Morphologies were initially generated using λ_0 = 843 nm with vertical polarization (E_0 ↕). Each panel presents profiles for successive modeling iterations using λ_1 = 843 nm with horizontal polarization (E_1 ↔).

Figure 2.9 presents light absorption profiles obtained from successive three-dimensional modeling iterations of a deposit morphology that was generated using λ_0 = 843 nm illumination with vertical polarization, followed by λ_1 = 843 nm illumination with horizontal polarization. The simulated data reproduced the stages

of the deposit morphology that were observed experimentally (Figure 2.1). In response to the polarization shift, the light absorption was uniform across the top surface of the lamellae (Figure 2.9a). The initial deposition of mass produced an increase in the width of the vertically oriented features. However, the light absorption across the features remained mostly uniform, with only a subtle increase in localized absorption in small, spatially discrete regions near the edges of the features (Figure 2.9b). Further deposition produced initial bridging between adjacent features, and resulted in intense, yet still small and highly spatially localized, areas of high absorption in the regions between preexisting vertically oriented lamellae (Figure 2.9c). As the deposition proceeded, these regions of high light absorption increased in both size and magnitude of absorption. The absorption however remained low and relatively unchanged along the preexisting vertically oriented lamellae (Figure 2.9d). As the deposition continued, bridge features developed further, and the regions of high absorption in the interlamellar space began to exhibit periodic spatial order along the vertical (Figures 9e and f). Regions of high absorption then fused horizontally across the vertically oriented lamellae, resulting in horizontally aligned bands of elevated absorption (Figure 2.9g). Concomitantly, the optical absorption decreased in the underlying vertically aligned lamellae. Eventually, the horizontally oriented lamellae became increasingly well-defined and exhibited high, uniform absorption along the entire length, with negligible absorption in the underlying vertically aligned lamellae (Figure 2.9h).

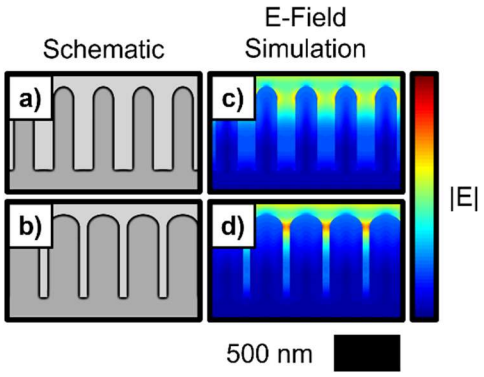

Figure 2.10. (a) Schematic of a simplified lamellar structure representative of the experimentally observed structure for deposition using λ_0 = 843 nm illumination with TE polarization (E_0 ⊗). (b) Same as (a) but for a structure with larger feature width. (c) and (d) Simulations of the time-average magnitude of the E-field resulting from illumination of simplified lamellar structures depicted in (a) and (b), respectively, with λ_1 = 843 nm with TM polarization (E_1 ↔).

Electromagnetic simulations of simplified structures provided further insight into the optical processes that controlled the structure development for deposition following an orthogonal shift in the direction of the polarization. Figure 2.10a presents a schematic of an idealized two-dimensional lamellar cross-section, with dimensions that are representative of deposits formed using λ = 843 nm illumination with TE polarization for Q = 1.000 C cm^{-2} (Figure 2a). Figure 2.10b presents a schematic that has an increased feature width but is otherwise identical to the structure depicted in Figure 2.10a. Figures 10c and 10d present simulated spatial profiles of the time-averaged magnitude of the optical E-field in response to illumination with λ = 843 nm light with TM polarization of the structures depicted in Figures 10a and 10b, respectively. For the idealized structure, void-space regions more than ~ 50 % beneath the height of the lamellae exhibited lower field magnitudes than the regions that had heights above that vertical distance (Figure 2.10c). The profile for the structure that had an increased feature width (Figure 2.10d) resembled that for the idealized structure (Figure 2.10c), but displayed an

increase in the magnitude of the optical E-field near the top of the sidewalls of the vertically oriented lamellae. The magnitude of the optical E-field increased across the full void space between adjacent lamellae.

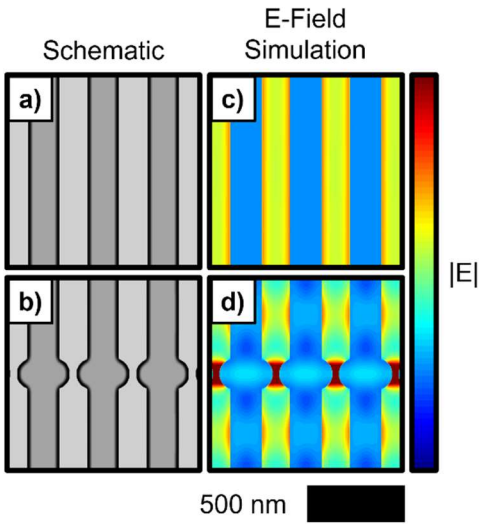

Figure 2.11. (a) Schematic of a simplified lamellar structure representative of the experimentally observed structures using λ_0 = 843 nm with vertical polarization (E_0 ↕). (b) Same as (a) but with features exhibiting a localized increase in width. (c) and (d) Simulations of the time-average magnitude of the E-field resulting from illumination of simplified lamellar structures depicted in (a) and (b), respectively, with λ_1 = 843 nm illumination with horizontal polarization (E_1 ↔).

Figure 2.11a depicts a plan-view schematic of an idealized lamellar structure with dimensions that are representative of deposits that were generated using λ = 843 nm illumination with vertical polarization for Q_0 = 1.000 C cm^{-2}. Figure 2.11b presents a schematic of structures similar to those depicted in Figure 2.11a but the structure in Figure 2.11b additionally had periodic, ellipsoidal expansions of material, with the expansions aligned across adjacent features. Figures 11c and 11d present simulated spatial profiles of the time-averaged magnitude of the optical E-field generated from illumination of the structures depicted in Figures 11a and 11b, respectively, with λ = 843 nm light having horizontal polarization. The magnitude of the optical E-field was low and mostly

uniform in the void space between features in the idealized structure, but the optical E-field increased in magnitude immediately adjacent to the edges of the features (Figure 2.11c). Moreover, the magnitude of the optical E-field in the voids varied periodically along the vertical direction (Figure 2.11d). Void regions adjacent to the expanded sites exhibited the highest magnitude of the optical E-field and were flanked on either side by local minima. Beyond these minima, the magnitude of the optical E-field was higher in the void space adjacent to edges of the features than in the tips of the features.

The agreement between the optically based modeling of the deposition (Figures 2.7-2.9) and the analogous experimental observations (Figures 2.1 and 2.2) indicates that photonic phenomena predominantly determined the morphologies at each state of woodpile development. Hence, the modeling is consistent with a mechanism in which woodpile formation proceeds through a series of several stepwise and concerted processes. In the first step, high, localized absorption at the tips of the features leads to formation of anisotropic lamellae (c.f. Figure 2.6a).[40] These lamellae scatter incident light that is polarized along the long axis of the structure towards adjacent features, enhancing light collection at the lamellar tips and continuing anisotropic deposition at steady state.

In the second step of the woodpile formation process, an abrupt orthogonal shift in the polarization disrupts the preceding steady state and reduces the spatial localization and magnitude of the absorption across the surfaces of the preexisting lamellae. Hence, the broadening proceeds at the lamellar tips (Figure 2.7a,b and

Figure 2.9a,b). Moreover, the intensity of the optical field increases in the narrowed void near the top of the sidewalls of the preexisting lamellae (Figure 2.10c,d). The enhancement of the optical field amplifies small, stochastic variations in the local rate of electrodeposition. After the lamellae broaden sufficiently, additional mass preferentially deposits with an orientation parallel to the new polarization, at the tips of the preexisting lamellae (Figure 2.1c). Positive feedback then yields further enhancement of the optical field and decreases the minimum distance between features across the preexisting lamellae (Figure 2.9c,d). Confinement of the enhanced optical field consequently produces bridging features across voids in the preexisting lamellar array (Figure 2.1d), rather than isotropic addition of material on the substrate and/or along the lamellar sidewalls.

The suspended bridging features initially do not exhibit collective spatial order, but continued deposition leads to the formation a periodic array of lamellae in the top layer of the woodpile structure (Figure 2.9c-f). The spatially directed deposition along the direction of the new polarization moreover leads to scattering of light parallel to the preexisting lamellar axis, producing an oscillatory optical field profile (Figure 2.11d), and resulting in formation of spatially periodic, suspended bridges. Upon further addition of material, the bridges coalesce to form a new lamellar structure with a long axis aligned parallel to the new polarization (Figure 2.9h). Further deposition then leads exclusively to continued development along the substrate normal of the lamellae that comprise the top layer of the woodpile. Hence, the data and simulations are consistent with a mechanism in

which formation of woodpile structures in response to an orthogonal polarization shift proceeds via a series of spontaneous yet concerted light-matter interactions. Figure 2.12 provides a graphical summary of this self-organizing deposition process.

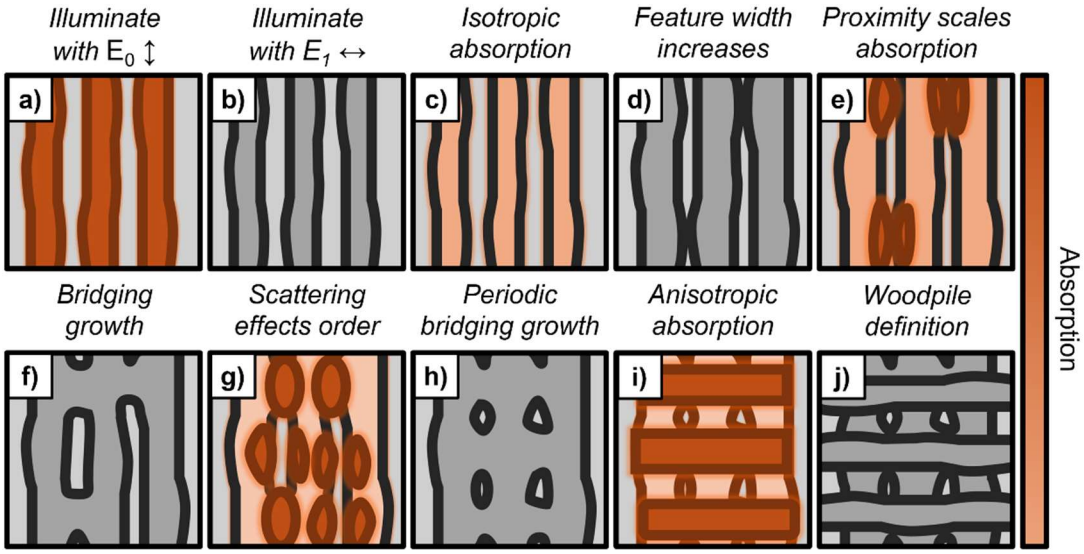

Figure 2.12. Schematic illustration of the stepwise mechanism of the deposition response to an abrupt shift in the polarization of the illumination from vertical (E_0 ↕) to horizontal (E_1 ↔). (a) Light absorption in vertically aligned lamellae for illumination with vertically polarized (E_0 ↕) light. (b)-(i) Alternating panels depict schematic deposit morphologies and the corresponding light absorption profiles for illumination with horizontally polarized (E_1 ↔) light. (j) Schematic of the resultant deposit morphology.

The light-directed electrodeposition method described herein enables facile, scalable generation of ordered nanoscale woodpile structures over macroscopic areas. Light-stimulated electrochemical deposition enables preparation of anisotropic, ordered lamellae of PbSe and CdSe so mesostructured woodpiles of these materials may also be formed via the use of orthogonal shifts in optical polarization deposition.[41,42] The mesoscale woodpiles are generated in a single continuous deposition process, without the use of lithography, structured light fields, or direct-write technology. The lack of any serial patterning suggests that the

deposition process may be scaled without a loss of throughput, and wafer-scale deposition may only require a light-source with sufficient output to uniformly illuminate the substrate. The technique enables systematic tuning of the pitch and height of each layer of the woodpile mesostructures via independent control of the illumination wavelength and charge, respectively during deposition. The electrodeposition method also ensures that all features are fully electrically addressable, facilitating integration into electrochemical system. The behavior observed herein highlights the potential of temporal optical manipulation to programmatically sculpt intricate mesostructures in a straightforward, scalable fashion.

2.3. Conclusions

Light-directed electrodeposition of Se-Te using an orthogonal shift in polarization effected the spontaneous, bottom-up production of three-dimensional woodpile structures. The height and pitch of the lamellae in each layer of the woodpile structure were independently controlled by variation of the charge density and wavelength of each polarized illumination input during deposition. The collective experiments and simulations performed in this work have elucidated the key steps in development of these mesoscale woodpile structures. First, an oriented array of lamellae forms via light-directed deposition under linearly polarized illumination. Then, a shift to the orthogonal polarization reduces the spatial localization and magnitude of the optical absorption in the lamellae, resulting in mass deposition that broadens the pre-existing lamellae. Concentration of light in the voids between lamellae then drives, and positively reinforces, spatially directed deposition from the lamellar tips into the voids. The deposition proceeds along the new direction of polarization, and continued feedback promotes the formation of suspended bridge features. Scattering at sites of the anisotropic deposition leads to periodic concentration of light perpendicular to the new direction of polarization and, consequently, to the formation of spatially periodic, bridging features. Eventually, consolidation of these suspended bridging features results in woodpiles. Generation of such complex three-dimensional mesostructures by manipulation of the illumination highlights the potential of light-directed electrodeposition to

constitute a scalable, lithography-free route to programmable three-dimensional nanoscale architectures.

C h a p t e r 3

PHOTONIC TEMPLATING OF INORGANIC PHOTOTROPIC GROWTH PRODUCES EXTENDED VERTICAL REGISTRATION IN MULTILAYERED MESOSTRUCTURES

Reich, N. D.; Lewis, N. S.; Carim, A. I. *In Preparation.*

3.1 Introduction

The precise morphologies produced by mesostructure generation via inorganic phototropic growth are a function of the illumination characteristics, e.g. linearly polarized illumination stimulates the growth of anisotropic lamellae with a feature pitch proportional to the wavelength.[43-45] Changing the illumination wavelength and/or polarization during growth can effect concomitant changes in the growth habit and consequently produce intricate three-dimensional structures including tuning forks, aqueducts, and woodpiles.[46,47] In this work, we report using a series of abrupt, orthogonal shifts in the optical polarization direction which can produce multi-layer morphologies with spatial registry and examine the photonic phenomena that underpin such formation of structural coherence.

3.2 Results and Discussion

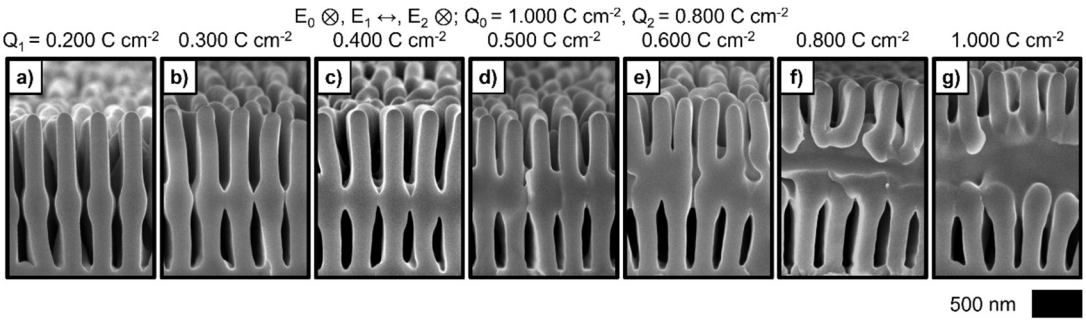

Figure 3.1. Representative cross-sectional SEMs of deposits generated using illumination first with TE polarization (E_0 ⊗) for Q_0 = 1.000 C cm^{-2}, followed by TM polarization (E_1 ↔) for the indicated Q_1, and then TE polarization (E_2 ⊗) for Q_2 = 0.800 C cm^{-2}.

Photoelectrochemical growth of Se-Te from an aqueous solution of fully oxidized precursors produced mesostructured deposits. A spatially uniform, linearly polarized light-emitting diode (LED) source with an intensity-weighted average emission wavelength of 843 nm supplied the photoexcitation. Figure 3.1 presents representative scanning-electron micrographs (SEMs) of deposits generated via a single photoelectrochemical growth process using three sequential optical polarization inputs. Transverse electric (TE) polarization (E_0 ⊗) was first supplied, followed by transverse magnetic (TM, E_1 ↔), and then TE again (E_2 ⊗). Deposition charge densities for the first and last polarization inputs remained fixed (Q_0 = 1.000 C cm^{-2}, Q_2 = 0.800 C cm^{-2}) and the deposition charge density for the intermediate polarization (Q_1) varied. For Q_1 = 0.200 C cm^{-2} (Figure 3.1a), deposition produced an ordered array of anisotropic lamellar features oriented along the substrate normal, and each feature exhibited a widened flare near the vertical midpoint. Increasing Q_1 to 0.300 C cm^{-2} (Figure 3.1b) generated a structure similar to that for Q_1 = 0.200 C cm^{-2} (Figure 3.1a) but with more pronounced flares that bridged neighboring features at the widest points. For Q_1 = 0.400 C cm^{-2}

(Figure 3.1c), deposition did not form discrete flared lamellae but instead produced a trilayer structure with ordered, anisotropic lamellae in the top and bottom layers separated by a uniform intermediate layer. For Q_1 = 0.500 C cm^{-2} (Figure 3.1d), deposition yielded a trilayer structure similar to that for Q_1 = 0.400 C cm^{-2} (Figure 3.1c) but with a larger uniform interlayer. For Q_1 = 0.600, 0.800, and 1.000 C cm^{-2} (Figure 3.1e-g), deposition produced structures similar to those for Q_1 = 0.500 C cm^{-2} (Figure 3.1d) and the expanse of the interlayer scaled with Q_1. Notably, for Q_1 = 0.400 and 0.500 C cm^{-2} (Figure 3.1c,d) lamellar features in the top layer appeared spatially well-aligned above features in the bottom layer. In contrast, for Q_1 = 0.800 and 1.000 C cm^{-2} (Figure 3.1f,g), some features in the top layer were aligned above features in the bottom layer, whereas other top layer features aligned above voids in the bottom layer.

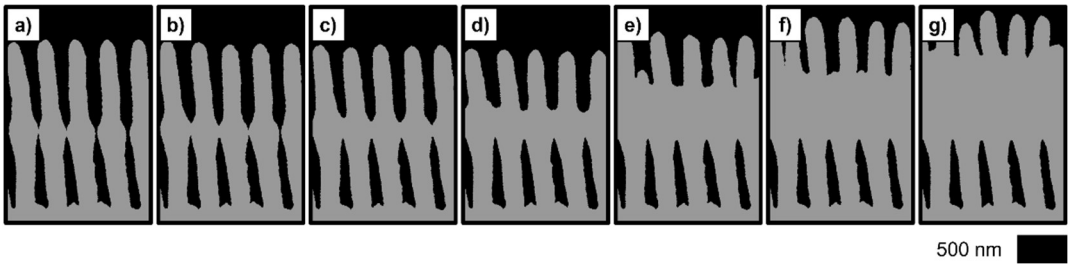

Figure 3.2. Morphologies generated by growth modeling using illumination first with TE polarization (E_0 ⊗), followed by TM polarization (E_1 ↔), and then TE polarization (E_2 ⊗), in a manner similar to that used experimentally to generate the deposits depicted in Figure 3.1. Panels arranged from left to right in order of increasing simulated growth at the TM polarization (E_1 ↔) step.

Computer modeling of the growth provided insight into the physical basis for spatial alignment between feature sets in multilayered structures. First, an electromagnetic simulation calculated the spatial profile of optical absorption at the electrochemical interface. Then, this absorption profile weighted the local probability of electrochemical growth via a probabilistic method. Successively

iterating these steps produced simulated morphologies. Empirical inputs to the modeling were limited to estimates of the complex refractive index of the material and the index of the electrolyte. Figure 3.2 presents simulations corresponding to the deposits in Figure 3.1, generated using the same sequence of three optical polarization inputs (TE, TM, TE) with increasing material addition at the second polarization (TM). In each case, the simulated morphologies were in close agreement with the experimental data. Moreover, the simulations corresponding to growth using $Q_1 < 0.600$ C cm^{-2} with the intermediate polarization input (TM, Figure 3.2a-d) reproduced the spatial alignment between the top and bottom layer features in the experimental data (Figure 3.1a-d). Additionally, the simulations corresponding to growth using $Q_1 \geq 0.600$ C cm^{-2} (Figure 3.2e-g) also reproduced the lack of such consistent alignment in the experimental data (Figure 3.1e-g). The agreement between the optically based simulations and the experiments suggests that the feature alignment between discrete layers is principally a consequence of photonic phenomena rather than crystallographic, electro-/chemical, and/or transport biases.[48-58]

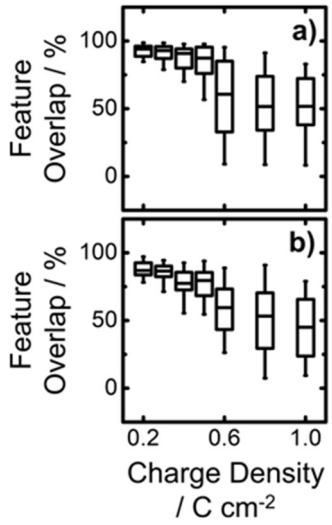

Figure 3.3. (a) Spatial overlap between lamellar features in the bottom and top layers of the structures presented in Figure 3.1 as a function of the deposition charge density (Q_1) used in conjunction with TM polarized (E_1 ↔) light to generate the middle layer. Box boundaries mark the lower and upper quartiles, the marker within the box indicates the median, and whiskers extend to the upper and lower 5% tails. (b) Same as (a) but for analogous data generated via growth modeling.

Figure 3.3a presents the normalized one-dimensional overlap of the horizontal extents of the features in the top and bottom layers of the structures presented in Figure 3.1 as a function of Q_1. This dataset quantifies the spatial alignment between the feature sets in alternate layers. For $Q_1 \leq 0.400$ C cm^{-2} the median overlap was > 90 %. For both $Q_1 = 0.200$ and 0.300 C cm^{-2} the interquartile range was ≤ 8 % whereas for both $Q_1 = 400$ C cm^{-2} the interquartile range was 13 %. These values indicate that for $Q_1 \leq 0.400$ C cm^{-2} top layer features preferentially grew directly above bottom layer features producing well-aligned features sets. For $Q_1 = 500$ C cm^{-2} the median overlap was 86 %, and the interquartile range was 29 %, which also indicates a substantial degree of preferential feature alignment, but lesser than that for $Q_1 \leq 0.400$ C cm^{-2}. For $Q_1 = 0.600$ C cm^{-2} the median overlap was 61 %, and the interquartile range was 52 %. Overlap > 50% indicates top features grew with some bias towards alignment above bottom layer features, but

the large interquartile range and overall magnitude of the distribution for $Q_1 = 0.600$ C cm^{-2} indicated that alignment substantially varied between individual feature pairs. For both $Q_1 = 0.800$ C cm^{-2} and $Q_1 = 1.000$ C cm^{-2} the median overlap was 52 % and the interquartile ranges were 34 and 39 % respectively. These values indicate that for $Q_1 > 0.600$ C cm^{-2} top layer features grew without any preferential bias toward alignment above a bottom layer feature but rather were almost equally likely to form centered above a bottom layer void. The collective overlap assessment demonstrates a growth bias for sufficiently small values of Q_1 (< 0.600 C cm^{-2}) that results in formation of top layer features in direct spatial registry with the bottom layer features. This bias is attenuated with increasing Q_1 but is operative even for sufficiently large values of Q_1 (> 0.300 C cm^{-2}) such that a uniform interlayer was produced between the top and bottom layers, precluding physical templating of growth.

Figure 3.3b presents overlap data analogous to that presented in Figure 3.3a but for the simulated morphologies presented in Figure 3.2. For $Q_1 < 0.600$ C cm^{-2} the assessment revealed substantial overlap with narrow distributions and thus indicates preferential spatial bias in the growth of the top layer features. For $Q_1 \geq 0.600$ C cm^{-2} the overlap values and distributions suggest a lack of a similar growth bias. Thus, the overlap analysis of the growth modeling data reproduced the trend derived from the experimental data (Figure 3.3a). This consistency further supports the notion that optical bias underpins the spatially preferential growth of the top layer structure.

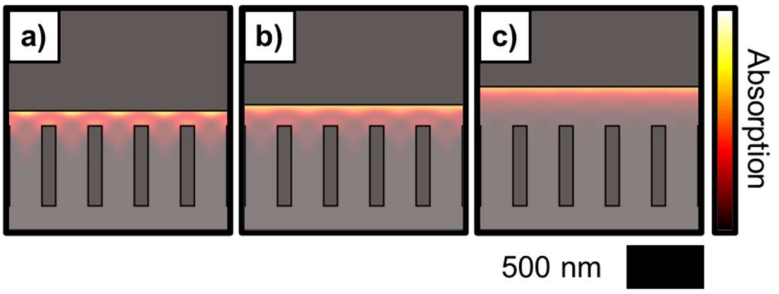

Figure 3.4. Simulated spatial profiles of the magnitude of absorption resulting from illumination of simplified structures with TE polarized (E_2 ⊗) light. Structures representative of morphologies generated via deposition using illumination first with TE polarization (E_0 ⊗) followed by TM polarization (E_1 ↔).

Simulations of light absorption in simplified model structures representative of morphologies generated via growth using TE polarization followed by TM polarization examined this optical bias. The model structures consisted of a uniform ridge feature above a transverse lamellar array. Figure 3.4a presents a simulated spatial profile of the absorption of TE polarized light for a structure with bottom layer and interlayer dimensions similar to those observed for growth using Q_1 = 0.400 C cm^{-2}. This profile exhibited periodic concentration of light absorption in the top of the ridge feature at locations centered above each of the underlying lamellae. This behavior is consistent with the spatial registry between the lamellar features in the top and bottom layers of the structure deposited using Q_1 = 0.400 C cm^{-2} (Figure 3.1c). Anisotropic deposition of lamellae via inorganic phototropic growth is a result of cooperative light-scattering amongst neighboring features that concentrates light in the feature tips.[59] Here, the incident light propagates through the ridge and is diffracted at the top of the lamellar array due to the substantial refractive index contrast between the lamellae (n = 3.68) and the voids (n = 1.33).[46] Notably, diffracted light projects through the ridge and shapes the intensity

distribution at the top, solution-facing interface which in turn shapes subsequent growth. Thus, growth at an isotropic interface is templated effectively by a physically remote structure via optical coupling. This phenomenon exemplifies a "history effect" in inorganic phototropic growth wherein subsequent growth is shaped not only by the instantaneous illumination characteristics but also by the preexisting structure.[60] However, in this case the templating does not select the growth habit but rather dictates only the relative feature position.

Figure 3.4b presents a simulated profile of light absorption similar to that in Figure 3.4a but for a structure with dimensions similar to those observed for growth using $Q_1 = 0.500$ C cm^{-2}. This profile also exhibited periodic absorption maxima in the top of the ridge aligned with the underlying lamellae. However, relative to Figure 3.4a these maxima were less well-defined and the absorption across the horizontal span of the ridge was more uniform. This result is consistent with the reduced, though nevertheless substantial, degree of preferential feature alignment in the trilayer structures generated using $Q_1 = 0.500$ C cm^{-2} relative to those generated using $Q_1 = 0.400$ C cm^{-2} (Figure 3.3a). The greater expanse of the ridge for $Q_1 = 0.500$ C cm^{-2} relative to $Q_1 = 0.400$ C cm^{-2} results in greater divergence of the diffracted light as it propagates across a longer path toward the top interface. This longer path also results in greater attenuation of both the incident and diffracted light. In concert, these effects reduce the optical confinement and thus the efficacy of the photonic templating.

Figure 3.4c presents an additional simulation similar to those presented in Figures 4a and b but for a structure with dimensions similar to those observed for

growth using Q_1 = 1.000 C cm^{-2}. This profile exhibited uniform light absorption across the ridge feature with no substantial periodic localization. The lack of horizontal variation in intensity is consistent with the lack of any horizontal spatial relation between the lamellar features in the top and bottom layers of the structure deposited using Q_1 = 1.000 C cm^{-2} (Figure 3.1g). Divergence and attenuation of the diffracted light decouples the intensity profile at the topmost interface from the influence of the bottom layer structure and thus removes the photonic template.

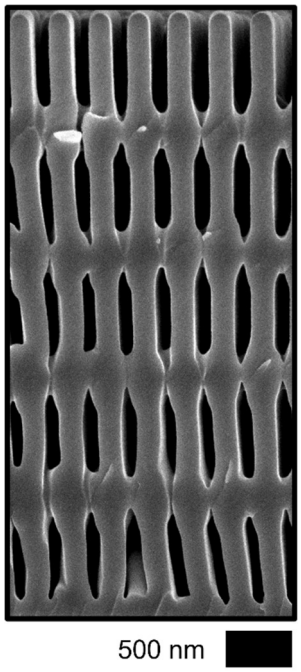

Figure 3.5. Representative cross-sectional SEM of a deposit generated using illumination initially with TE polarization (E_0 ⊗) for Q_0 = 1.000 C cm^{-2}, followed by four successive cycles of first TM polarization (E_1 ↔) for Q_1 = 0.350 C cm^{-2} and then TE polarization (E_2 ⊗) for Q_2 = 0.800 C cm^{-2}.

Figure 3.5 presents a representative SEM of a deposit generated via a single photoelectrochemical growth process with nine sequential optical polarization inputs. TE polarization (E_0 ⊗) was initially supplied for Q_0 = 1.000 C cm^{-2} followed by four successive cycles of first TM polarization (E_1 ↔) for Q_1 = 0.350 C cm^{-2} and then TE polarization (E_2 ⊗) for Q_2 = 0.800 C cm^{-2}. The deposit

exhibited a nine-layer structure consisting of five parallel layers of anisotropic lamellae periodically interspersed with four uniform intermediary layers. This structure displayed a substantial degree of vertical spatial registry as the lamellar features in each layer were well-aligned with the features in adjacent parallel layers. This result indicates that anisotropies intrinsic to the interaction between a uniform light field and the evolving deposit can be effectively leveraged to produce ordered three-dimensional lattices with extended structural coherence without lithographic processing including any need for precise, repeated photomask or pattern alignment.[61,62]

3.3 Conclusions

The cumulative data presented herein demonstrate that a uniform light field can stimulate ordered, anisotropic deposition at specific sites along an unpatterned interface with nanoscale precision. Such deposition is templated by a physically remote structure via optical coupling and enables spatially registered feature generation. The photonic templating phenomenon can be leveraged to enable programmable fabrication of multi-tiered architectures with extended structural coherence via inorganic phototropic growth with deliberate sequencing of optical inputs. Bottom-up, high-throughput synthesis in this manner may facilitate generation of photonic crystal structures, electrocatalyst and battery supports, and sensing platforms.[32-34,38]

Chapter 4

METHODS

This chapter details the experimental and computational methods used to generate the data presented in the preceding chapters.

4.1 Materials and Chemicals

H_2SO_4 (ACS Reagent, J. T. Baker), buffered HF improved etchant (Transene), SeO_2 (99.4 %, Alfa Aesar), and TeO_2 (99+ %, Sigma-Aldrich) were used as received. H_2O with a resistivity ≥ 18.2 MΩ cm (Barnstead Nanopure System) was used throughout. n^+-Si(100) (< 0.005 Ω cm, As-doped, 525 ± 25 μm, single-side polished, Addison Engineering) was coated with Pt as noted in section 4.2 and used as a substrate for deposition. Flash-Dry Ag Paint (SPI Supplies), EP21ARHTND Epoxy (MasterBond) and nitrocellulose-based nail polish were used to assemble the working electrodes.

4.2 Substrate Preparation

n^+-Si wafers were etched with buffered HF(aq) for 30 s, rinsed with H_2O, dried under a stream of N_2(g), and then immediately transferred to an electron-beam metal evaporator with a base pressure < 10^{-6} torr. Using an accelerating voltage of 10 kV, a 10 nm Ti adhesion layer was deposited on the polished side of the wafer using a 40 mA deposition current. 50 nm of Pt was then deposited on top of the Ti using a 70 mA deposition current. 20 nm of Ti was deposited on the unpolished side of the wafer to serve as a back-contact. The Pt-coated Si samples were then cut into square 0.50 cm by 0.50 cm sections for use as deposition substrates.

4.3 Electrode Preparation

Electrode assemblies were prepared by applying epoxy to the flat sides of each of two Al half-round bars (0.25 in diameter). The two bars were then joined together, with a ~ 10 mm offset in the axial dimension to form a cylinder with two half-round ends. Polytetrafluoroethylene heat-shrink tubing was used to insulate the cylindrical section of the bars, and epoxy was used to insulate the rounded side of one of the half-round ends. Ag paint was applied to the Ti-coated back surfaces of the Pt-topped Si sections, and the sections were affixed to the flat surface of the epoxied half-round end. The remaining uncovered area on the flat surface that surrounded the Pt-coated Si was insulated with nail polish. Immediately before deposition, the surface of each electrode was briefly cleaned using a stream of $N_2(g)$.

4.4 Electrode Illumination

Illumination for photoelectrochemical deposition was provided by narrowband diode (LED) sources (Thorlabs) with intensity-weighted average wavelength, λ, values and spectral bandwidths (FWHM) of 727 nm and 37 nm (M730L4), 843 nm and 30 nm (M850L3), and 934 nm and 55 nm (SOLIS-940C), respectively. A single aspheric lens (Ø50.8 mm, f = 32 mm) was used in conjunction with the λ_{avg} = 727 nm and 843 nm sources to collect, condense, and collimate the output. A series of three lenses, consisting of an aspheric lens (Ø25.4 mm, f = 16 mm) along with two bi-convex lenses (Ø50.8 mm, f = 60 mm and Ø50.8 mm, f = 100 mm) was used for the λ_{avg} = 934 nm source. A film polarizer (LPNIRE200-B, Thorlabs) was inserted after the lenses to produce and directionally orient the linear polarization. A 220 grit ground-glass (N-BK7) diffuser was placed immediately in front of the photoelectrochemical cell, to ensure the spatial homogeneity of the illumination.

The light intensity incident on the electrode was measured by placing a calibrated Si photodiode (Thorlabs FDS100), instead of an electrode assembly, in the photoelectrochemical cell with electrolyte, and the steady-state current response of that Si photodiode was measured. Depositions with λ = 727 or 843 nm were performed with a light intensity of 60 mW cm^{-2}, whereas depositions with λ = 934 nm were performed with a light intensity of 195 mW cm^{-2}.

4.5. Photoelectrochemical Deposition

Deposition was performed using a Bio-Logic SP-200 potentiostat. Deposition was performed in a two-compartment glass cell with a Pyrex window. A three-electrode configuration was utilized with a Ag/AgCl reference electrode (3.00 M KCl, Bioanalytical Systems) and an Ir wire counter electrode (99.999 %, Sigma-Aldrich) that was isolated behind a porous glass frit. The counter electrode was separated from the main compartment, to minimize contamination of the deposition substrate by any potential corrosion products or other species in the anolyte chamber. Deposits were produced from an aqueous solution of 0.0200 M SeO_2, 0.0100 M TeO_2, and 2.00 M H_2SO_4. Deposition was effected by biasing the Pt-coated electrode potentiostatically at -0.15 V vs. Ag/AgCl until the target charge density had passed. For depositions using two sequential, discrete illumination inputs, the electrode was transiently floated to open circuit after the initial deposition. The illumination input was then changed, and deposition was continued with the new illumination input by again by biasing the Pt-coated electrode potentiostatically at -0.15 V vs. Ag/AgCl until the target charge density for the second deposition step had passed. After deposition, the electrode was immediately removed from the cell, rinsed with H_2O, and dried under a stream of N_2(g). The Pt-coated substrate with a top-facing Se-Te deposit was mechanically separated from the rest of the electrode assembly. The nitrocellulose-based insulation and the majority of the Ag paint were then removed mechanically.

4.6. Scanning Electron Microscopy

Scanning-electron micrographs (SEMs) were obtained with a FEI Nova NanoSEM 450 at an accelerating voltage of 5.00 kV with a working distance of 5 mm and an in-lens secondary electron detector. Micrographs that were used to produce display figures were acquired with a resolution of 344 pixels μm^{-1} over ~ 2 μm^2 areas. Deposits were prepared in triplicate for each distinct photoelectrochemical growth condition, and micrographs were acquired from three separate spatial regions of each deposit. For each growth condition, the pitch of the lamellae was consistently within ± 5 % of the mean.

4.7. Energy Dispersive X-ray Spectroscopy

Energy dispersive X-ray (EDX) spectroscopy was performed in the SEM using an accelerating voltage of 15.00 kV and a working distance of 5 mm. An Oxford Instruments X-Max silicon drift detector was utilized. Spectra were collected in the range of 0 to 10 keV and quantitative deposit compositions were derived from these spectra using the “INCA” software package (Oxford Instruments).

4.8. Simulation of Deposit Morphology

Light-directed electrochemical deposition was simulated with an iterative model in which electromagnetic simulations were first used to calculate the local light absorption profile at the electrochemical interface. Then, mass addition was simulated via a Monte Carlo method wherein the local absorption weighted the local rate of mass addition along the deposit surface.

Two-dimensional simulations were discretized using a square mesh whereas three-dimensional simulations were discretized using a cubic mesh. To maximize the resolution of the simulations, the two-dimensional modeling used a lattice constant of 2 nm. The computational expense of three-dimensional solutions is exponentially higher than that of two-dimensional solutions. Consequently, to complete the simulations with the available computational resources, three-dimensional modeling was performed using a lattice constant of 7 nm. Deposition began with a bare, semi-infinite planar substrate. In the first step, the light-absorption profile under a linearly polarized, plane-wave illumination source with $\lambda = 843$ nm was calculated using full-wave finite-difference time-domain (FDTD) simulations ("FDTD Solutions" software package, Lumerical). Perfectly matched layer boundary conditions were used in the direction normal to the substrate, and periodic boundary conditions were used for the two orthogonal directions in the plane of the substrate. The wavelength-dependent complex refractive index of Se-Te has been measured previously, and a value of $n = 1.33$ was used as the refractive index of the electrolyte.[63]

In the second step, a Monte Carlo simulation was performed in which an

amount of mass, equaling that of a planar layer covering the simulation area with a thickness of 1 nm for two-dimensional simulations or a thickness of 5 nm for three-dimensional simulations, was added to the upper surface of the structure with a probability *F*:

$$F(A) = A\prod_{i=1}^{n}\frac{x_i}{r_i} \qquad \textbf{(Equation 1).}$$

Here, *A* is the spatially dependent absorption at the deposit/solution interface, *n* is the dimensionality of the simulation (2 or 3), x_i is the fraction of i^{th} nearest neighbors occupied in the lattice, and r_i is the distance to the i^{th} nearest neighbor. The multiplicative sum in the definition of this probability (Equation 1) serves to reduce the surface roughness of the deposit to mimic the experimentally observed surface roughness.

After the initial Monte Carlo simulation, the absorption of the new, structured deposit was calculated in the same manner as for the initial planar interface. An additional Monte Carlo simulation of mass addition was then performed. This process of absorbance calculation and mass addition was repeated until the simulated morphologies had heights equal to those of the experimentally generated deposits. To model the deposition using two sequential, discrete illumination inputs, the computational process was first iterated using the initial illumination input, until the simulated morphology height was equal to the height observed for the deposits generated experimentally. The simulated illumination was then updated to represent the new optical input, and the computational process was further iterated until the simulated morphologies had heights equal to those of the deposits generated

experimentally.

4.9. Electromagnetic Simulations Using Simplified Structures

Two and three-dimensional FDTD simulations were used to calculate the time-averaged magnitude of the optical E-field produced by illumination of idealized structures. A square simulation mesh with a lattice constant of 1 nm was used for the two-dimensional simulations, whereas a cubic simulation mesh with a lattice constant of 2 nm was used for the three-dimensional simulations. The illumination propagated along the substrate normal with the E-field vector oriented parallel to the substrate. Perfectly matched layer boundary conditions were imposed in the direction parallel to the propagation direction, whereas periodic boundary conditions were imposed in both perpendicular directions. The structures were designed to have dimensions in accord with the structures observed experimentally.

BIBLIOGRAPHY

(1) Autumn, K.; Liang, Y. A.; Hsieh, S. T.; Zesch, W.; Chan, W. P.; Kenny, T. W.; Fearing, R.; Full, R. J. Adhesive force of a single gecko foot-hair. *Nature* **2000**, *405*, 681-685.

(2) Liu, Y.; Wang, H.; Li, J.; Li, P.; Li, S. Gecko-Inspired Controllable Adhesive: Structure, Fabrication, and Application. *Biomimetics* **2024**, *9*, 149

(3) Watson, G. S.; Green, D. W.; Schwarzkopf, L.; Li, X.; Cribb, B. W.; Myhra, S.; Watson, J. A. A gecko skin micro/nano structure – A low adhesion, superhydrophobic, anti-wetting, self-cleaning, biocompatible, antibacterial surface. *Acta Biomaterialia* **2015**, *21*, 109-122

(4) Hawkes, E.; Christensen, D.; Cutkosky, M. 2019.

(5) Ball, P. Engineering Shark skin and other solutions. *Nature* **1999**, *400*, 507-509

(6) Bixler, G. D.; Bhushan, B. Fluid Drag Reduction with Shark-Skin Riblet Inspired Microstructured Surfaces. *Adv. Funct. Mater.* **2013**, *23*, 4507-4528.

(7) Kelleher, S. M.; Habimana, O.; Lawler, J.; O' Reilly, B.; Daniels, S.; Casey, E.; Cowley, A. Cicada Wing Surface Topography: An Investigation into the Bactericidal Properties of Nanostructural Features. *ACS Appl. Mater. Interfaces* **2016**, *8*, 14966-14974.

(8) Diu, T.; Faruqui, N.; Sjöström, T.; Lamarre, B.; Jenkinson, H. F.; Su, B.; Ryadnov, M. G. Cicada-inspired cell-instructive nanopatterned arrays. *Sci. Rep.* **2014**, *4*, 7122.

(9) Bhadra, C. M.; Werner, M.; Baulin, V. A.; Truong, V. K.; Kobaisi, M. A.; Nguyen, S. H.; Balcytis, A.; Juodkazis, S.; Wang, J. Y.; Mainwaring, D. E.; Crawford, R. J.; Ivanova, E. P. Subtle Variations in Surface Properties of Black Silicon Surfaces Influence the Degree of Bactericidal Efficiency. *Nano-Micro Letters* **2018**, *10*, 36

(10) Khatoon, Z.; McTiernan, C. D.; Suuronen, E. J.; Mah, T.-F.; Alarcon, E. I. Bacterial biofilm formation on implantable devices and approaches to its treatment and prevention. *Heliyon* **2018**, *4*.

(11) Ahmed, R.; Ji, X.; Atta, R. M. H.; Rifat, A. A.; Butt, H. Morpho butterfly-inspired optical diffraction, diffusion, and bio-chemical sensing. *RSC Adv.* **2018**, *8*, 27111-27118.

(12) Butt, H.; Yetisen, A. K.; Mistry, D.; Khan, S. A.; Hassan, M. U.; Yun, S. H. *Morpho* Butterfly-Inspired Nanostructures. *Adv. Opt. Mater.* **2016**, *4*, 497-504

(13) Betancourt, T.; Brannon-Peppas, L. Micro- and nanofabrication methods in nanotechnological medical and pharmaceutical devices. *Int. J. Nanomed.* **2006**, *1*, 483-495

(14) D, H.; Wai, S. Focused Ion Beam Lithography. In *Recent Advances in Nanofabrication Techniques and Applications*; Cui, B., Ed. 2011.

(15) Cox, L. M.; Martinez, A. M.; Blevins, A. K.; Sowan, N.; Ding, Y.; Bowman, C. N. Nanoimprint lithography: Emergent materials and methods of actuation. *Nano Today* **2020**, *31*, 100838

(16) Stuart, C.; Chen, Y. Roll in and Roll out: A Path to High-Throughput Nanoimprint Lithography. *ACS Nano* **2009**, *3*, 2062-2064

(17) Balslev, H. Tomlinson, P. B. 1990. The Structural Biology of Palms. *Nord. J. Bot.* **1991**, *11*, 152-152.

(18) Christie, J. M.; Murphy, A. S. Shoot phototropism in higher plants: New light through old concepts. *Am. J. Bot.* **2013**, *100*, 35-46

(19) Iwase, A.; Sakai, K.; Suzuki, A.; van Woesik, R. Phototropic adjustment of the foliaceous coral Echinopora lamellosa in Palau. *Estuarine, Coastal and Shelf Science* **2008**, *77*, 672-678

(20) Kaniewska, P.; Campbell, P. R.; Fine, M.; Hoegh-Guldberg, O. Phototropic growth in a reef flat acroporid branching coral species. *J. Exp. Bio.* **2009**, *212*, 662-667

(21) Meier, M. C.; Cheng, W.-H.; Atwater, H. A.; Lewis, N. S.; Carim, A. I. Inorganic Phototropism in Electrodeposition of Se–Te. *J. Am. Chem. Soc.* **2019**, *141*, 18658-18661.

(22) Sadtler, B.; Burgos, S. P.; Batara, N. A.; Beardslee, J. A.; Atwater, H. A.; Lewis, N. S. Phototropic growth control of nanoscale pattern formation in photoelectrodeposited Se–Te films. *Proc. Natl. Acad. Sci. U. S. A.* **2013**, *110*, 19707-19712

(23) Carim, A. I.; Batara, N. A.; Premkumar, A.; May, R.; Atwater, H. A.; Lewis, N. S. Morphological Expression of the Coherence and Relative Phase of Optical Inputs to the Photoelectrodeposition of Nanopatterned Se–Te Films. *Nano Lett.* **2016**, *16*, 2963-2968.

(24) Carim, A. I.; Batara, N. A.; Premkumar, A.; Atwater, H. A.; Lewis, N. S. Polarization Control of Morphological Pattern Orientation During Light-Mediated Synthesis of Nanostructured Se–Te Films. *ACS Nano* **2016**, *10*, 102-111

(25) Hamann, K. R.; Meier, M. C.; Lewis, N. S.; Carim, A. I. Plastic Morphological Response to Spectral Shifts during Inorganic Phototropic Growth. *JACS Au* **2022**, *2*, 865-874

(26) Ho, K. M.; Chan, C. T.; Soukoulis, C. M.; Biswas, R.; Sigalas, M. Photonic Band Gaps in Three Dimensions: New Layer-by-Layer Periodic Structures. *Solid State Commun.* **1994**, *89*, 413-416.

(27) Noda, S.; Tomoda, K.; Yamamoto, N.; Chutinan, A. Full Three-Dimensional Photonic Bandgap Crystals at Near-Infrared Wavelengths. *Science* **2000**, *289*, 604-606.

(28) Ogawa, S.; Imada, M.; Yoshimoto, S.; Okano, M.; Noda, S. Control of Light Emission by 3D Photonic Crystals. *Science* **2004**, *305*, 227-229.

(29) Joannopoulos, J. D.; Villeneuve, P. R.; Fan, S. Photonic crystals: putting a new twist on light. *Nature* **1997**, *386*, 143-149.

(30) Noda, S.; Fujita, M.; Asano, T. Spontaneous-emission control by photonic crystals and nanocavities. *Nat. Photonics* **2007**, *1*, 449-458.

(31) Ergin, T.; Stenger, N.; Brenner, P.; Pendry, J. B.; Wegener, M. Three-Dimensional Invisibility Cloak at Optical Wavelengths. *Science* **2010**, *328*, 337-339.

(32) Ge, J.; Yin, Y. Responsive photonic crystals. *Angew. Chem. Int. Ed.* **2011**, *50*, 1492-1522.
(33) Li, W.; Zhou, Y.; Howell, I. R.; Gai, Y.; Naik, A. R.; Li, S.; Carter, K. R.; Watkins, J. J. Direct Imprinting of Scalable, High-Performance Woodpile Electrodes for Three-Dimensional Lithium-Ion Nanobatteries. *ACS Appl. Mater. Interfaces* **2018**, *10*, 5447-5454.
(34) Kim, Y. J.; Lim, A.; Kim, J. M.; Lim, D.; Chae, K. H.; Cho, E. N.; Han, H. J.; Jeon, K. U.; Kim, M.; Lee, G. H.; Lee, G. R.; Ahn, H. S.; Park, H. S.; Kim, H.; Kim, J. Y.; Jung, Y. S. Highly efficient oxygen evolution reaction via facile bubble transport realized by three-dimensionally stack-printed catalysts. *Nat. Commun.* **2020**, *11*, 4921.
(35) Kim, K.; Lee, G. R.; Kim, M.; Lim, H.; Jung, Y. S.; Park, C. B. Metallic Woodpile Nanostructures for Femtomolar Sensing of Alzheimer's Neurofilament Lights. *ACS Nano* **2020**, *14*, 10376-10384.
(36) Zhou, Y.; Uzun, S. D.; Watkins, N. J.; Li, S.; Li, W.; Briseno, A. L.; Carter, K. R.; Watkins, J. J. Three-Dimensional CeO_2 Woodpile Nanostructures To Enhance Performance of Enzymatic Glucose Biosensors. *ACS Appl. Mater. Interfaces* **2019**, *11*, 1821-1828.
(37) Jeon, H. C.; Han, S. G.; Park, S.-G.; Yang, S.-M. Fabrication of microparticles with controllable internal woodpile structures for highly efficient sensing applications. *RSC Adv.* **2012**, *2*, 2334-2239.
(38) Chen, M.; Phang, I. Y.; Lee, M. R.; Yang, J. K.; Ling, X. Y. Layer-by-layer assembly of Ag nanowires into 3D woodpile-like structures to achieve high density "hot spots" for surface-enhanced Raman scattering. *Langmuir* **2013**, *29*, 7061-7069.
(39) Sadtler, B.; Burgos, S. P.; Batara, N. A.; Beardslee, J. A.; Atwater, H. A.; Lewis, N. S. Phototropic growth control of nanoscale pattern formation in photoelectrodeposited Se-Te films. *Proc. Natl. Acad. Sci. U. S. A.* **2013**, *110*, 19707-19712.
(40) Carim, A. I.; Meier, M. C.; Kennedy, K. M.; Richter, M. H.; Hamann, K. R.; Lewis, N. S. Assessing Effects of Near-Field Synergistic Light Absorption on Ordered Inorganic Phototropic Growth. *J. Am. Chem. Soc.* **2021**, *143*, 3693-3696.
(41) Carim, A. I.; Hamann, K. R.; Batara, N. A.; Thompson, J. R.; Atwater, H. A.; Lewis, N. S. Template-Free Synthesis of Periodic Three-Dimensional PbSe Nanostructures via Photoelectrodeposition. *J. Am. Chem. Soc.* **2018**, *140*, 6536-6539.
(42) Hamann, K. R.; Carim, A. I.; Meier, M. C.; Thompson, J. R.; Batara, N. A.; Yermolenko, I. S.; Atwater, H. A.; Lewis, N. S. Optically tunable mesoscale CdSe morphologies via inorganic phototropic growth. *J. Mater. Chem. C* **2020**, 12412-12417.
(43) Carim, A. I.; Batara, N. A.; Premkumar, A.; Atwater, H. A.; Lewis, N. S. Polarization Control of Morphological Pattern Orientation During Light-Mediated Synthesis of Nanostructured Se-Te Films. *ACS Nano* **2016**, *10*, 102-111.
(44) Carim, A. I.; Batara, N. A.; Premkumar, A.; May, R.; Atwater, H. A.; Lewis, N. S. Morphological Expression of the Coherence and Relative Phase of Optical

Inputs to the Photoelectrodeposition of Nanopatterned Se-Te Films. *Nano Lett.* **2016**, *16*, 2963-2968.
(45) Carim, A. I.; Batara, N. A.; Premkumar, A.; Atwater, H. A.; Lewis, N. S. Self-Optimizing Photoelectrochemical Growth of Nanopatterned Se-Te Films in Response to the Spectral Distribution of Incident Illumination. *Nano Lett.* **2015**, *15*, 7071-7076.
(46) Hamann, K. R.; Meier, M. C.; Lewis, N. S.; Carim, A. I. Plastic Morphological Response to Spectral Shifts during Inorganic Phototropic Growth. *JACS Au* **2022**, *2*, 865-874.
(47) Reich, N. D.; Lewis, N. S.; Carim, A. I. Mechanism of Mesoscale Woodpile Development via Photoelectrochemical Deposition of Se-Te. *ACS Nano* **2025**, *19*, 34869-34879.
(48) Vertegel, A. A.; Shumsky, M. G.; Switzer, J. A. Epitaxial Electrodeposition of Lead Sulfide on (100)-Oriented Single-Crystal Gold. *Angew. Chem. Int. Ed.* **1999**, *38*, 3169-3171.
(49) Liu, R.; Oba, F.; Bohannan, E. W.; Ernst, F.; Switzer, J. A. Shape Control in Epitaxial Electrodeposition: Cu_2O Nanocubes on InP(001). *Chem. Mater.* **2003**, *15*, 4882-4885.
(50) Carim, A. I.; Collins, S. M.; Foley, J. M.; Maldonado, S. Benchtop Electrochemical Liquid–Liquid–Solid Growth of Nanostructured Crystalline Germanium. *J. Am. Chem. Soc.* **2011**, *133*, 13292-13295.
(51) Mahenderkar, N. K.; Liu, Y.-C.; Koza, J. A.; Switzer, J. A. Electrodeposited Germanium Nanowires. *ACS Nano* **2014**, *8*, 9524-9530.
(52) Xiao, Z.-L.; Han, C. Y.; Kwok, W.-K.; Wang, H.-H.; Welp, U.; Wang, J.; Crabtree, G. W. Tuning the Architecture of Mesostructures by Electrodeposition. *J. Am. Chem. Soc.* **2004**, *126*, 2316-2317.
(53) Siegfried, M. J.; Choi, K.-S. Elucidating the Effect of Additives on the Growth and Stability of Cu_2O Surfaces via Shape Transformation of Pre-Grown Crystals. *J. Am. Chem. Soc.* **2006**, *128*, 10356-10357.
(54) Choi, K.-S. Shape control of inorganic materials via electrodeposition. *Dalton Trans.* **2008**, 5432-5438.
(55) Fleury, V.; Kaufman, J. H.; Hibbert, D. B. Mechanism of a morphology transition in ramified electrochemical growth. *Nature* **1994**, *367*, 435-438.
(56) Penner, R. M. Mesoscopic Metal Particles and Wires by Electrodeposition. *J. Phys. Chem. B* **2002**, *106*, 3339-3353.
(57) López, C. M.; Choi, K.-S. Electrochemical Synthesis of Dendritic Zinc Films Composed of Systematically Varying Motif Crystals. *Langmuir* **2006**, *22*, 10625-10629.
(58) Siegfried, M. J.; Choi, K. S. Elucidation of an overpotential-limited branching phenomenon observed during the electrocrystallization of cuprous oxide. *Angew. Chem. Intl. Ed.* **2008**, *47*, 368-372.
(59) Carim, A. I.; Meier, M. C.; Kennedy, K. M.; Richter, M. H.; Hamann, K. R.; Lewis, N. S. Assessing Effects of Near-Field Synergistic Light Absorption on Ordered Inorganic Phototropic Growth. *J. Am. Chem. Soc.* **2021**, *143*, 3693-3696.

(60) Hamann, K. R.; Carim, A. I.; Meier, M. C.; Lewis, N. S. Path-Dependent Morphological Evolution of Se-Te Mesostructures Prepared by Inorganic Phototropic Growth. *J. Am. Chem. Soc.* **2020**, *142*, 19840-19843.
(61) Totzeck, M.; Ulrich, W.; Göhnermeier, A.; Kaiser, W. Pushing Deep Ultraviolet Lithography to its Limits. *Nat. Photonics* **2007**, *1*, 629-631.
(62) Han, K. S.; Hong, S. H.; Kim, K. I.; Cho, J. Y.; Choi, K. W.; Lee, H. Fabrication of 3D nano-structures using reverse imprint lithography. *Nanotechnology* **2013**, *24*, 045304.
(63) Hale, G. M.; Querry, M. R. Optical Constants of Water in the 200-nm to 200-μm Wavelength Region. *Appl. Opt.* **1973**, *12*, 555-563.

A p p e n d i x A

COST-EFFECTIVE APPROACHES TO MAINTAINING RESOURCE ADEQUACY IN WIND AND SOLAR ELECTRICITY SYSTEMS OVER DECADES OF WEATHER VARIABILITY

Reich, N. D.; Ruggles, T. H.; Virgüez, E.; Dowling, J. A.; Caldeira, K.; Lewis, N. S.
Submitted

A.1 Introduction

Currently, twenty-four states, plus the District of Columbia and Puerto Rico, have set 100% clean energy or carbon-free electricity goals by 2050 or earlier.[23] However, high penetrations of wind and solar generation in electricity systems pose significant challenges to resource adequacy, which is generally quantified as a probabilistic measure of the system's ability to meet demand under uncertain conditions. Even assuming lossless transmission across a region, wind and solar generation fluctuate seasonally and daily. For example, across CONUS (contiguous United States), daily averaged solar generation output peaks in summer at 3.7 times the minimum daily averaged generation in winter, whereas the daily averaged wind generation is 3.5 times higher in winter than in summer.[24] Demand, in contrast to wind and solar power, varies seasonally by only a factor of 1.8 between spring and summer peaks. On many calendar days, same-day wind output spans approximately 0.3× to 3.0× the long-term mean wind generation. Smaller load-balancing areas exhibit even greater variability, including more frequent wind and solar "drought

days," defined as periods when the daily mean capacity factor remains below 50% of the long-term mean for that day of the year.[25] California, for example, experiences an average of 6.6 solar and 48 wind drought days annually over a 39-year period, compared to just 0.41 solar and 19 wind drought days per year in the larger Western Interconnect region.

Most studies of electricity systems dominated by variable renewable generation constrain the system to meet 100% demand and/or only utilize a year of wind and solar resource data. Modeling with a single year of data substantially underestimates the capacity needed to meet demand over multi-decade periods, the typical lifespan of assets on a grid.[26,27] In notional German electricity systems relying exclusively on wind and solar generation and planned using only a single year of weather data, the average hydrogen storage capacity was only half of that required to fully meet demand over multiple years of operation.[28,29] In a study that considered 36 years of wind resource variability, electricity systems that met hourly averaged demand in full for one planning year had a 35% chance of experiencing an outage that lasted at least 3 h when operated during a randomly selected operational year of weather variability.[30]

Another recent study investigating the planning of reliable electricity systems found that nearly forty years of weather data were required to design wind-, solar-, and storage-based systems that consistently met 100% of demand over a decade of historical weather variability in CONUS, whereas systems planned using only one year of weather data often failed to meet electricity demand over ten out-of-sample years, resulting in 0.082% lost load for a solar–wind–battery configuration.[31] These

findings indicate that the short planning horizons commonly used in models are inadequate for assessing the long-term reliability of renewable-based systems. However, such perfect-foresight planning is computationally demanding and often infeasible for higher-resolution or regional systems. This study examines how targeted, incremental capacity additions to generation and storage can improve reliability under unanticipated future weather, providing an adaptive analogue to reserve-margin planning for systems dominated by variable renewable generation. Our analysis builds on this framework by exploring a complementary approach that reflects real-world conditions in which system design is inherently based on limited data and future weather is unknown.

The present study evaluated cost-effective capacity additions that improved resource adequacy in systems dominated by variable renewable generation. Systems were planned using one year of weather data but were evaluated over four decades of weather and demand data across CONUS at 0.5° spatial resolution. Asset capacities in least-cost electricity systems were first determined using by demand matching at each timestep, consistent with current utility planning practice. To identify the additions that most improved adequacy with the lowest marginal cost, incremental capacity was then added by asset class. Resource adequacy was quantified as the percentage of met demand during operational years. Here, resource adequacy is evaluated in terms of inter-annual weather variability, recognizing that operational uncertainties such as forecast errors and unplanned outages increase the need for additional storage and/or dispatchable generation capacity. This long-term analysis captures wind and solar variability across the lifetime of grid infrastructure

and provides a guide to design reliable electricity systems under a deep decarbonization constraint.

A.2. Methods

Macro-Energy Model

A stylized, macro-scale energy model (MEM) was used to represent a continental-scale electricity system across CONUS.[26,31–35] Lossless transmission was assumed between generation and load over the whole CONUS load-balancing region. For consistency with prior literature, we refer to this framework as a "macro-energy" model, but the formulation used here does not include other energy sectors such as transportation or heating and is therefore more accurately characterized as a macro-electricity or macro-power system model.[25,26,31,32,36,37] In this context, the term macro-energy model refers to an analytical framework that captures long-term, system-scale behavior through simplified representations of technology and operation, allowing transparent evaluation of interactions between generation, storage, and reliability over large spatial and temporal domains.

To focus on the effects of daily, weekly, seasonal, and interannual weather variability, dispatched generation and dispatched stored energy were constrained to fully satisfy demand averaged over 4-hour time periods throughout a single year, hereafter referred to as the planning year, with energy balanced at each time step. This resolution was selected for the study to improve computational tractability when evaluating across multiple decades and for multiple system configuration, while still capturing the longer-timescale fluctuations in weather and renewable resource availability most relevant to this study. Prior work exploring the impact of temporal coarsening has found limited sensitivity of system outcomes to this level of

aggregation, as the weather events that most strongly influence system builds in capacity-expansion frameworks occur on multi-hour or longer timescales.[31,38,39]

Three energy systems, each with different available technologies (referred to as system architectures), were evaluated:

1. solar-wind-battery: electricity was supplied by wind and/or solar generation, with Li-ion batteries as an exemplary storage technology.
2. solar-wind-battery-H_2: electricity was supplied by wind and/or solar generation, with storage provided by Li-ion batteries and/or hydrogen energy storage and conversion technologies.
3. solar–wind–battery–natural gas (5% or 30%): electricity was supplied by wind and/or solar generation, storage was provided by Li-ion batteries, and natural gas combustion was available as firm dispatchable generation (5% or 30%). The mean natural gas dispatch was constrained to supply no more than 5% or 30% of the mean system demand over the simulation period.

The modeling process was divided into two stages. In the first stage, asset capacities and averaged dispatch values were calculated for a least-cost system based on a single (planning) year of wind and solar resource data and a single year of demand data. The model was constrained to supply all electricity demand at each time step, resulting in 100% resource adequacy for each system planning year. 42 such least-cost systems were obtained using weather data from each calendar year between 1979-2020. In the second stage of the process, the resource adequacy of the systems was evaluated across the entire dataset consecutively—the period 1979-

2020—using a dispatch-only mode, in which the asset capacities were fixed at the values obtained for the planning year. For each least-cost system obtained for a given planning year, additional capacity was obtained by multiplying the capacity of that technology by a selected scale factor. As referenced before, the MEM assumes a copper plate model (no transmission constraints or energy losses due to transmission). Hence, transmission costs were not included in the analysis. The expenditures reflect only the additional capital investments required to increase generation or storage capacity for each technology, against a baseline represented by the system without the additional generation or storage assets in place. These added capacity costs thus do not include any avoided costs or energy-delivery expenses. This additional, or extra, capacity is analogous to a reserve margin established to maintain resource adequacy in operational years relative to the resource availability in the planning year. Lost load (unmet demand) occurred if the specified asset capacities did not supply all demanded electricity at a given time step during the operational years. This study evaluated resource adequacy as the percentage of annual electricity demand met by energy dispatched from generation and storage assets. The North American Electric Reliability Corporation (NERC) BAL-502-RF-03 event-based standard for resource adequacy stipulates that, over each of the planning years analyzed, the cumulative probability of loss of hourly averaged load during any peak hour must not exceed 0.1, corresponding to an expectation of at most one such hourly loss-of-load event in a decade.[40] This criterion is often described as a “once in a decade” or “one-day-in-ten-years” standard and sets an event-based loss

of load criterion during a single peak hour within one day rather than for an entire day, or for 24 nonconsecutive hours in a decade, of unserved demand."[41,42]

In this analysis resource adequacy was evaluated by calculating the fraction of demand that was met during operation. Resource adequacy can also be measured as the number of events (loss of load hours, loss of load days, or loss of load years) for which 100% of demand is not met. Therefore, one possible interpretation of the resource adequacy standard of one hour of unmet demand in a decade is that any lost load in more than one individual hour falls below the resource adequacy standard. Another metric is to specify that the fraction of unmet demand must be not larger than an hour of unmet demand relative to mean demand, or 0.0011% of unmet demand. Both interpretations are used in reports on resource adequacy.[42] NERC has recommended that fraction of demand met, or expected served energy, be used instead of loss of load events as the new reliability metric, as it can be compared across systems of different sizes and load shapes. Expected served energy is used in other electricity markets internationally as the measure of resource adequacy. For example, Australia's National Energy Market (NEM) uses a 0.002% unserved energy standard. In this work, although our analysis uses a four-hour time resolution, we convert the "one-hour-in-a-decade" benchmark to an equivalent fraction of unmet energy demand (0.0011%), enabling direct comparison across temporal resolutions while maintaining consistency with the NERC standard.[42]

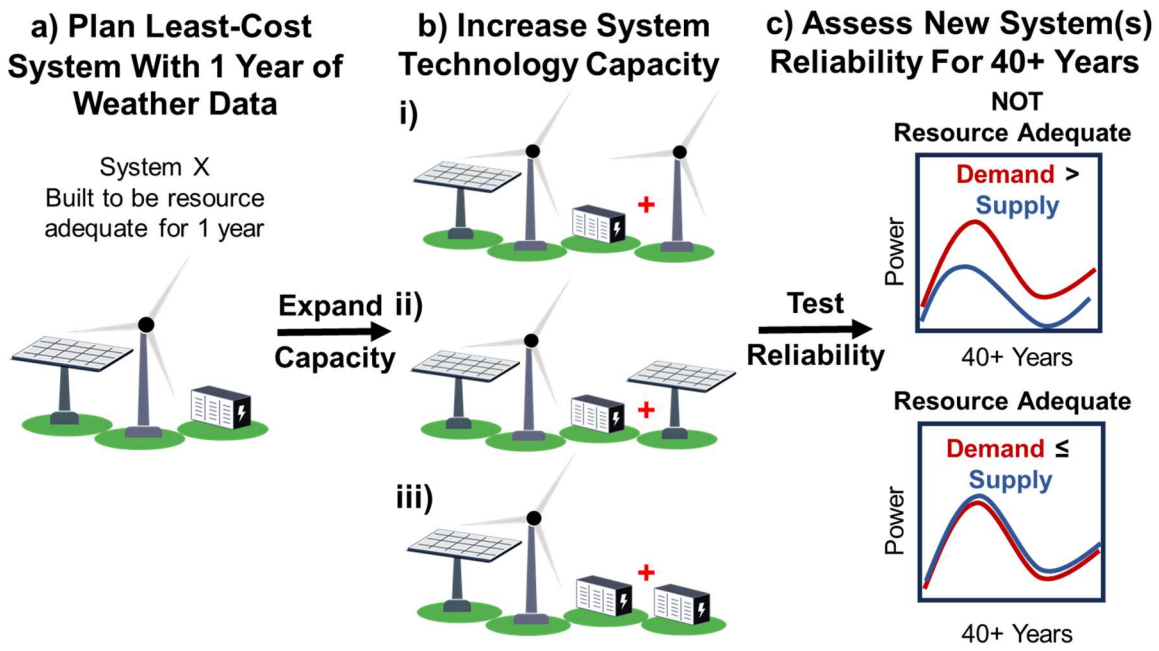

Figure A1. Schematic of the methodology used to construct and assess the performance of a solar-wind-battery electricity system. a) In the first phase, asset capacities were determined for a single (planning) year in a least-cost system that fully met demand throughout the planning year. b) The capacities of selected technologies in the system were then increased by additional expenditures on selected asset classes, and in the second phase c) the resulting system performance was determined during operation in all years of weather variability.

Model Inputs

Inputs to the model were based on cost estimates for currently available technologies. The fixed cost for each system asset included the cost for each component as well as the installation cost, including ancillary components and needs such as instrumentation, piping, electrical, buildings, and service facilities.[43] The calculated fixed hourly cost included the fixed capital investment as well as fixed annual operation and maintenance (O&M) costs, and thus had units of $/kW per hour for hourly fixed capacity costs and $/kWh per hour for hourly fixed energy capacity costs. Variable O&M and variable fuel costs were included as appropriate. Base case

costs for solar photovoltaics (PV), wind, and natural gas combined-cycle generation were obtained from the NREL (National Renewable Energy Laboratory) ATB (Annual Technology Baseline) report (Table 1).[44] Tables A1 presents the base case costs, efficiencies, and other characteristics for generation and storage technologies used in the model. Costs and technology characteristics for Li-ion batteries and hydrogen energy storage were obtained from the 2021 NREL analysis of long-duration energy storage technologies.[45] Li-ion batteries were modeled with a duration of 4 h.[45] Hydrogen energy storage was modeled with separate energy- and power-capacity components, and charging processes were assigned different power-capacity costs than discharging processes. For hydrogen energy storage, proton-exchange membrane (PEM) electrolyzers were used to split water; hydrogen was stored underground in salt caverns; and hydrogen was combined with O_2(g) in PEM fuel cells to generate power. The hydrogen storage leakage rate was based on leakage rates characteristic of hydrogen stored in pipelines, likely yielding an upper limit on the leakage rate of hydrogen storage in salt caverns considered herein. Wind and solar resources were represented by a time series of 4-hourly capacity factors derived from the ERA5 weather reanalysis data.[46] Solar capacity factors were calculated assuming a horizontal single-axis tracking system with a fixed tilt (0°–45°).[31,36] The solar panel power output was calculated based on the in-plane irradiance and module temperature.[47]

Wind resource availability was calculated for a wind turbine with a 100 m hub height and 1.6 MW nameplate capacity.[48] The turbines had a cut-in speed of 3 m/s, a maximum output at 12 m/s, and a cut-out speed of 25 m/s. Annual mean

resource availability was calculated for all of the assets deployed in the stylized system in each ERA5 grid cell. Aggregate time series were then produced using an area-weighted average of the 25% of these ERA5 cells that had the highest annual capacity factors. This aggregation smoothed the resource profiles by averaging over a quarter of the CONUS cells, thus producing a less variable profile along with using the most productive regions.

Our historical weather dataset had a mean wind capacity factor of 29% and a mean solar capacity factor of 26%, as compared to the US mean capacity factor of 35% and 25%, respectively, for installed wind and solar projects.[49–51] With the variability calculated using the relative standard deviation, the variability within our 42-year dataset in the calculated mean of the annual capacity factors was 4.8% for wind generation and 1.49% for solar generation. The reported solar capacity factor represents a conceptual estimate of the total energy available from solar generation and is calculated on a direct current (DC) basis.

A synthetic demand profile was constructed for each year by preserving possible correlations between wind and solar availability and electricity load. In this approach, future peak electricity demands and load profiles were used to calculate plausible electricity demand across CONUS.[52] Specifically, a predictor of historical electricity use was constructed as a function of temperature, based on US building stock information and US Census 2010 American Community Survey data. These predictors minimized the sum of squares between the predicted monthly electricity usage and actual 2010 monthly state-level electricity usage for each building class. Using these methods and historical hourly ERA5 temperatures values, plausible

hourly electricity loads were calculated for a 2010-type building stock for years 1979 through 2020, concurrent with the wind and solar resource profiles. The calculations were performed at the census track level and then were aggregated together to produce a total value for CONUS.

Model Formulation

Table A1. Techno-economic values for electricity technologies

Economic parameter	**Solar PV**[44]	**Wind**[44]	**Combined-cycle gas turbine**[44]	**Utility-scale battery storage**[53]*		**PEM Electrolysis facility**[53]	**Salt cavern H_2 storage**[53]	**PEM fuel cell**[53]
Fixed capital cost $\left(\frac{\$}{kW_e}\right)$	1391	1436	1054	Energy: 326 $\frac{\$}{h\ kW_e}$	Power: 251 $\frac{\$}{kW_e}$	1706	2.0	1415
Fixed O&M cost $\left(\frac{\$}{yr.kW_e}\right)$	23	43	27	Energy: 4.2 (% of capital cost)	Power: 8.5	13.1	1.5 (% of capital cost)	13.1
Fixed property tax, insurance, licensing, permitting (% of capital cost)	-	-	-	-	Power: 1.5%	1.5%	-	1.5%
Lifetime (yr)	30	30	30	30		30	30	30

Capital Recovery Factor ($\frac{\%}{yr}$)	8.06	8.06	8.06	8.06	8.06	8.06	8.06
Heat rate ($\frac{Btu}{kWh}$)	-	-	6,360	-	-	-	-
Fixed hourly cost ($\frac{\$}{h\ kW_e}$)	0.015	0.018	0.013	0.0039($\frac{\$}{h\ kWh_e}$)	0.01742	1.87×10^{-5}	0.01470
Relative efficiency	-	-	54%	86% round-trip	50%	-	71%
Decay Rate	-	-	-	1% per month	0.1% per day		
Variable O&M cost ($\frac{\$}{kWh_e}$)	0	0	0.002	3×10^{-6}	1.3×10^{-6}	0	2.8×10^{-6}
Variable fuel cost ($\frac{\$}{kWh_e}$)	-	-	0.008	-	-	-	-
Total variable cost ($\frac{\$}{kWh_e}$)	0	0	0.01	3×10^{-6}	1.3×10^{-6}	0	2.8×10^{-6}

*Source separates energy and power components for Li-ion battery storage, but we assume a 4 h duration with non-separated energy and power.
**Calculations are based on our assumed discount rate of 7%.

Table A2. Model nomenclature

Symbol	**Unit**	**Description**

g	label only	Generation technology (wind, solar, natural gas)
s	label only	Energy storage technologies (Battery, H2)
v	label only	Energy conversion (electrolysis facility, fuel cell)
l	label only	Energy not supplied (lost load)
$x\ to\ y$	label only	Energy from 'x' to 'y' (grid to battery, battery to grid, grid to H2, H2 to grid)
t	h	Time step, starting from 1 and ending at T
c_{cap}	$(\frac{\$}{kW_e})$for generation and electrolysis facility, $\left(\frac{\$}{kWh_e}\right)$ for battery storage, $\left(\frac{\$}{kWh_{LHV}}\right)$ for H_2 storage, $\left(\frac{\$}{kW_{LHV}}\right)$ for fuel fell	(Overnight) capital cost
$c_{fixed\ O\&M}$	$(\frac{\$}{yr \cdot kW_e})$ for generation, $(\frac{\$}{yr \cdot kWh_e})$ for storage	Fixed operating and maintenance (O&M) cost
c_{fixed}	$(\frac{\$}{h \cdot kW_e})$ for generation, $(\frac{\$}{h \cdot kWh_e})$ for storage	Fixed cost
c_{var}	$\left(\frac{\$}{kWh_e}\right)$	Variable cost (natural gas with CCS)
f	unitless	Capacity factor (generation technology, f = 1 for all t for natural gas)
h	*h/yr*	Number of hours per year
i	unitless	Discount rate
n	*yrs*	Asset lifetime
Δt	h	Time step size, i.e., 1 hour in the model
C	kW_e for generation, kWh_e for storage	Capacity
D_t	kW_e	Dispatch at time step t from generation or energy storage assets
M_t	kW_e	Electricity load at time step t
u_t	kW_e	Curtailed power
S_t	kWh_e for battery, kWh_{LHV} for H_2	Energy in battery or H_2 storage at end of time step t
L_t	$k\ kWh_e$	Energy supply shortfall at time step t (lost load)

γ	$1/yr$	Capital recovery factor
δ	$1/h$	Storage decay rate (energy loss per hour) expressed as fraction of energy in storage
η	unitless	Round-trip efficiency (all energy storage assets)
τ	h	Storage charging duration
exp_{add}	$\left(\frac{\$}{kWh_e}\right)$	Value of expenditure on additional capacity

A capital recovery factor (Eq. 1) using n, the lifetime of the associated asset, was used to calculate the fixed hourly costs for the generation assets (wind, solar, natural gas combined cycle), the energy conversion assets (electrolysis facility and fuel cell) and the battery storage asset (Eq. 2).

$$(1)\ \gamma = \frac{i(1+i)^n}{(1+i)^n-1}$$

$$(2)\ c_{fixed} = \frac{\gamma c_{cap} + c_{fixed\ O\&M}}{h}$$

The generation, conversion, and storage asset capacities are constrained to be greater than or equal to zero (Eq. 3) with associated power flows for each time step, t, constrained by the capacities (Eqs. 4 & 5). The $f_{t,g}$ value was 1 for all assets except wind and solar generation, in which $f_{t,g}$ represents the mean wind or solar capacity for that time step. Lost load had an associated capacity constraint and was forced to equal zero for all initial system build optimizations (Eq. 6).

$$(3)\ 0 \leq C_{g,v,s}$$

$$(4)\ 0 \leq D_{t,g} \leq C_g f_{t,g}$$

$$(5)\ 0 \leq D_{t,v} \leq C_v$$

$$(6)\ 0 \leq L_t$$

The battery charging and discharging rates were limited by the asset capacity and the power-to-energy ratio, which was 4 for the modeled Li-ion technology (Eqs. 7 & 8). The rates for charging and discharging the H_2 storage were limited by the capacities of the conversion technologies (electrolysis facility and fuel cells (Eqs. 9 & 10)). The stored energy in the grid battery and H_2 storage (if included in the system) were less than or equal to the energy storage capacities (Eq. 11) and the total dischargeable energy was limited by the decay rates (Eq. 12).

$$(7)\ 0 \leq D_{t,grid\ to\ batt} \leq \frac{C_{batt}}{\tau_{batt}}$$

$$(8)\ 0 \leq D_{t,batt\ to\ grid} \leq \frac{C_{batt}}{\tau_{batt}}$$

$$(9)\ 0 \leq D_{t,grid\ to\ H_2} \leq C_{electrolysis}$$

$$(10)\ 0 \leq D_{t,H_2\ to\ grid} \leq C_{fuel\ cell}$$

$$(11)\ 0 \leq S_{t,s} \leq C_s$$

$$(12)\ 0 \leq D_{t,s\ to\ grid} \leq S_{t,s}(1-\delta_s)\Delta t$$

1. Initial capacity build optimization

In the first step, where an initial capacity build optimization was performed, energy balance was maintained for the electricity node, and for the hydrogen node if included, for all time steps. The grid battery storage asset maintained balance, including at the start and end of each simulation, according to Eq. 13 and Eq. 14. Grid energy balance was maintained by balancing all sources (generation, discharge from grid battery, and conversion from H_2 via the fuel cell, lost load) against all sinks (load, battery charging, and conversion to H_2 via the electrolysis facility, generation curtailment) (Eq 17). The hydrogen energy balance used in the solar-wind-battery-H_2 system is described in Eqs. 15 & 16, like Eqs. 13 & 14 used for battery storage.

$$(13)\ S_{1,batt} = (1-\delta_s)S_{T,batt}\Delta t + \eta_{batt}D_{T,grid\ to\ batt}\Delta t - D_{T,batt\ to\ grid}\Delta t$$

$$(14)\ S_{t+1,batt} = (1-\delta_s)S_{t,batt}\Delta t + \eta_{batt}D_{t,grid\ to\ batt}\Delta t - D_{t,batt\ to\ grid}\Delta t$$
$$t \in 1, \dots, (T-1)$$

$$(15)\ S_{1,H_2} = \left(1-\delta_{H_2}\right)S_{T,H_2}\Delta t + \eta_{H_2}D_{T,grid\ to\ H_2}\Delta t - D_{T,H_2\ to\ grid}\Delta t$$

$$(16)\ S_{t+1,,H_2} = \left(1-\delta_{H_2}\right)S_{t,H_2}\Delta t + \eta_{electorlyzer}D_{t,grid\ to\ H_2}\Delta t - D_{t,H_2\ to\ grid}\Delta t$$
$$t \in 1, \dots, (T-1)$$

$$(17)\ \sum_g D_{t,g}\Delta t + D_{t,batt\ to\ grid}\Delta t + \eta_{fuel\ cell}D_{t,H_2\ to\ grid}\Delta t = M_t\Delta t + D_{t,grid\ to\ batt}\Delta t + D_{t,grid\ to\ H_2}\Delta t + u_t\Delta t$$

The model minimized the system cost for each initial simulation (Eq. 18) by optimizing the installed generation, conversion, and battery storage asset capacities and dispatch at each time step.

$$(18)\ system\ cost = \sum_{g,v,s} c_{fixed\ g,vc,}C_{g,v,s} + \sum_g \left(\frac{\sum_t c_{var,g}D_{t,g}}{T}\right)$$

The average cost of electricity, or the levelized cost of electricity (LCOE), was calculated as the system cost divided by the average annual load for the dataset, which was 304,000 kWh (Eq. 19).

$$(19)\ Levelized\ cost\ of\ electricity = \frac{system\ cost}{304000}$$

2. Expenditure on increased asset capacities

In the second step, the effects of increased capacity expenditure were assessed with respect to improvements in resource adequacy. A new capacity for each technology was generated by adding an additional capacity to the original solved capacity obtained in step 1. This additional capacity was equivalent to how much capacity could be bought by an additional expenditure (exp_{add} in \$/kWh) (Eq. 20).

$$(20)\ C_{new} = C_{original} + \left(\frac{exp_{add}*304000}{c_{fixed}}\right)$$

The values of exp_{add} used for each system architecture are presented in Table A3.

Table A3. Expenditure made on capacity.

System Architecture	exp_{add} (\$/kWh)
Solar-wind-battery	0, 0.005, 0.01, 0.025, 0.05, 0.075, 0.1, 0.25, 0.5, 0.75, 1.0
Solar-wind-battery-H_2	0, 0.005, 0.01, 0.025, 0.05, 0.075, 0.1, 0.25, 0.5, 0.75, 1.0

Solar-wind-battery-5% NG	0, 0.005, 0.01, 0.05, 0.1, 1.0
Solar-wind-battery-30% NG	0, 0.005, 0.01, 0.05, 0.1, 1.0

3. Dispatch-only reliability test

In the third step, when the model was run in dispatch-only mode, the asset capacities solved for in the first step were held constant. When system builds were being tested for resource adequacy, only the dispatch at each time step of each technology was allowed to vary in the cost minimization process. Grid energy balance was still maintained by balancing all sources as in the first step, but now lost load was included as a generation technology (Eq. 21). The cost of lost load during tests, $c_{var,l}$, was \$10/kWh, substantially greater than all other variable costs.[14]

$$(21)\ \sum_g D_{t,g}\Delta t + D_{t,batt\ to\ grid}\Delta t + \eta_{fuel\ cell} D_{t,H_2\ to\ grid}\Delta t + L_t\Delta t = M_t\Delta t + D_{t,grid\ to\ batt}\Delta t + D_{t,grid\ to\ H_2}\Delta t + u_t\Delta t$$

The model still minimized the system cost for each initial simulation (Eq. 22), but could not optimize the installed generation, conversion, and battery storage asset capacities, which were fixed. Instead, the system cost could be minimized by optimizing only dispatch at each time step, including lost load. The LCOE was calculated using Eq. 23.

$$(22)\ system\ cost = \sum_{g,v,s} c_{fixed\ g,vc,} C_{g,v,s} + \sum_g \left(\frac{\sum_t c_{var,g} D_{t,g}}{T}\right) + \frac{\sum_t c_{var,l} L_t}{T}$$

$$(23)\ LCOE = \frac{(\sum_{g,v,s} c_{fixed\ g,vc,} C_{g,v,s} + \sum_g \left(\frac{\sum_t c_{var,g} D_{t,g}}{T}\right) - \frac{\sum_t c_{var,l} L_t}{T})}{304000}$$

The met demand (% mean demand) was calculated as the average lost load, L_t, subtracted from the average load across the dataset, normalized to the average load across the dataset (Eq. 24).

$$(24)\ Met\ demand = \frac{304000 - \sum_t L_t}{304000} \times 100\%$$

Table A4. Mean capacities for initial least-cost optimizations run for a single year. Capacities are presented as averages of the values obtained for all 42 single-year-systems.

Technology	**Capacity unit**	**Solar-wind-battery**	**Solar-wind-battery-H_2**	**Solar-wind-battery-5% natural gas**	**Solar-wind-battery-30% natural gas**
Solar	% mean demand	240	110	140	100
Wind	% mean demand	650	350	410	180
Utility-battery storage	Useful energy as hours of mean demand	6.9	0.9	0.3	0.3
Hydrogen electrolysis facility	% mean demand	--	20	--	--
Salt cavern hydrogen storage	Useful energy as hours of mean demand	--	490	--	--
Hydrogen fuel cell	% mean demand	--	70	--	--
Natural Gas generation	% mean demand	--	--	75	100
System Cost	($\$/kWh_e$)	0.188	0.132	0.097	0.063

Table A5. Met demand (as percentage of average CONUS demand) when single-year-systems are operated on the "future" decades of weather. As 42 least-cost systems were evaluated as part of this study, results are reported as the minimum met demand (the lowest percentage of demand met by any single system), the median met demand (the middle value across all systems), and the maximum met demand (the highest percentage of demand met by any single system).

System Architecture	**Minimum Met Demand**	**Median Met Demand**	**Maximum Met Demand**
Solar-wind-battery	99.67%	99.91%	99.99%
Solar-wind-battery-H_2	96.51%	98.27%	99.96%
Solar-wind-battery-5% natural gas	98.57%	99.56%	100%
Solar-wind-battery-30% natural gas	96.59%	99.75%	99.99%

A.3 Results and Discussion

The solar-wind-battery system represents an example of a stylized fully decarbonized electricity system based on variable renewable generation with only short-duration energy storage. In contrast, in the solar-wind-battery-hydrogen system, wind and solar generation can be used by an electrolysis facility to split water and produce hydrogen, which can then be stored at high pressure in salt caverns. If demand cannot be satisfied by wind and solar resources, and hydrogen storage reserves are not depleted, hydrogen fuel cells would combine hydrogen and oxygen to produce water and electricity on demand and thus balance the grid. This power-to-gas-to-power hydrogen energy storage provides an exemplary long-duration storage technology that may ease reliability and affordability challenges of electricity grids based predominantly on variable renewable generation.[26,29,54] However, other long duration energy storage technologies can, in principle, serve similar roles, such as compressed air energy storage or pumped hydro storage, provided that they can be deployed at the required scale.[32,36,55,56]

First, least-cost systems were obtained for each calendar year from 1979 to 2020 using that year as the planning year weather input. These systems were then evaluated over 42 operational years to assess their ability to meet demand under multiple decades of resource variability. In agreement with previous studies, least-cost systems obtained using a single planning year of weather data did not reliably meet demand in all operational years (Table A6).[30,31,57] For this study, resource adequacy was evaluated as the percentage of annual electricity demand that was met by dispatched energy from generation and storage assets, referred to as met demand.

The threshold for resource adequacy was set at 99.9989%, reflecting a conversion of the NERC "one-hour-in-a-decade" standard into an equivalent metric applicable to a model with coarser temporal resolution.[42] The "minimum met demand" reported in all figures refers to the lowest average percentage of demand met across all operational years by any one of the 42 systems. This metric captures the performance of the system that was most stressed by interannual resource variability and is therefore the most important to improve. For both the solar-wind-battery and solar-wind-battery-H_2 systems, the mean and minimum satisfied load values were substantially less than 99.9989% of demand over the full operational period.

Table A6. Demand met (as percentage of average CONUS demand) when single-year-systems were operated on "future" decades of weather. 42 least-cost systems were evaluated as part of this study, so the results are reported as the minimum met demand (the lowest average percentage of demand met by any single system), the median met demand (the median average percentage of demand across all systems studied), and the maximum met demand (the highest average percentage of demand met by any single system).

System Architecture	Minimum Met Demand	Median Met Demand	Maximum Met Demand
Solar-wind-battery	99.67%	99.91%	99.99%
Solar-wind-battery-H_2	96.51%	98.27%	99.96%

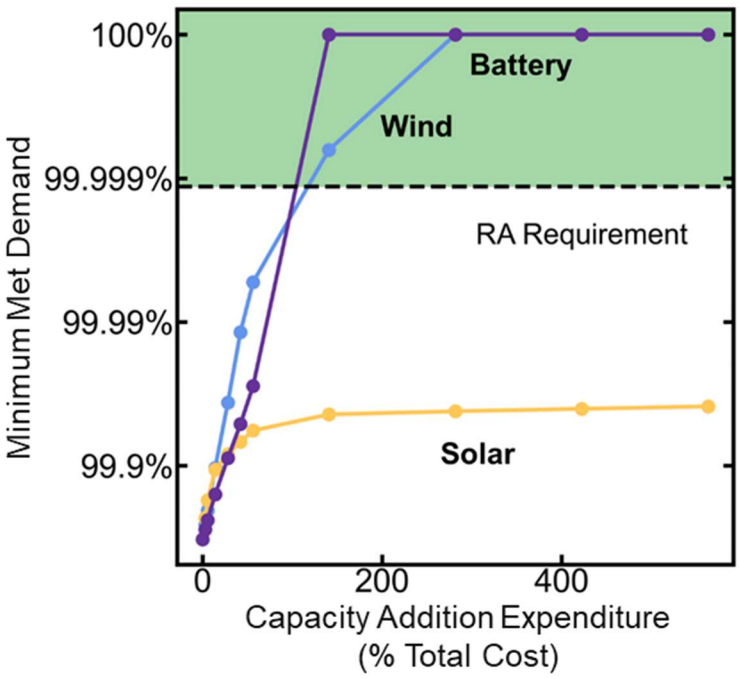

Figure A2. Impact of capacity addition expenditures on resource adequacy when electricity was supplied by wind and solar generation in conjunction with Li-ion battery storage. An expenditure was made for least-cost systems that met 100% of hourly averaged demand in each of the 42 planning years to increase wind generation capacity (blue), solar generation capacity (yellow), or battery storage capacity (purple). These systems were then operated over the full 42-year period, and the demand met during operation is reported as a percentage of mean demand. This figure displays the minimum met demand (the lowest average percentage of demand met by any single system) so the data is displayed for the system that had the most difficulty meeting resource adequacy requirements. The capacity addition expenditure made for each asset type is reported as the percentage of the mean cost of electricity with no additional expenditure. The black dotted line represents the resource adequacy requirement used in this study (99.9989% met demand).

Figure A2 shows the percentage of demand met for least-cost solar-wind-battery systems in operational years that resulted from capacity addition based on each planning year. For all asset types evaluated, the marginal return on asset expenditures allocated to maintaining resource adequacy in operating years decreased as the expenditure increased. A capacity addition expenditure allocated to wind generation of 140% of the total mean cost of electricity (Figure A2; top axis)

resulted in a minimum met demand (the lowest average percentage of demand met by any single system) in operational years of 99.9994%, above the resource adequacy requirement stipulated herein. An equal capacity expenditure in battery storage also brought the minimum met demand of the systems studied above the resource adequacy requirement, with 100% of demand met in operational years. In contrast, the same expenditure allocated to increased solar generation capacity resulted in a minimum demand met of 99.956%, which did not satisfy the minimum resource adequacy requirement. Even increasing the expenditure on solar generation capacity to over 560% of the total mean cost of electricity (Figure A2; top axis) did not result in systems that met the specified resource adequacy requirement, with a minimum met demand for all systems of 99.961%.

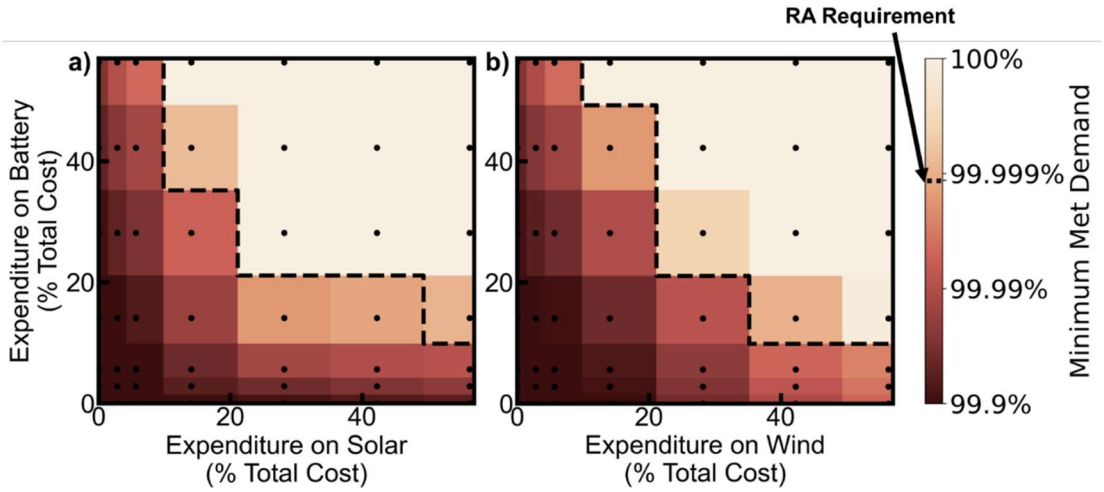

Figure A3. Impact of simultaneous expenditures in expanded generation and storage capacities on resource adequacy when electricity was supplied by wind and solar generation in conjunction with Li-ion battery storage. Simultaneous capacity addition expenditures were made for each of the least-cost systems obtained from the 42 planning years in (a) solar generation and battery storage capacity, and (b) wind generation and battery storage capacity. These systems were then operated over the full 42 years of weather data, and the demand met during operation is reported as a percentage of mean demand across the dataset. This figure displays the minimum

met demand (the lowest average percentage of demand met by any single system), so the data are displayed for the system that had the most difficulty meeting resource adequacy requirements. The capacity addition expenditure made for each asset type is shown as the percentage of the mean cost of electricity with no additional expenditure. The black dotted line represents the resource adequacy requirement used in this study (99.9989% of met demand). Data points are represented by black dots.

Figure A3 illustrates the effect of simultaneous capacity additions in battery storage and generation on resource adequacy. For battery storage in combination with either generation technology, a simultaneous expenditure on generation and storage was a more cost-effective approach to increasing resource adequacy during system operating years than an expenditure on generation or storage alone. For example, for all systems studied, a capacity addition expenditure equal to 56% of the total mean cost of electricity, split evenly between solar generation and battery storage, resulted in 100% of demand met during operational years (Figure A3a). This same expenditure in solely battery storage or solely solar generation only resulted in a minimum met demand of 99.97% and 99.72%, respectively. Consistently, the same expenditure (56% of total mean cost of electricity) split evenly between expansion of wind generation capacity and battery storage resulted in a minimum met demand of 99.9996%, above the resource adequacy requirement used in this analysis (Figure A3b). This same expenditure in solely wind generation only yielded a minimum met demand of 99.94%, which was larger than the percentage of demand met when the expenditure was solely devoted to solar generation.

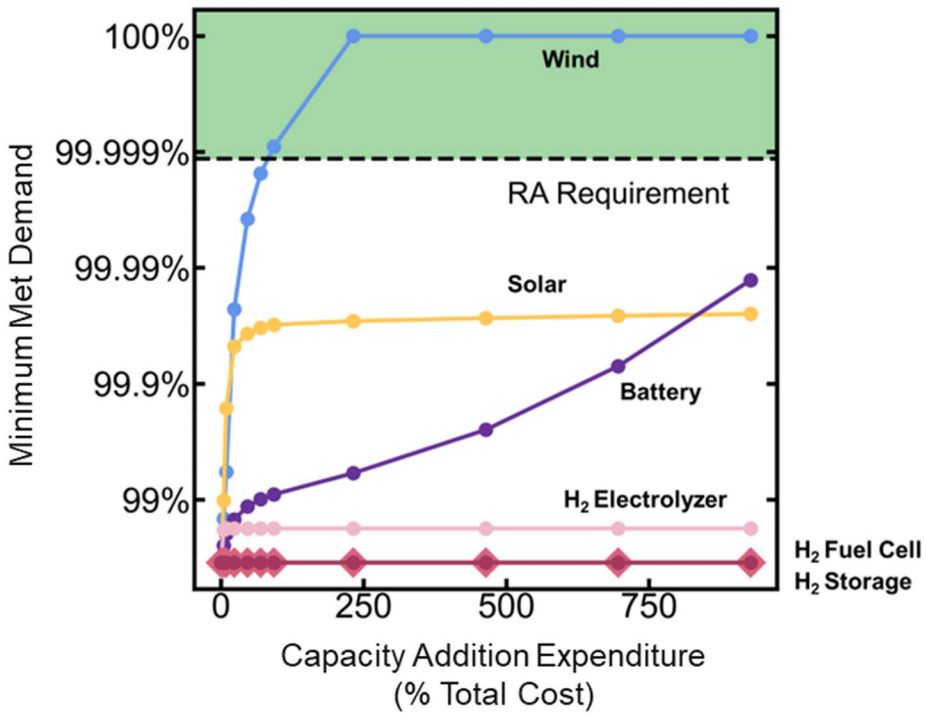

Figure A4. Impact of expenditures on capacity addition vs demand met when electricity was supplied by wind and/or solar generation in conjunction with Li-ion battery storage and hydrogen power-to-gas-to-power energy storage. Independent capacity addition expenditures were made in wind generation (blue), solar generation (yellow), battery storage (purple), PEM electrolyzers (light pink), salt cavern hydrogen energy storage (dark pink), or PEM fuel cell (maroon diamonds) for least-cost systems that met 100% of hourly averaged demand in each of the 42 planning years. These systems were then operated over the full 42 years of weather data, and the demand met during operation is reported as a percentage of mean demand. This figure displays the minimum met demand (the lowest average percentage of demand met by any single system), so the data are displayed for the system that had the most difficulty meeting resource adequacy requirements. The capacity addition expenditure made for each asset type is reported as the percentage of the mean cost of electricity with no additional expenditure. The black dotted line represents the resource adequacy requirement used in this study (99.9989% met demand).

Figure A4 shows the effects of capacity addition expenditures on resource adequacy of the solar-wind-battery-H_2 system. As observed for the solar-wind-battery system, the marginal improvement in resource adequacy decreased as the expenditure on capacity addition increased. A capacity addition expenditure

allocated to wind generation of 93% of the total mean cost of electricity resulted in a minimum met demand of 99.9992%, above the resource adequacy standard used in this analysis. The same expenditure in increased solar generation capacity however resulted in a minimum met demand of 99.96%. Moreover, increasing the expenditure in solar generation to 928% of the total mean cost of electricity resulted in a minimum met demand of 99.97%, still below the resource adequacy metric used herein, in a fashion analogous to the trend observed for expenditure on solar generation capacity in the solar-wind-battery system.

For solar-wind-battery-H_2 systems, capacity addition expenditures in storage technologies were less cost-effective approaches to increasing resource adequacy than capacity expenditures in wind generation, contrary to the behavior observed for solar-wind-battery systems. An expenditure in additional battery storage capacity of as large as 928% of the total mean cost of electricity resulted in a minimum met demand of 99.987%, below our resource adequacy metric. An expenditure allocated to increasing hydrogen electrolyzer capacity in an amount of 23% of the total mean cost of electricity increased the minimum met demand by 1.714%. Further expenditures in hydrogen electroylzer capacity had almost no impact on resource adequacy (<0.0000001%). Moreover, expenditures on either salt cavern hydrogen storage capacity or hydrogen fuel cell capacity had little impact on resource adequacy (the minimum met demand increased by <0.0000001% and 0.0015%, respectively with an expenditure of 928% of total mean cost of electricity).

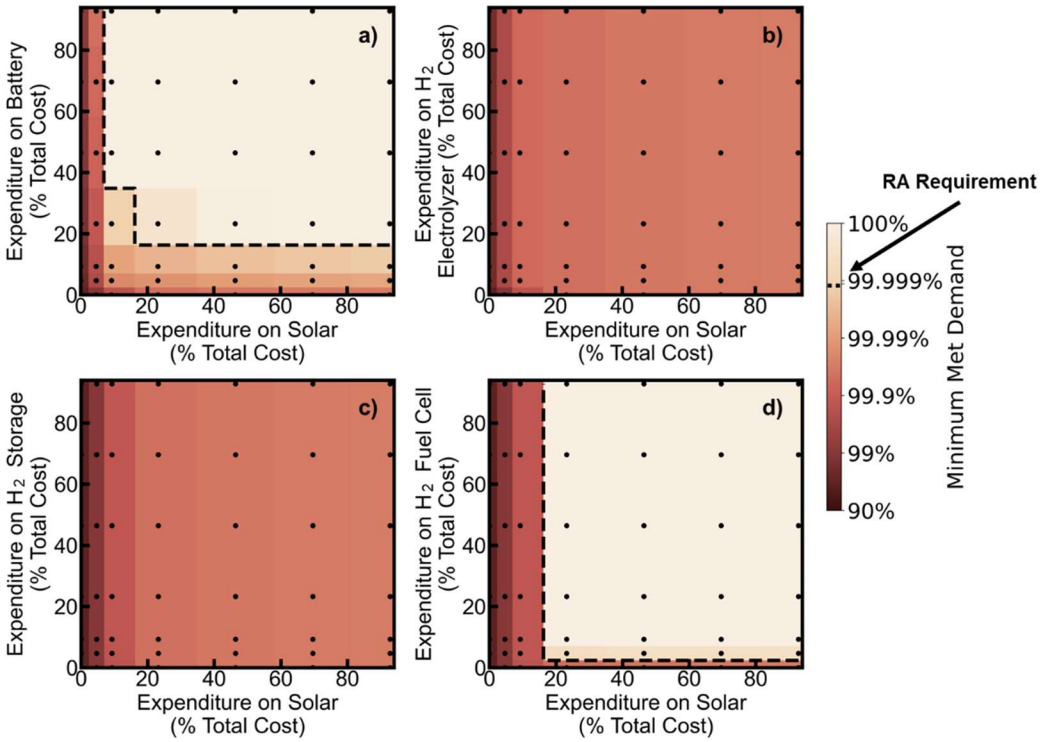

Figure A5. Impact of simultaneous expenditures in expanded generation and storage capacities on resource adequacy when electricity was supplied by wind and/or solar generation in conjunction with Li-ion battery storage and hydrogen power-to-gas-to-power energy storage. Simultaneous capacity addition expenditures for the least-cost systems that met 100% of hourly averaged demand in each of the 42 planning years were made in (a) solar generation and battery storage capacity, (b) solar generation and hydrogen electrolyzer capacity, (c) solar generation and hydrogen storage, and (d) solar generation and hydrogen fuel cell capacity. These systems were then operated over the full 42 years of weather data, and the demand met during operation is reported as a percentage of mean demand. This figure displays the minimum met demand (the lowest average percentage of demand met by any single system), so the data are displayed for the system that had the most difficulty meeting resource adequacy requirements. The capacity addition expenditure made for each asset type is reported as the percentage of the mean cost of electricity with no additional expenditure. The black dotted line represents the resource adequacy requirement used in this study (99.9989% met demand). Data points are represented by black dots. In contrast to expansions in battery storage or hydrogen fuel cell capacity, additional spending on hydrogen electrolyzers or hydrogen storage had minimal impact on the share of demand met, even when combined with increased solar or wind capacity.

Figure A5 shows the effect of simultaneous capacity addition expenditures allocated to increasing solar generation capacity in conjunction with increasing

battery or hydrogen storage capacities, while Figure A6 displays results for expenditure in wind generation in conjunction with storage technologies. The resulting increase in generation capacity enabled the system to meet, or exceed, the resource adequacy standard either by concurrent expenditures on increasing battery storage capacity (Figure A5a) or hydrogen fuel cell capacity (Figure A5d). Spending about 60% of the total mean cost of electricity on solar and battery capacity addition, split evenly between the two classes of assets, produced a system that met resource adequacy requirements during operation. However, allocation of this same expenditure solely to battery storage or solely to solar generation only resulted in systems with a minimum met demand of 98.85% and 99.96%, respectively, during operation. Expenditure of 23% of the total mean cost of electricity on solar generation and 5% of total mean cost of electricity on hydrogen fuel cell capacity yielded a system that met the resource adequacy metric with the lowest increase to total system cost of any combinations studied in this analysis. However, no expenditure allocated to either technology alone produced a system that met the resource adequacy metric during operation (Figure A4). In contrast to expansion of battery storage and hydrogen fuel cell capacity, expenditures allocated to either hydrogen electrolyzer capacity or hydrogen storage capacity had a relatively minor effect on the percentage of demand met during system operation, even in conjunction with expenditures allocated to expansion of solar or wind generation capacity (Figure A5b and A5c, Figure A6a and Figure A6b).

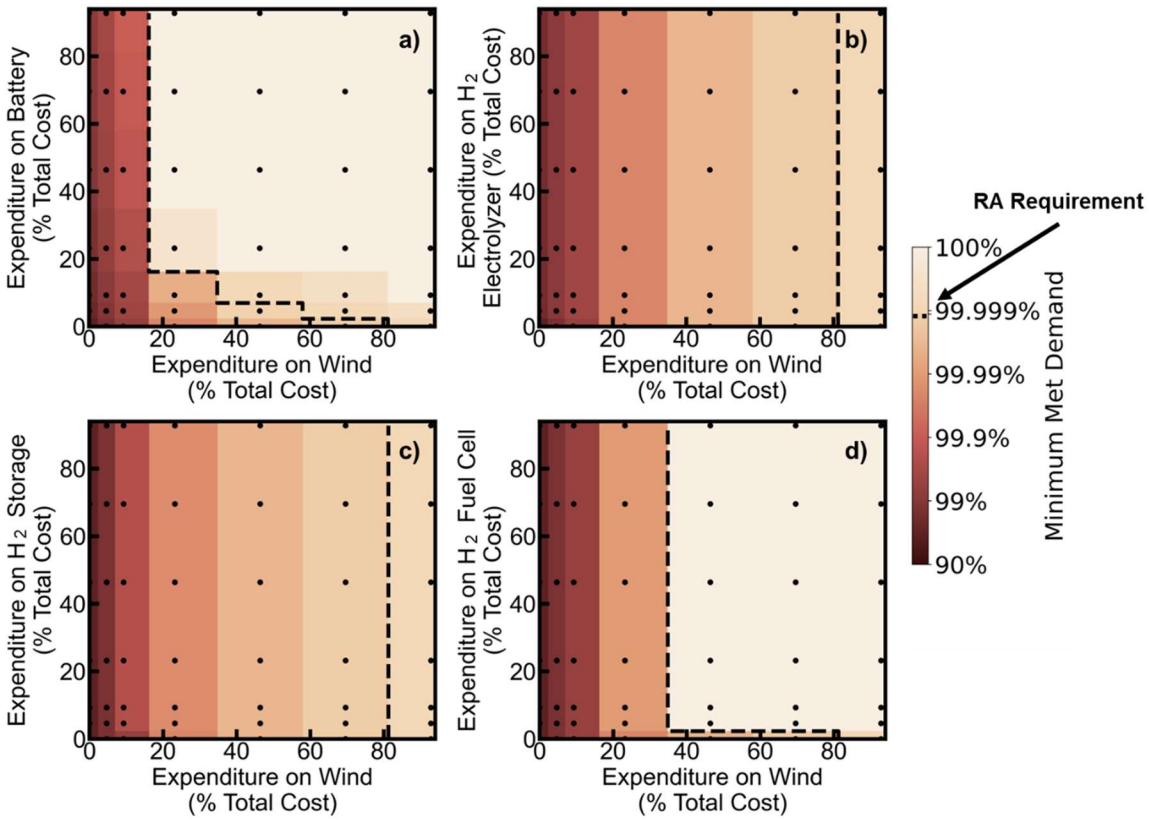

Figure A6. Impact of simultaneous expenditures in expanded generation and storage capacities on resource adequacy when electricity was supplied by wind and/or solar generation in conjunction with Li-ion battery storage and hydrogen power-to-gas-to-power energy storage. Simultaneous capacity addition expenditures were made in (a) wind generation and battery storage capacity, (b) wind generation and hydrogen electrolyzer capacity, (c) wind generation and hydrogen storage, and (d) wind generation and hydrogen fuel cell capacity for the least-cost system obtained from each of the 42 planning years. for least-cost systems that met 100% of hourly averaged demand in each of the 42 planning years. These systems were then operated over the full 42 years of weather data, and the demand met during operation is reported as a percentage of mean demand. This figure displays the minimum met demand (the lowest average percentage of demand met by any single system), so the data are displayed for the system that had the most difficulty meeting resource adequacy requirements. The capacity addition expenditure made for each asset type is reported as the percentage of the mean cost of electricity with no additional expenditure. The black dotted line represents the resource adequacy requirement used in this study (99.998% met demand). Data points are represented by black dots.

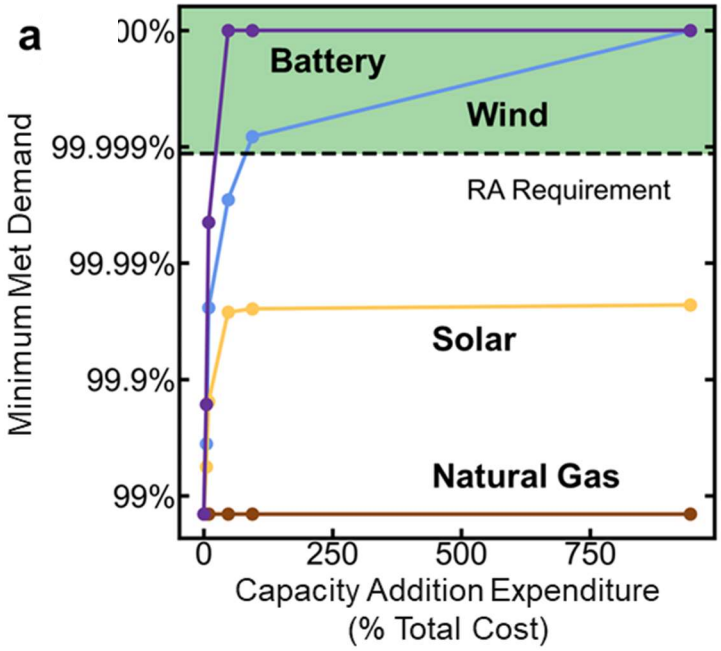

Figure A7. Impact of capacity addition expenditures on resource adequacy when electricity was supplied by wind and/or solar generation in conjunction with Li-ion battery storage and natural gas combustion was available as firm dispatchable generation but was constrained to provide no more than 5% of mean demand. An expenditure was made to increase wind generation capacity (blue), solar generation capacity (yellow), battery storage capacity (purple), or natural gas combined-cycle generation capacity (brown) for least-cost systems that met 100% of hourly averaged demand in each of the 42 planning years, though natural gas dispatch was still constrained to no more than 5% mean demand. These systems were then operated over the full 42 years of weather data, and the demand met during operation is reported as a percentage of mean demand. This figure displays the minimum met demand (the lowest average percentage of demand met by any single system), so the data are displayed for the system that had the most difficulty meeting resource adequacy requirements .The black dotted line represents the resource adequacy requirement used in this study (99.9989% met demand).

Figure A7 shows the effects of capacity addition expenditures in the solar-wind-battery-5% natural gas dispatch system. A capacity addition expenditure in battery storage of 47% of the mean system cost of the least-cost systems obtained in planning years resulted in a minimum met demand of 100%. Spending 94% of the original system cost on additional capacity of wind resulted in a minimum met

demand of 99.9993%, above the resource adequacy standard used in this analysis. No expenditure in increased solar generation capacity resulted in a minimum met demand above the resource adequacy standard, increasing that expenditure in solar generation to 944% of the mean system cost only resulted in a minimum met demand of 99.97%, still below resource adequacy, and analogous to the trend observed for expenditure on solar capacity in the solar-wind-battery system. Natural gas dispatch was constrained to 5% of mean demand, therefore increases in natural gas capacity had no impact on resource adequacy.

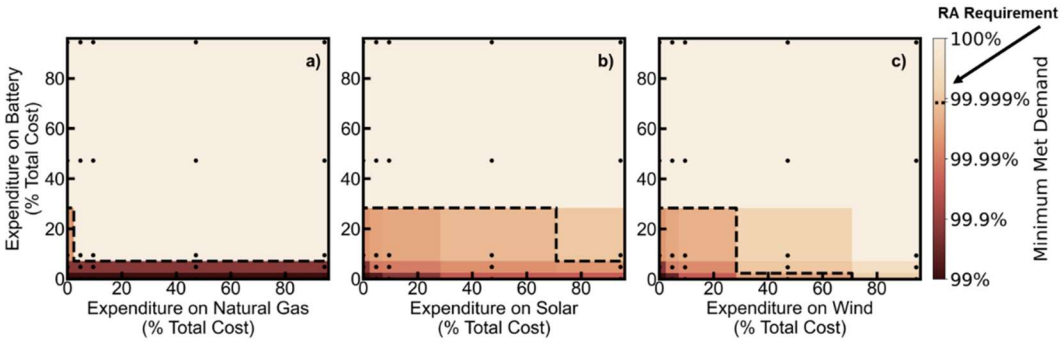

Figure A8. Impact of simultaneous expenditures in expanded generation and storage capacities on resource adequacy when electricity was supplied by wind and/or solar generation in conjunction with Li-ion battery storage and natural gas combustion was available as firm dispatchable generation but was constrained to provide no more than 5% of mean demand. Simultaneous capacity addition expenditures were made in (a) natural gas combined-cycle generation and battery storage capacity, (b) solar generation and battery storage capacity, and (c) wind generation and battery storage capacity for the least-cost system obtained from each of the 42 planning years for least-cost systems that met 100% of hourly averaged demand in each of the 42 planning years, though natural gas dispatch was still constrained to no more than 5% mean demand. These systems were then operated over the full 42 years of weather data, and the demand met during operation is reported as a percentage of mean demand. This figure displays the minimum met demand (the lowest average percentage of demand met by any single system), so the data are displayed for the system that had the most difficulty meeting resource adequacy requirements. The capacity addition expenditure made for each asset type is reported as the percentage of the mean cost of electricity with no additional expenditure. The black dotted line represents the resource adequacy requirement used in this study (99.998% met demand). Data points are represented by black dots.

Figure A8 shows the effect of concurrent capacity addition expenditures on battery storage with expenditures on natural gas, wind, or solar generation. A capacity addition expenditure split evenly between solar and battery storage that was equal to 94% of the mean system cost of the least-cost systems obtained in planning years resulted in 100% met demand (Figure A8b). This same expenditure in solely solar generation only yields a minimum met demand of 99.97%. But in contrast to the other system architecture studied, an expenditure of 94% solely in battery storage is also able to meet 100% of demand. Again, with a simultaneous expenditure on wind and solar of 94% of total cost, split evenly between the technologies, yields a resource adequate system. That same expenditure solely on wind or solely on battery also yields a resource adequate system. When 5% of dispatch can be met with a firm dispatchable technology, like natural gas, a simultaneous expenditure on generation and storage technology was not more cost effective to increase resource adequacy than sole expenditure on generation or storage.

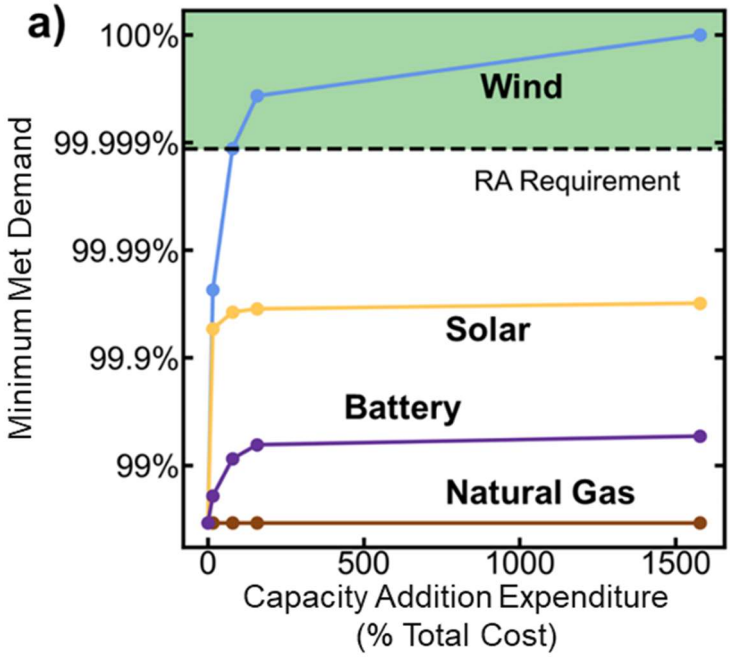

Figure A9. Impact of capacity addition expenditures on resource adequacy when electricity was supplied by wind and/or solar generation in conjunction with Li-ion battery storage and natural gas combustion was available as firm dispatchable generation but was constrained to provide no more than 30% of mean demand. An expenditure was made to increase wind generation capacity (blue), solar generation capacity (yellow), battery storage capacity (purple), or natural gas combined-cycle generation capacity (brown) for least-cost systems that met 100% of hourly averaged demand in each of the 42 planning years, though natural gas dispatch was still constrained to no more than 30% mean demand. These systems were then operated over the full 42 years of weather data, and the demand met during operation is reported as a percentage of mean demand. This figure displays the minimum met demand (the lowest average percentage of demand met by any single system), so the data are displayed for the system that had the most difficulty meeting resource adequacy requirements. The capacity addition expenditure made for each asset type is reported as the percentage of the mean cost of electricity with no additional expenditure. The black dotted line represents the resource adequacy requirement used in this study (99.9989% met demand).

Figure A9 shows the effects of capacity addition expenditures in the solar-wind-battery-30% natural gas dispatch system. A capacity addition expenditure in wind of 80% of the mean system cost of the least-cost systems obtained in planning years resulted in a minimum met demand of 99.99% above the resource adequacy

standard used in this analysis. No expenditure in either solar or battery storage resulted in minimum met demand above the resource adequacy standard, even at 1000% of mean system cost. This matches the trend for solar capacity expenditure observed in the solar-wind-battery-5% natural gas system, but not the trend observed for battery storage, as in this system there is too little otherwise-curtailed generation to make battery storage useful. With the ability to supply 30% of mean demand with firm generation, i.e. natural gas combustion, the system does not overbuild wind or solar. Natural gas dispatch was constrained to 30% of mean demand, therefore increases in natural gas capacity had little impact on resource adequacy.

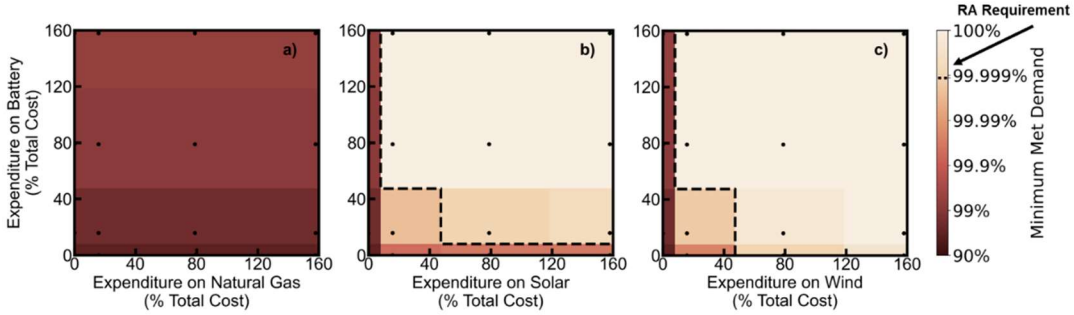

Figure A10. Impact of simultaneous expenditures in expanded generation and storage capacities on resource adequacy when electricity was supplied by wind and/or solar generation in conjunction with Li-ion battery storage and natural gas combustion was available as firm dispatchable generation but was constrained to provide no more than 30% of mean demand. Simultaneous capacity addition expenditures were made in (a) natural gas combined-cycle generation and battery storage capacity, (b) solar generation and battery storage capacity, and (c) wind generation and battery storage capacity for the least-cost system obtained from each of the 42 planning years for least-cost systems that met 100% of hourly averaged demand in each of the 42 planning years, though natural gas dispatch was still constrained to no more than 30% mean demand. These systems were then operated over the full 42 years of weather data, and the demand met during operation is reported as a percentage of mean demand. This figure displays the minimum met demand (the lowest average percentage of demand met by any single system), so the data are displayed for the system that had the most difficulty meeting resource adequacy requirements. The capacity addition expenditure made for each asset type is reported as the percentage of the mean cost of electricity with no additional

expenditure. The black dotted line represents the resource adequacy requirement used in this study (99.998% met demand). Data points are represented by black dots.

Figure A10 shows the effect of concurrent capacity addition expenditures on battery storage with expenditures on natural gas, wind, or solar generation. A capacity addition expenditure split evenly between solar or wind and battery storage that was equal to 96% of the mean system cost (split unevenly with 16% invested in either generation or storage) of the least-cost systems obtained in planning years resulted in all systems being resource adequate (Figure A8b and A8c). Expenditure on battery storage becomes significantly more valuable when there is concurrent expenditure on wind or solar generation, highlighting the lack of excess generation for battery usage in this system. However, an expenditure on wind of 80% of mean system cost on wind also yields a resource adequate system, which follows the trend observed for the system allowing 5% natural gas dispatch, that a simultaneous expenditure on generation and storage technology was not more cost effective to increase resource adequacy than sole expenditure on generation or storage.

The spatially and temporally coarse-grained macro-energy system modeling allows transparent evaluation of issues associated with obtaining long-term resource adequacy from systems that rely solely on variable renewable generation in conjunction with energy storage, but that do not have available substantial firm dispatchable generation. In such scenarios, the historical practice of establishing reserve margins based on limited demand and supply planning data is not adequate to definitively ensure future resource adequacy, because the annual generation is determined by the geophysical variability of the wind and/or solar resources over the

load-balancing region of interest. In an illustrative limiting case evaluated herein, with CONUS as the load-balancing region and lossless transmission from generation to load throughout CONUS, the variability in generation occurs due to the predictable diurnal and seasonal variability of the insolation as well as the unpredictable, large amplitude, weekly, monthly, seasonal, and interannual variability of wind resources. Moreover, the variability in wind resources on these timescales does not follow a Gaussian distribution but instead exhibits characteristics of red noise, with variability increasing as the period over which the resource is evaluated increases. Here, we use 'red' in the general sense, referring to the tendency of lower-frequency components to dominate the variability. Hence, statutorily mandated formulas for resource adequacy, such as the presently in-force NERC standard that electricity systems be planned so that hourly averaged demand is not met in full for at most 1 hour in a decade, will need to take into consideration planning for resource adequacy against events that represent a “once in a century flood” or a “once in a century wind drought”, in light of past geophysical resource variability as well as potentially ill-understood future resource variability due to climate change and related impacts.

Currently and in the foreseeable future, the cost of energy storage per kWh remains substantially higher than the hourly cost of one kW of generation capacity. Consequently, stylized wind/solar generation least-cost systems evaluated over a variety of regions globally consist of substantial amounts of wind generation, due to the expense and technological limitations of batteries and the inability of solar generation to provide power during darkness. Hence, obtaining high resource adequacy in such stylized electricity systems requires extensive (and thus costly)

curtailment of wind generation at all but the most stressing time periods of resource availability relative to electricity demand. When short-duration and long-duration storage is available, in least-cost stylized systems, storage is deployed until the marginal cost increase due to deploying storage exceeds the marginal cost decrease associated with a reduction in the wind generation assets required to maintain resource adequacy (Figure A6). However, least-cost systems planned based on one year of weather variability (primarily wind variability in most cases) cost substantially less than least-cost systems that meet demand in full over many years or decades, due to the need to anticipate resource variability and thus incur extensive curtailment in much of the operational time of the system.

A retrospective analysis of the stylized model systems evaluated herein indicates that some types of capacity addition expenditures would have been especially cost effective when expanding a wind-solar-battery electricity system from the least-cost asset mix obtained from a single planning year to provide resource adequacy over extended periods (i.e. decades) of operational years. Least-cost systems met demand during darkness by a combination of wind generation and storage assets, with storage helping to smooth the variability of extensive wind resources. No amount of additional solar generation reduced the need for these wind generation or storage assets, nor provided the electricity needed to meet increased demand during darkness in system operational years. In contrast, expansion of wind generation capacity from the values obtained in the planning year would have provided increased generation that could have met demand in full in operational years, albeit at the expense of substantial curtailment and thus substantial increases

in electricity system costs. Increasing storage capacity alone was not a cost-effective approach for meeting residual demand challenges on the order of weeks or seasons. At current asset costs, the most cost-effective capacity addition approach is to strategically allocate expenditures to the concurrent expansion of generation and storage assets, regardless of whether the generation comes from solar or wind resources.

In the stylized systems that additionally had long-duration storage available, least-cost systems in the planning year had substantially less generation assets, and thus lower cost, than systems without long-duration storage. Furthermore, expenditures associated with additional wind generation relative to systems formed based only on the planning year met demand in operational years both by producing more available generation and by resulting in more stored energy. Expansion of solar generation did not produce more electricity during darkness and exhausted the limited capacity of the storage reservoir due to the larger daily variability of the solar resource relative to the wind resource. Similarly, expansion of hydrogen energy storage alone minimally increased resource availability in operational years, due to the inability of the limited amount of generation in least-cost systems obtained in the planning year to provide the increased residual electricity needed to compensate for wind and/or solar droughts during some of the system operational years. In stylized systems that had both short and long-duration storage available, resource adequacy relative to the least-cost systems for planning years was therefore most cost-effectively produced in operational years by expenditures on both generation and storage assets. Increases in generation along with increases in battery capacity or

hydrogen energy storage discharge capacity were the most cost-effective approaches to meeting demand in full in system operational years. This behavior reflects the geophysical variability of the resources being exploited, because the limiting factor to meet demand is the high discharge power needed during resource lulls in operational years relative to the ability to more slowly charge the reservoirs with otherwise curtailed electricity in other time periods.

Current electricity systems manage uncertainty, in part, through the use of planning reserve margins that specify capacity held above forecasted peak demand to account for contingencies such as forecast errors, forced outages, transmission constraints, and inter-annual weather variation. These deterministic margins implicitly serve as a coarse proxy for probabilistic adequacy but are typically calibrated using limited historical data and short simulation horizons. The finding that a coordinated expansion of generation and storage most effectively enhances resource adequacy provides a pathway for reinterpreting reserve margins not as fixed percentage targets, but as dynamic reliability requirements that can be met by portfolios combining additional generation, short- and long-duration storage, and potentially limited firm capacity. In this way, the analysis provides insight into how future planning margins could evolve to reflect the nature of renewable variability.

The analysis has limitations that should be considered when interpreting the results. The wind and solar generation profiles used in this study were selected from the top 25% of grid cells by resource, and were aggregated over the contiguous United States.[24] Additionally, a single node was used to represent the contiguous U.S. grid, resulting in unconstrained power and gas transmission from generation to load

sites. Representing spatial heterogeneity and transmission limitations would only increase the amount of backup storage and/or additional generation needed to provide system reliability. Modeling smaller geographic areas, such as the Independent System Operators (ISOs), would increase the variability of wind and/or solar generation over these regions relative to over CONUS and is moreover expected to lead to an increase in the frequency, length, and magnitude of resource droughts. Including more geographic detail in the analysis would therefore further strengthen the conclusion that a strategic combination of generation and storage is most effective for achieving resource adequacy. This simplifying assumption of a single-node system explicitly isolates the effect of generation and storage capacity from transmission constraints, but previous regionalized analyses of Oahu and California/Western Electricity Coordinating Council systems, as well as multi-region storage studies, have shown that constraining the load-balancing region to smaller geographical areas generally amplifies the renewable resource variability and the severity of resource droughts, and therefore tends to increase the need for backup storage and/or dispatchable generation capacity.[25,36,58] Consequently, the finding that coordinated investments in both generation and storage improve reliability is expected to remain robust even under more geographically constrained and transmission-constrained conditions. The generation capacity added through marginal expenditures will not generally be well-correlated spatially or temporally with demand, necessitating concurrent deployment of additional storage assets at a magnitude that is likely to be greater than that calculated here.

Similarly, if future resource variability increases due to climate change, the lack of full correlation between generation and demand would also imply that a strategic combination of investments in generation and storage would provide the most-cost effective approach to meet demand over long periods of resource variability. Although this analysis used retrospective demand data, the main findings are expected to be robust under a range of plausible future load shapes and weather conditions. Changes in the timing or amplitude of seasonal demand peaks (for example, stronger winter or summer peaks) could affect the magnitude of the expenditures and capacities needed to deal with resource variability. Increases in demand variability would increase the motivation for coordinated investments in both generation and storage. This analysis also represents the two extremes of the storage-duration spectrum by using lithium-ion batteries and electrolytic hydrogen to capture short- and long-duration balancing behavior. There is a spectrum of storage technologies that could potentially firm up wind and solar-reliant electricity systems.[59] However, once long-duration storage is available in single-node systems, both short- and long-term reliability can be satisfied primarily by the long-duration storage assets, when the energy and power capacities of other technologies are optimized endogenously, leaving little role for intermediate-duration storage or additional flexibility in power-to-energy sizing for technologies with separable components.[36] Additionally, this analysis focuses on resource adequacy rather than operational reliability. Although resource adequacy quantifies the probabilistic ability of the system to meet demand, operational reliability concerns short-timescale stability phenomena such as inertia, frequency response, and dynamic stability. These

aspects, though also affected by high penetrations of renewable resources, are not directly influenced by inter-annual weather variability and are therefore beyond the scope of this study.

In our analysis, asset costs were assumed to be fixed, with the system assumed to be constructed overnight. Regardless of the ratio between solar and wind generation costs, obtaining resource adequacy solely through additional expenditures on solar generation is not feasible due to the diurnal insolation cycle. In contrast, although battery or other storage technologies are currently expensive relative to wind and solar generation, if storage were to become much cheaper than generation, an unconstrained ability to arbitrarily time-shift generated power to meet demand in the limit of free or nearly free storage would favor deployment of the least-expensive generation asset on a levelized electricity cost basis regardless of the variability of the resource. However, such a situation would still require a strategic expenditure in both generation and storage to cost-effectively meet demand over extended time periods. The main finding—that concurrent strategic expenditure in both generation and storage is more cost effective than expenditures allocated to either asset class alone—consequently is expected to be robust over a wide range of cost assumptions and geographic constraints.

Allowing a small percentage of firm dispatchable energy sources, such as natural gas, to meet 5% of mean demand (Figure A7-A8) alleviated some of the issues associated with obtaining resource adequacy. In these scenarios, the 5% and 30% limits were applied as constraints on the mean annual energy supplied by natural gas, allowing gas to operate flexibly within that annual bound. Systems that allowed

for 5% of mean demand supplied by gas generation were not able to meet all demand during all the >40 weather years but required lower marginal expenditures on battery storage or wind generation to meet demand in full than systems that did not allow natural gas dispatch. Allowing natural gas to meet 30% of mean demand (Figure A9-A10) substantially decreased system costs, and when these systems were operated on all the historical weather years, the minimum met demand was higher than for all the other cases studied, making it the least robust system architecture over decades of variability. The resulting systems relied heavily on natural gas to smooth the variability of wind and solar generation, but when gas generation was limited to 30% of the mean demand, gas dispatch could not fully compensate for the variability in renewable generation over the full >40 year time period.

Additional marginal expenditures on wind generation capacity allowed 100% of demand to be met over the entire 42-year period, in contrast to marginal expenditures on batteries or hydrogen energy storage technologies, because the amount of energy that could be stored was limited by the amount of otherwise curtailed generation in conjunction with limitations on solar generation associated with the diurnal variability of insolation. Moreover, for both systems in which natural gas dispatch was limited, either to 5% or 30% of the mean demand, the expenditure on wind generation alone that was required to meet demand in full was less than the expenditures that were required to meet demand through a concurrent expansion of solar generation and battery storage. Hence, the availability of a dispatchable source of electricity eliminated the benefit of strategic simultaneous expenditures on generation and storage relative to expenditures on generation (and storage, for the

case where natural gas dispatch was limited to 5%) alone, because the dispatchable resource smoothed much of the variability of wind and solar generation, obviating the need for additional battery storage to meet demand in full most cost-effectively. Other firm, low-carbon resources such as nuclear power, which may play an important role in future low-carbon energy systems, could technically fulfill this role. Because nuclear power is dominated by fixed capital costs and minimal variable costs, at current costs, use of nuclear power at low capacity factors to firm wind and/or solar generation would be more costly than gas generation, which is better suited for operation at moderate capacity factors due to a moderate capital cost and moderate variable fuel costs.[60] Hydroelectricity was likewise excluded because its inclusion has been shown to have limited effects on total system cost or technology mix in least-cost renewable electricity systems.[25] Moreover, the seasonality of hydroelectricity can slightly increase the required installed capacity of storage technologies in reliable, least-cost systems, so the inclusion of hydroelectricity is likely to strengthen the need for combined investment in generation and storage.

A.4 Conclusions

This work evaluated cost-effective strategies for improving long-term resource adequacy in wind- and solar-based electricity systems that are planned using limited weather data but must operate over decades of real-world weather variability. Using a stylized macro-scale model across CONUS, this study showed that least-cost systems designed using a single planning year did not reliably satisfy demand when exposed to multi-decadal resource variability. The analysis further demonstrated that, in the wind–solar systems considered here, the most effective way to improve adequacy was not generally to invest in a single asset class, but instead to make coordinated additions to wind and solar generation and storage capacity. In systems with only battery storage, simultaneous expenditures on generation and storage were substantially more cost-effective than expenditures on either alone. In systems with both short- and long-duration storage, the same general conclusion held, although the most effective additions depended on which component constrained performance. Across all cases without substantial firm dispatchable generation, additional solar generation alone was insufficient to restore adequacy, underscoring the importance of considering not only total annual energy production but also the temporal availability of that energy.

The novelty of this work lies in its explicit examination of how incremental, post-planning capacity additions can be used to recover resource adequacy in systems that were designed using limited weather information. Rather than assuming perfect-foresight planning over many decades of resource data, this study reflects the practical reality that future weather is unknown and that capacity expansion decisions

are often made using relatively short historical records. For deeply decarbonized systems, the results thus provide an adaptive analogue to traditional reserve-margin planning. The findings also highlight the limitations of applying legacy adequacy standards, such as the NERC one-hour-in-a-decade framework, to electricity systems whose performance is strongly shaped by low-frequency weather events and interannual renewable resource variability.

A.5. Bibliography

(1)Autumn, K.; Liang, Y. A.; Hsieh, S. T.; Zesch, W.; Chan, W. P.; Kenny, T. W.; Fearing, R.; Full, R. J. Adhesive Force of a Single Gecko Foot-Hair. *Nature* **2000**, *405* (6787), 681–685. https://doi.org/10.1038/35015073.
(2)Liu, Y.; Wang, H.; Li, J.; Li, P.; Li, S. Gecko-Inspired Controllable Adhesive: Structure, Fabrication, and Application. *Biomimetics* **2024**, *9* (3), 149. https://doi.org/10.3390/biomimetics9030149.
(3)Watson, G. S.; Green, D. W.; Schwarzkopf, L.; Li, X.; Cribb, B. W.; Myhra, S.; Watson, J. A. A Gecko Skin Micro/Nano Structure – A Low Adhesion, Superhydrophobic, Anti-Wetting, Self-Cleaning, Biocompatible, Antibacterial Surface. *Acta Biomater.* **2015**, *21*, 109–122. https://doi.org/10.1016/j.actbio.2015.03.007.
(4)*Gecko-adhesive for gentle robotic grasping of irregular objects | Explore Technologies*. https://techfinder.stanford.edu/technology/gecko-adhesive-gentle-robotic-grasping-irregular-objects (accessed 2026-04-14).
(5)Ball, P. Engineering Shark Skin and Other Solutions. *Nature* **1999**, *400* (6744), 507–509. https://doi.org/10.1038/22883.
(6)Bixler, G. D.; Bhushan, B. Fluid Drag Reduction with Shark-Skin Riblet Inspired Microstructured Surfaces. *Adv. Funct. Mater.* **2013**, *23* (36), 4507–4528. https://doi.org/10.1002/adfm.201203683.
(7)Kelleher, S. M.; Habimana, O.; Lawler, J.; O' Reilly, B.; Daniels, S.; Casey, E.; Cowley, A. Cicada Wing Surface Topography: An Investigation into the Bactericidal Properties of Nanostructural Features. *ACS Appl. Mater. Interfaces* **2016**, *8* (24), 14966–14974. https://doi.org/10.1021/acsami.5b08309.
(8)Diu, T.; Faruqui, N.; Sjöström, T.; Lamarre, B.; Jenkinson, H. F.; Su, B.; Ryadnov, M. G. Cicada-Inspired Cell-Instructive Nanopatterned Arrays. *Sci. Rep.* **2014**, *4* (1), 7122. https://doi.org/10.1038/srep07122.
(9)Bhadra, C. M.; Khanh Truong, V.; Pham, V. T. H.; Al Kobaisi, M.; Seniutinas, G.; Wang, J. Y.; Juodkazis, S.; Crawford, R. J.; Ivanova, E. P. Antibacterial Titanium Nano-Patterned Arrays Inspired by Dragonfly Wings. *Sci. Rep.* **2015**, *5* (1), 16817. https://doi.org/10.1038/srep16817.
(10)Khatoon, Z.; McTiernan, C. D.; Suuronen, E. J.; Mah, T.-F.; Alarcon, E. I. Bacterial Biofilm Formation on Implantable Devices and Approaches to Its Treatment and Prevention. *Heliyon* **2018**, *4* (12), e01067. https://doi.org/10.1016/j.heliyon.2018.e01067.
(11)Ahmed, R.; Ji, X.; Atta, R. M. H.; Rifat, A. A.; Butt, H. Morpho Butterfly-Inspired Optical Diffraction, Diffusion, and Bio-Chemical Sensing. *RSC Adv.* **2018**, *8* (48), 27111–27118. https://doi.org/10.1039/C8RA04382E.
(12)Butt, H.; Yetisen, A. K.; Mistry, D.; Khan, S. A.; Hassan, M. U.; Yun, S. H. *Morpho* Butterfly-Inspired Nanostructures. *Adv. Opt. Mater.* **2016**, *4* (4), 497–504. https://doi.org/10.1002/adom.201500658.
(13)D., H.; Wai, S. Focused Ion Beam Lithography. In *Recent Advances in Nanofabrication Techniques and Applications*; Cui, B., Ed.; InTech, 2011. https://doi.org/10.5772/22075.

(14)Balslev, H. Tomlinson, P. B. 1990. The Structural Biology of Palms. *Nord. J. Bot.* **1991**, *11* (2), 152–152. https://doi.org/10.1111/j.1756-1051.1991.tb01815.x.
(15)Christie, J. M.; Murphy, A. S. Shoot Phototropism in Higher Plants: New Light through Old Concepts. *Am. J. Bot.* **2013**, *100* (1), 35–46. https://doi.org/10.3732/ajb.1200340.
(16)Iwase, A.; Sakai, K.; Suzuki, A.; van Woesik, R. Phototropic Adjustment of the Foliaceous Coral Echinopora Lamellosa in Palau. *Estuar. Coast. Shelf Sci.* **2008**, *77* (4), 672–678. https://doi.org/10.1016/j.ecss.2007.10.022.
(17)Kaniewska, P.; Campbell, P. R.; Fine, M.; Hoegh-Guldberg, O. Phototropic Growth in a Reef Flat Acroporid Branching Coral Species. *J. Exp. Biol.* **2009**, *212* (5), 662–667. https://doi.org/10.1242/jeb.022624.
(18)Meier, M. C.; Cheng, W.-H.; Atwater, H. A.; Lewis, N. S.; Carim, A. I. Inorganic Phototropism in Electrodeposition of Se–Te. *J. Am. Chem. Soc.* **2019**, *141* (47), 18658–18661. https://doi.org/10.1021/jacs.9b10579.
(19)Sadtler, B.; Burgos, S. P.; Batara, N. A.; Beardslee, J. A.; Atwater, H. A.; Lewis, N. S. Phototropic Growth Control of Nanoscale Pattern Formation in Photoelectrodeposited Se–Te Films. *Proc. Natl. Acad. Sci.* **2013**, *110* (49), 19707–19712. https://doi.org/10.1073/pnas.1315539110.
(20)Carim, A. I.; Batara, N. A.; Premkumar, A.; May, R.; Atwater, H. A.; Lewis, N. S. Morphological Expression of the Coherence and Relative Phase of Optical Inputs to the Photoelectrodeposition of Nanopatterned Se–Te Films. *Nano Lett.* **2016**, *16* (5), 2963–2968. https://doi.org/10.1021/acs.nanolett.5b04999.
(21)Carim, A. I.; Batara, N. A.; Premkumar, A.; Atwater, H. A.; Lewis, N. S. Polarization Control of Morphological Pattern Orientation During Light-Mediated Synthesis of Nanostructured Se–Te Films. *ACS Nano* **2016**, *10* (1), 102–111. https://doi.org/10.1021/acsnano.5b05119.
(22)Hamann, K. R.; Meier, M. C.; Lewis, N. S.; Carim, A. I. Plastic Morphological Response to Spectral Shifts during Inorganic Phototropic Growth. *JACS Au* **2022**, *2* (4), 865–874. https://doi.org/10.1021/jacsau.1c00588.
(23)*Table of 100% Clean Energy States*. Clean Energy States Alliance. https://www.cesa.org/projects/100-clean-energy-collaborative/guide/table-of-100-clean-energy-states/ (accessed 2025-02-18).
(24)Shaner, M. R.; Davis, S. J.; Lewis, N. S.; Caldeira, K. Geophysical Constraints on the Reliability of Solar and Wind Power in the United States. *Energy Environ. Sci.* **2018**, *11* (4), 914–925. https://doi.org/10.1039/C7EE03029K.
(25)Rinaldi, K. Z.; Dowling, J. A.; Ruggles, T. H.; Caldeira, K.; Lewis, N. S. Wind and Solar Resource Droughts in California Highlight the Benefits of Long-Term Storage and Integration with the Western Interconnect. *Environ. Sci. Technol.* **2021**, *55* (9), 6214–6226. https://doi.org/10.1021/acs.est.0c07848.
(26)Dowling, J. A.; Rinaldi, K. Z.; Ruggles, T. H.; Davis, S. J.; Yuan, M.; Tong, F.; Lewis, N. S.; Caldeira, K. Role of Long-Duration Energy Storage in Variable Renewable Electricity Systems. *Joule* **2020**, *4* (9), 1907–1928. https://doi.org/10.1016/j.joule.2020.07.007.

(27)Collins, S.; Deane, P.; Ó Gallachóir, B.; Pfenninger, S.; Staffell, I. Impacts of Inter-Annual Wind and Solar Variations on the European Power System. *Joule* **2018**, *2* (10), 2076–2090. https://doi.org/10.1016/j.joule.2018.06.020.
(28)Jenkins, J. D.; Luke, M.; Thernstrom, S. Getting to Zero Carbon Emissions in the Electric Power Sector. *Joule* **2018**, *2* (12), 2498–2510. https://doi.org/10.1016/j.joule.2018.11.013.
(29)Ruhnau, O.; Qvist, S. Storage Requirements in a 100% Renewable Electricity System: Extreme Events and Inter-Annual Variability. *Environ. Res. Lett.* **2022**, *17* (4), 044018. https://doi.org/10.1088/1748-9326/ac4dc8.
(30)Hilbers, A. P.; Brayshaw, D. J.; Gandy, A. Importance Subsampling: Improving Power System Planning under Climate-Based Uncertainty. *Appl. Energy* **2019**, *251*, 113114. https://doi.org/10.1016/j.apenergy.2019.04.110.
(31)Ruggles, T. H.; Virgüez, E.; Reich, N.; Dowling, J.; Bloomfield, H.; Antonini, E. G. A.; Davis, S. J.; Lewis, N. S.; Caldeira, K. Planning Reliable Wind- and Solar-Based Electricity Systems. *Adv. Appl. Energy* **2024**, *15*, 100185. https://doi.org/10.1016/j.adapen.2024.100185.
(32)Kennedy, K. M.; Ruggles, T. H.; Rinaldi, K.; Dowling, J. A.; Duan, L.; Caldeira, K.; Lewis, N. S. The Role of Concentrated Solar Power with Thermal Energy Storage in Least-Cost Highly Reliable Electricity Systems Fully Powered by Variable Renewable Energy. *Adv. Appl. Energy* **2022**, *6*, 100091. https://doi.org/10.1016/j.adapen.2022.100091.
(33)Ruggles, T. H.; Caldeira, K. Wind and Solar Generation May Reduce the Inter-Annual Variability of Peak Residual Load in Certain Electricity Systems. *Appl. Energy* **2022**, *305*, 117773. https://doi.org/10.1016/j.apenergy.2021.117773.
(34)Duan, L.; Petroski, R.; Wood, L.; Caldeira, K. Stylized Least-Cost Analysis of Flexible Nuclear Power in Deeply Decarbonized Electricity Systems Considering Wind and Solar Resources Worldwide. *Nat. Energy* **2022**, *7* (3), 260–269. https://doi.org/10.1038/s41560-022-00979-x.
(35)Duan, L.; Ruggles, T. H.; Caldeira, K. Electricity Systems in the Limit of Free Solar Photovoltaics and Continent-Scale Transmission. *iScience* **2022**, *25* (4), 104108. https://doi.org/10.1016/j.isci.2022.104108.
(36)Li, A. X.; Virgüez, E.; Dowling, J. A.; Wongel, A.; Covelli, D.; Ruggles, T. H.; Reich, N.; Lewis, N. S.; Caldeira, K. The Influence of Regional Geophysical Resource Variability on the Value of Single- and Multistorage Technology Portfolios. *Environ. Sci. Technol.* **2024**, acs.est.3c10188. https://doi.org/10.1021/acs.est.3c10188.
(37)Levi, P. J.; Kurland, S. D.; Carbajales-Dale, M.; Weyant, J. P.; Brandt, A. R.; Benson, S. M. Macro-Energy Systems: Toward a New Discipline. *Joule* **2019**, *3* (10), 2282–2286. https://doi.org/10.1016/j.joule.2019.07.017.
(38)Pfenninger, S. Dealing with Multiple Decades of Hourly Wind and PV Time Series in Energy Models: A Comparison of Methods to Reduce Time Resolution and the Planning Implications of Inter-Annual Variability. *Appl. Energy* **2017**, *197*, 1–13. https://doi.org/10.1016/j.apenergy.2017.03.051.

(39)Gonzato, S.; Bruninx, K.; Delarue, E. Long Term Storage in Generation Expansion Planning Models with a Reduced Temporal Scope. *Appl. Energy* **2021**, *298*, 117168. https://doi.org/10.1016/j.apenergy.2021.117168.
(40)North American Electric Reliability Corporation (NERC). *Standard BAL-502-RF-03: Planning Resource Adequacy Analysis, Assessment and Documentation*; BAL-502-RF-03; ReliabilityFirst Corporation, 2-17. https://www.nerc.com/pa/Stand/Reliability%20Standards/BAL-502-RF-03.pdf (accessed 2025-10-14).
(41)Stephen, G.; Tindemans, S. H.; Fazio, J.; Dent, C. J.; Figueroa Acevedo, A.; Bagen, B.; Crawford, A.; Klaube, A.; Logan, D.; Burke, D. Clarifying the Interpretation and Use of the LOLE Resource Adequacy Metric: PMAPS 2022; 2022. https://doi.org/10.1109/PMAPS53380.2022.9810615.
(42)Pfeifenberger, J. P.; Spees, K.; Carden, K.; Wintermantel, N. *Resource Adequacy Requirements: Reliability and Economic Implications*; The Brattle Group, 2013. https://www.ferc.gov/sites/default/files/2020-05/02-07-14-consultant-report.pdf.
(43)Peters, M. S.; Timmerhaus, K. D.; West, R. E. *Plant Design and Economics for Chemical Engineers*, 5th ed.; McGraw-Hill chemical engineering series; McGraw Hill: Boston, 2003.
(44)Vimmerstedt, L.; Akar, S.; Mirletz, B.; Sekar, A.; Stright, D.; Augustine, C.; Beiter, P.; Bhaskar, P.; Blair, N.; Cohen, S.; Cole, W.; Duffy, P.; Feldman, D.; Gagnon, P.; Kurup, P.; Murphy, C.; Ramasamy, V.; Robins, J.; Stehly, T.; Zuboy, J.; Oladosu, G.; Hoffman, J. *2022 Annual Technology Baseline*; NREL/PR-6A20-83064; NREL (National Renewable Energy Laboratory), 2022; p 65. https://atb.nrel.gov/ (accessed 2023-05-31).
(45)Hunter, C. A.; Penev, M. M.; Reznicek, E. P.; Eichman, J.; Rustagi, N.; Baldwin, S. F. Techno-Economic Analysis of Long-Duration Energy Storage and Flexible Power Generation Technologies to Support High-Variable Renewable Energy Grids. *Joule* **2021**, *5* (8). https://doi.org/10.1016/j.joule.2021.06.018.
(46)Hersbach, H.; Bell, B.; Berrisford, P.; Hirahara, S.; Horányi, A.; Muñoz-Sabater, J.; Nicolas, J.; Peubey, C.; Radu, R.; Schepers, D.; Simmons, A.; Soci, C.; Abdalla, S.; Abellan, X.; Balsamo, G.; Bechtold, P.; Biavati, G.; Bidlot, J.; Bonavita, M.; Chiara, G.; Dahlgren, P.; Dee, D.; Diamantakis, M.; Dragani, R.; Flemming, J.; Forbes, R.; Fuentes, M.; Geer, A.; Haimberger, L.; Healy, S.; Hogan, R. J.; Hólm, E.; Janisková, M.; Keeley, S.; Laloyaux, P.; Lopez, P.; Lupu, C.; Radnoti, G.; Rosnay, P.; Rozum, I.; Vamborg, F.; Villaume, S.; Thépaut, J. The ERA5 Global Reanalysis. *Q. J. R. Meteorol. Soc.* **2020**, *146* (730), 1999–2049. https://doi.org/10.1002/qj.3803.
(47)Huld, T.; Gottschalg, R.; Beyer, H. G.; Topič, M. Mapping the Performance of PV Modules, Effects of Module Type and Data Averaging. *Sol. Energy* **2010**, *84* (2), 324–338. https://doi.org/10.1016/j.solener.2009.12.002.
(48)Bett, P. E.; Thornton, H. E. The Climatological Relationships between Wind and Solar Energy Supply in Britain. *Renew. Energy* **2016**, *87*, 96–110. https://doi.org/10.1016/j.renene.2015.10.006.

(49)Feldman, D.; Margolis, R. *Fall 2021 Solar Industry Update*; NREL/PR-7A40-81325; National Renewable Energy Lab. (NREL), Golden, CO (United States), 2021. https://www.osti.gov/biblio/1829299 (accessed 2023-03-15).
(50)*Wind was second-largest source of U.S. electricity generation on March 29*. https://www.eia.gov/todayinenergy/detail.php?id=52038 (accessed 2023-03-15).
(51)U.S. Energy Information Administration (EIA). *EIA Monthly Energy Review*; 2023. https://www.eia.gov/totalenergy/data/monthly/pdf/mer.pdf.
(52)Waite, M.; Modi, V. Electricity Load Implications of Space Heating Decarbonization Pathways. *Joule* **2020**, *4* (2), 376–394. https://doi.org/10.1016/j.joule.2019.11.011.
(53)Mongrid, K.; Viswananthan, V.; Alam, J.; Vartanian, C.; Sprenkle, V.; Baxter, R. *2020 Grid Energy Storage Technology Cost and Performance Assessment.*; DOE/PA-0204; 2020.
(54)Colbertaldo, P.; Agustin, S. B.; Campanari, S.; Brouwer, J. Impact of Hydrogen Energy Storage on California Electric Power System: Towards 100% Renewable Electricity. *Int. J. Hydrog. Energy* **2019**, *44* (19), 9558–9576. https://doi.org/10.1016/j.ijhydene.2018.11.062.
(55)Ziegler, M. S.; Mueller, J. M.; Pereira, G. D.; Song, J.; Ferrara, M.; Chiang, Y.-M.; Trancik, J. E. Storage Requirements and Costs of Shaping Renewable Energy Toward Grid Decarbonization. *Joule* **2019**, *3* (9), 2134–2153. https://doi.org/10.1016/j.joule.2019.06.012.
(56)Fertig, E.; Apt, J. Economics of Compressed Air Energy Storage to Integrate Wind Power: A Case Study in ERCOT. *Energy Policy* **2011**, *39* (5), 2330–2342. https://doi.org/10.1016/j.enpol.2011.01.049.
(57)Grochowicz, A.; van Greevenbroek, K.; Benth, F. E.; Zeyringer, M. Intersecting Near-Optimal Spaces: European Power Systems with More Resilience to Weather Variability. *Energy Econ.* **2023**, *118*, 106496. https://doi.org/10.1016/j.eneco.2022.106496.
(58)Covelli, D.; Virgüez, E.; Caldeira, K.; Lewis, N. S. Oahu as a Case Study for Island Electricity Systems Relying on Wind and Solar Generation Instead of Imported Petroleum Fuels. *Appl. Energy* **2024**, *375*, 124054. https://doi.org/10.1016/j.apenergy.2024.124054.
(59)Wongel, A.; Caldeira, K. Broad Range of Technologies Could Firm Up Wind and Solar Generation in Net Zero Carbon Dioxide Emission Electricity Systems. *Findings* **2023**. https://doi.org/10.32866/001c.90391.
(60)Yuan, M.; Tong, F.; Duan, L.; Dowling, J. A.; Davis, S. J.; Lewis, N. S.; Caldeira, K. Would Firm Generators Facilitate or Deter Variable Renewable Energy in a Carbon-Free Electricity System? *Appl. Energy* **2020**, *279*, 115789. https://doi.org/10.1016/j.apenergy.2020.115789.